

國立臺灣大學生物資源暨農學院森林環境暨資源學系

碩士論文

School of Forestry and Resource Conservation

College of Bioresources and Agriculture

National Taiwan University

Master Thesis

電紡木質素磺酸鹽活性碳纖維－

製備、性質分析及應用

Electrospun Lignosulfonate Activated Carbon Fiber as Valuable

Metal Ion Adsorbents – Preparation, Characterization, and

Application

王思涵

Szu-Han Wang

指導教授：張豐丞 博士

Advisor: Feng-Cheng Chang, Ph.D.

中華民國 109 年 6 月

June, 2020



Acknowledgement



I am lucky enough to have the best family and professors on my way to finishing master. Thanks to all family members, backing me for every decision I have made, and always accompany me regardless of the situation. Thanks to Dr. Feng-Cheng Chang, supporting and giving me lots of opportunities and spaces to do things I want, and guiding me whenever I am stuck on research or life-wise. I really have learned a lot and can feel my growth over these years. Thanks to Dr. William Tai Yin Tze, making doing experiments at midnight much more joyful and directing me when I feel trapped. Thanks to Dr. Chuhsing Kate Hsiao for offering me the chance to be the teaching assistant of biostatistics class, it was truly fun to teach and learn at the same time. Thanks to Dr. Karl Rohe, answering my statistics questions while I am working on the thesis in Madison. Thanks to committee members: Dr. Hsing-Cheng Hsi, Dr. Hong-Ping Lin, Dr. Han-Chien Lin, and Dr. Pei-Yu Kuo for helping me improve the thesis.

Thanks to all friends in lab, Christy, Peter, Yi-Hsuan, and those who have graduated, Chi-Chi and Lang-Ting, it is so much more enjoyable to work with you guys around than working alone. Thanks to friends outside the lab, especially Mathias, Ninna, and Shao-en, always dragging me outside the lab to relax a bit. Also, thanks to friends and course buddies in Madison for accompanying me, Andy, Brian, Amanda, Bindesh, Cheng-Hsien, Eda, Gennie, Joey, Pan, Parker, Robin, Sam, Sean, Tzyy-Hsien, another Yi-Hsuan, Yi-Ming, and Yun-Chia.

Thanks to Ørsted for offering me the scholarship and providing all possible resources to access the offshore wind industry, it really opens another career possibility for me. There are just too many people that I want to say thanks to. Overall, thanks to the world and life for teaching me lessons and making me a better person.

摘要



隨著科技日新月異，電子廢棄物回收成為刻不容緩的議題。眾多解決方案中，以生質廢棄物回收電子垃圾為較環境友善的辦法。木質素磺酸鹽是近來廣受歡迎的生質廢棄物。每年，全球造紙業產生上萬噸的木質素磺酸鹽，其豐富的碳含量，具備作高值化利用的潛能。

此研究分為兩部分：木質素磺酸鹽活性碳纖維研發、以及木質素活性碳纖維金屬離子吸附研究。第一部份利用靜電紡絲法紡織木質素纖維膜，接著以二氧化碳進行物理活化，產出木質素活性碳纖維。進一步以物理及化學方法分析材料特性，以選擇材料最佳活化時間。材料結構由電子掃描顯微鏡 (Scanning electron microscope, SEM) 以及比表面積與孔徑分佈儀進行檢測。材料表面性質由元素分析儀、X 射線光電子能譜儀 (X-Ray Photoelectron Spectroscopy, XPS)、傅立葉轉換紅外光譜儀 (Fourier Transform Infrared Spectroscopy, FTIR)、拉曼光譜儀 (Raman Spectroscopy) 進行分析。

第二部分利用第一部分最佳條件之木質素活性碳纖維，分別以批次法吸附二價銅離子、三價金離子。由於銅、金離子為電子廢棄物中含量、價值較高之金屬，故選擇其作為吸附對象。吸附行為主要由三個角度分析：不同金屬離子濃度對材料吸附量之影響 (吸附等溫線)、不同金屬離子溶液酸鹼值對材料吸附量之影響、不同吸附時間對吸附量之影響 (吸附動力學)。並進一步以不同等溫線模型、動力學模型擬合實驗數據，由赤池信息量準則 (Akaike Information Criterion, AIC) 選擇較佳模型。此外，亦由金屬離子脫附試驗評估木質素磺酸鹽活性碳纖維之重複利用性。

分析結果顯示，經 60 分鐘活化之木質素磺酸鹽活性碳纖維具較高比表面積、微孔體積，及較多酸性官能基，故有潛力成為較佳金屬離子吸附劑。根據吸附行為研究，銅離子與金離子之吸附機制皆為物理、化學吸附混合，其中，金離子吸

附較傾向於化學吸附。此外，吸/脫附試驗顯示，木質素磺酸鹽活性碳纖維在三輪吸脫附循環後，仍具備吸附銅、金離子之效能。整體而言，此研究開拓物理活化木質素磺酸鹽活性碳纖維與其回收有價值金屬離子之應用。



關鍵詞：木質素磺酸鹽、活性碳纖維、靜電紡絲法、物理活化、金屬離子、吸附
機制

Abstract



Living in an electronic-dominated world, e-wastes have become an urgent problem. From an environment point of view, an effective solution would be leveraging renewable source, preferably another type of wastes, to recycle these metals. One waste that is easy to deal with is lignosulfonate. Tons of them were produced as byproduct by the pulp industry every year. As a carbon-rich polymer, it is worth the attention for a higher-value investment.

The research is divided into two parts, including the development of lignosulfonate activated carbon fiber (LACF) and its metal recovery behavior. LACF was developed through the electrospinning technique, followed by a series of CO₂-based physical activation. Physical and chemical characterization were implemented to find the optimized activation time for developing LACF. For the material structure, scanning electron microscope (SEM) and specific surface area and pore size distribution analyzer were utilized. In terms of the surface properties, elemental analysis, X-Ray Photoelectron Spectroscopy (XPS), Fourier Transform Infrared Spectroscopy (FTIR), and Raman Spectroscopy were applied.

Throughout the second part of the study, the adsorption behavior of Cu(II) and Au(III) metal ions were respectively tested with batch methods on the lab-made LACF. The metal ions were chosen for their larger amount and higher value. Examinations included the adsorption capacity change according to various adsorbate concentrations, adsorbate pH environment, and adsorption equilibrium time. In order to explore the adsorption mechanism, isotherm and kinetic modeling were performed, and the Akaike Information Criterion (AIC) was implemented to choose the better model. Further, desorption tests were executed to evaluate the reusability of LACF.

It was observed that LACF with a 60-min activation treatment possessed a higher specific surface area, micropore ratio, and more acidic functional groups, which potentially made it a better candidate for metal-ion adsorption. According to the adsorption behavior study, both Cu(II) and Au(III) ions were adsorbed onto LACF with a mix of physi- and chemisorption, while the latter was more inclined to chemisorption. Furthermore, the LACF could recover these two metal ions after 3 adsorption-desorption cycles. Overall, this study paves the way for physically activated lignosulfonate carbon and its application in recovering valuable metal ions.

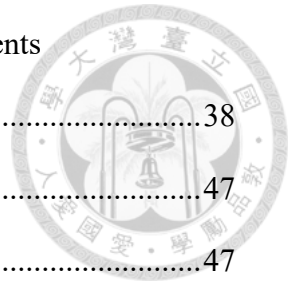
Keywords: lignosulfonate, activated carbon fiber, electrospinning, physical activation, metal ion, adsorption mechanism

Table of Contents



Acknowledgement	i
摘要.....	ii
Abstract.....	iv
Table of Contents	vi
List of Figures.....	viii
List of Tables.....	x
Chapter 1: Introduction.....	1
Chapter 2: Background and Literature Review	4
2.1 Introduction of Lignosulfonate	4
2.2 Production of Electrospun Lignosulfonate Activated Carbon Fiber (LACF)..	5
2.2.1 Electrospinning.....	5
2.2.2 Pre-oxidation (Thermal stabilization).....	14
2.2.3 Carbonization.....	15
2.2.4 Physical Activation	16
2.3 Adsorption mechanism.....	18
2.3.1 Physical adsorption (Physisorption)	18
2.3.2 Chemical adsorption (Chemisorption).....	23
Chapter 3: Materials and Methods.....	25
3.1 Materials	25
3.2 Methods.....	25
3.2.1 LACF Production.....	25
3.2.2 Characterization of LACF	27
3.2.3 Characterization of LACF with metal ion	38

3.2.4 Mono-component Metal Recovery experiments (Batch/Column).....	38
Chapter 4: Results and Discussion.....	47
4.1 Characterization	47
4.1.1 Physical Characterization	47
4.1.2 Chemical Characterization.....	51
4.1.3 Characterization of LACF with metal ion	63
4.2 Batch Adsorption experiment	66
4.2.1 Cu(II)/Au(III) adsorption according to various pH	66
4.2.2 Cu(II)/Au(III) adsorption according to various concentration (Isotherm) 68	
4.2.3 Cu(II)/Au(III) adsorption according to various contact time (Kinetics) 77	
4.3 Desorption and Recycle of LACFs.....	79
Chapter 5: Conclusions and Recommendations	82
References.....	85



List of Figures



Figure 1. Hardwood lignosulfonate chemical structure (modified from [14])	5
Figure 2. Basic electrospinning setup [15]	6
Figure 3. SEM photographs of electrospun nanofibers from different polymer concentration solutions [25].....	7
Figure 4. An electrospinning jet that contained three successive electrical bending instabilities [38]	10
Figure 5. A schematic rotating collector for electrospun ultrafine fibers [54].....	12
Figure 6. Aligning electrospun fibers with an auxiliary electrical field [52].....	12
Figure 7. A set-up for thin-wheel electrospinning [53].....	13
Figure 8. H ₂ O activation reactions (modified from [64])	17
Figure 9. CO ₂ activation reactions (modified from [64])	17
Figure 10. H ₂ O activation in presence of metal catalysts (modified from [64]).....	18
Figure 11. Classification of physisorption isotherms [68].....	19
Figure 12. Classification of hysteresis loops [68].....	22
Figure 13. (a) electrospinning apparatus; (b) fabricated lignosulfonate fiber mat	26
Figure 14. Two-step carbonization/activation process.....	27
Figure 15. Possible highly defective carbonaceous structures [73].....	28
Figure 16. Typical BET plot [81].....	31
Figure 17. BET plot for an ACF adopting the classical relative pressure range (0.05–0.25)	32
Figure 18. Plot of P/P_0 vs. $V[1-(P/P_0)]$	33
Figure 19. BET plot for the same ACF adopting the criteria.....	33
Figure 20. Scheme of QSDFT model [67].....	35

Figure 21. LACFs (a) without water wash; (b) after water wash for 10 mins.....	47
Figure 22. LACF morphology (a) nest-like; (b) cage-like.....	48
Figure 23. Typical N ₂ (77.35 K) adsorption-desorption isotherm of LACF.....	48
Figure 24. Physical characterization of LCF, LACF30 and LACF60	49
Figure 25. QSDFT pore size distribution.....	50
Figure 26. Point of zero charge.....	52
Figure 27. FTIR spectrum of LACF	54
Figure 28. Scheme of Lignosulfonate transforming to LACF (modified from [70,112,113]).....	56
Figure 29. Reaction with CO ₂ (○ denotes a vacant site[64]).....	57
Figure 30. XPS C1s spectra. Left: CF; Right: above: LACF30; below: LACF60	59
Figure 31. Raman Spectrum of LACF.....	61
Figure 32. EDS for LACF. Left: examined area; right: element detection.....	63
Figure 33. EDS for LACF-Cu. Left: examined area; right: element detection.....	64
Figure 34. EDS for LACF-Au. Left: examined area; right: element detection	64
Figure 35. FTIR for LACF – before, after adsorption, and after desorption	65
Figure 36. Effect of pH solution on Cu(II) adsorption	67
Figure 37. Effect of pH solution on Au(III) adsorption.....	68
Figure 38. Batch isotherm test: Cu-original(above); Cu-excluded(below)	70
Figure 39. Batch isotherm test: Au-original(above); Au-excluded(below)	73
Figure 40. Batch kinetics test: Cu(II)(above); Au(III)(below).....	78
Figure 41. 3-cycle Cu(II) adsorption-desorption	80
Figure 42. 3-cycle Au (III) adsorption-desorption.....	80

List of Tables



Table 1. Fixed positions in peak-deconvolution-step-1 [88]	37
Table 2. Zeta potential of CF and LACF	51
Table 3. FTIR peak assignment	55
Table 4. Elemental Analysis of LCF, LACF30 and LACF60	59
Table 5. XPS C1s LACF30 and LACF60 functional group ratio	61
Table 6. Cu(II) adsorption isotherm modeling result.....	71
Table 7. AICc calculation for each model fitting result (Cu ²⁺).....	72
Table 8. Au isotherm modeling result (calculate from R).....	74
Table 9. AICc calculation for each model fitting result (Au ³⁺).....	75
Table 10. Free-energy calculation for Cu(II) and Au(III)	76
Table 11. Estimated parameters from kinetic models	79
Table 12. AICc calculation for each model fitting result.....	79

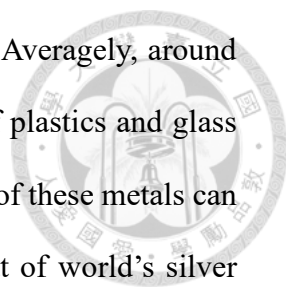
Chapter 1: Introduction

Motivated by the need of finding alternatives for petroleum products, recently more interests have been drawn to biowaste-based product development. Lignin, as the second most abundant macromolecule (next to cellulose) in nature, has thus become a popular raw material for applications in activated carbon production, adhesive, or tanning agent [1,2]. Large amount of lignin is readily available thanks to the paper and pulp industry, but much of it is burnt as energy, and only 1-2% of the technical lignin is used in non-fuel high-value applications [1].

Lignin is composed of more than 60% carbon content. A large ratio of the structure consists of aromatic rings, resembling that of activated carbon [1,2]. Therefore, among all applications, substituting for current petroleum precursor in activated carbon production should be promising. Technical lignin includes kraft lignin, liginosulfonate and organosolve lignin [3], among which, kraft lignin is mostly used in past studies, and liginosulfonate on the other hand, has not been adequately explored [1]. However, millions of tons of liginosulfonates are produced each year as dry solids [1]. It contains sulfur groups, which can be beneficial to metal ion adsorption[4,5], and is hydrophilic, increasing ease of further processing. With large quantity and favorable structures, liginosulfonate has the potential to be transformed into effective carbon adsorbents.

One of the emerging applications of carbon adsorbent is recovering electronic waste (e-wastes). As technology advances, over the past five years, electronic waste accumulation within a year has doubled, climbing from approximately 20 to 40 million tons per year globally, and is estimated to exceed 50 million tons by 2021 [6]. According to the Environmental Protection Agency (EPA), only 15-20% of e-waste is recycled, and the rest is transported to developing country for disposal, leading to serious environment, human health problems, and economic loss [6]. While these e-wastes are





malfunctioned, the heavy and precious metals within are valuable. Averagely, around 40% of an e-waste is composed of metals, along with a mixture of plastics and glass [6]. A report from world economic forum shows that the total value of these metals can reach 62.5 billion USD, which is three times more than the output of world's silver mines [7]. If the e-wastes are recovered and return to the industry, it can not only contribute to the circular economy, but benefit the environment.

Currently, the more environmental-friendly method for recycling e-wastes is hydrometallurgy [6]. It consists of two main steps, chemical leaching followed by metal recovery. Activated carbon adsorption contributes to the second step, during which metal ions can precipitate on the surface, and recover through desorption. Among all other precipitation methods, such as ion exchange, cementation, and solvent extraction, activated carbon stands out as it requires fewest chemicals; hence, more sustainable.

With a view to leveraging wastes to recover wastes, this research focused on developing lignosulfonate-based activated carbon, and further tested its ability to recover metal ions. To be more specific, among all forms of activated carbon, fiber form was chosen. Comparing to common granular activated carbons, who have ladder-like structures, and adsorbates need to pass through macropores before entering smaller pores, activated carbon fibers possess faster adsorption rate [8,9]. Their meso- and micropores are readily exposed to the surface of the fibers. Another advantage is that, powder and granular forms are difficult to recycle, while fiber mat is easy for handling [9].

Built on previous researches [10,11], this study used electrospinning technique and 2-step carbon dioxide activation method to develop lignosulfonate-activated carbon fiber (LACF). Physical and chemical characterizations were done to evaluate LACF's morphology, pore structure, and surface properties. After feature verification, the

optimized sample was chosen for metal recovery tests. The metal adsorption mechanism was studied through modeling, and metal ion desorption was further implemented to examine LACF's regeneration capability.



Chapter 2: Background and Literature Review



2.1 Introduction of Lignosulfonate

Lignosulfonate is one of the byproducts from pulp industry. It is extracted from the sulfite pulping process, during which the sulfur dioxide (SO_2) is mixed with an alkaline solution to create the raw liquor for cooking wood. This process introduces the sulfonate group (SO_3^-) onto the lignin structure to replace the hydroxyl group, resulting in its solubility feature [12]. As a lignin-type material, it also contains rich carbon content.

Each year, approximately 1.8 million tons of lignosulfonate are produced, which accounts for 90% of the total commercial lignin market [13]. Currently, most common applications for lignosulfonates include animal feed, pesticides, surfactants, additives in oil drilling, stabilizers in colloidal suspensions, and as plasticizers in concrete admixtures [13]. As the structure in Figure 1 shows [14], it contains rich carbon content, and has the aromatic structure that is similar to activated carbon. Therefore, besides the usages mentioned above, its application in activated carbon production is worth more attention.

In the past, the difficulty for dealing with lignosulfonate as an activated carbon precursor stems from its hydrophilicity feature. In this study, hydrophilicity on the other hand, is the characteristic that assists with the production. To knit a fiber cloth precursor, electrospinning technique was implemented, during which, lignosulfonate could easily blend with polymers and evenly disperse in dH_2O for the electrospinning solution preparation, leading to a clean process.

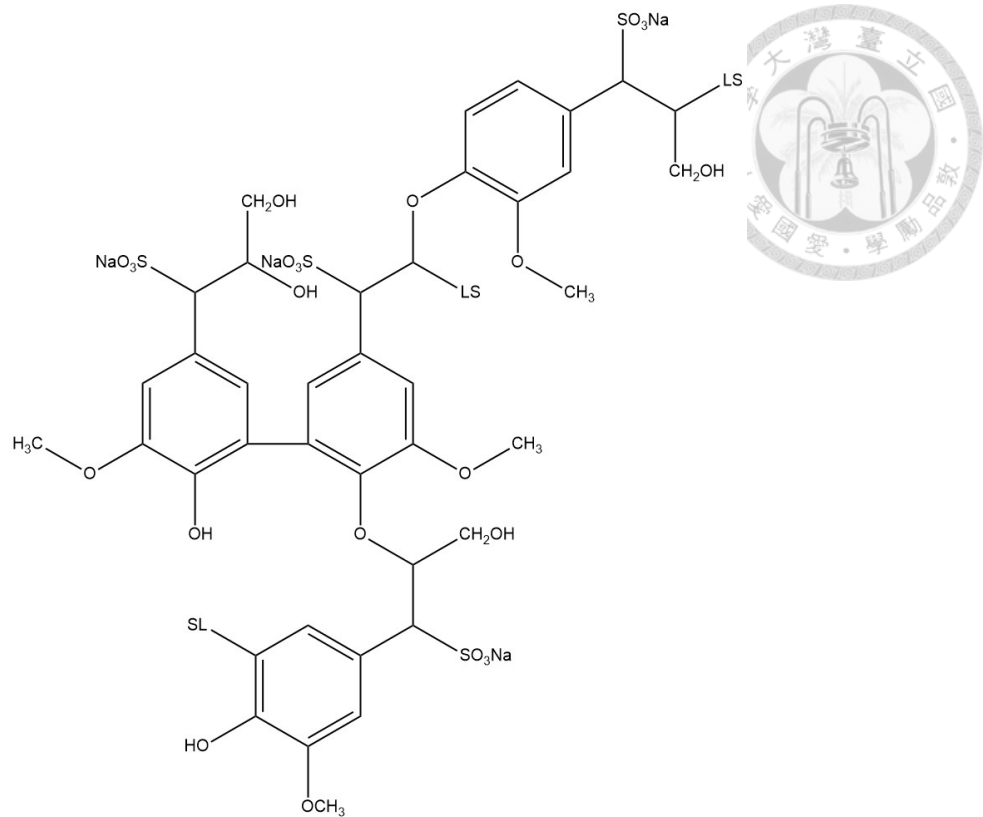


Figure 1. Hardwood lignosulfonate chemical structure (modified from [14])

2.2 Production of Electrospun Lignosulfonate Activated Carbon Fiber (LACF)

2.2.1 Electrospinning

2.2.1.1 Basics

As Figure 2 shows, an electrospinning device consists of three fundamental components: a high voltage supplier, a capillary tube or syringe with a pipette or needle of small diameter, and a grounded metal collector [15]. First, most polymers would be dissolved in solvents before electrospinning, and when completely dissolves, forms polymer solution, which would then be introduced into a syringe. Second, the syringe is put onto a syringe pump, and parameters are adjusted depending on different uses. Third, the distance from the needle tip to the collector is altered to 10-25 cm in laboratory systems. Fourth, the voltage supplier is connected to the needle tip of the syringe. After all settings are done, a DC voltage in the range of $100\text{-}500\text{ kVm}^{-1}$ is

applied [16,17]. Then, under room temperature and appropriate atmosphere conditions, electrospinning is conducted.

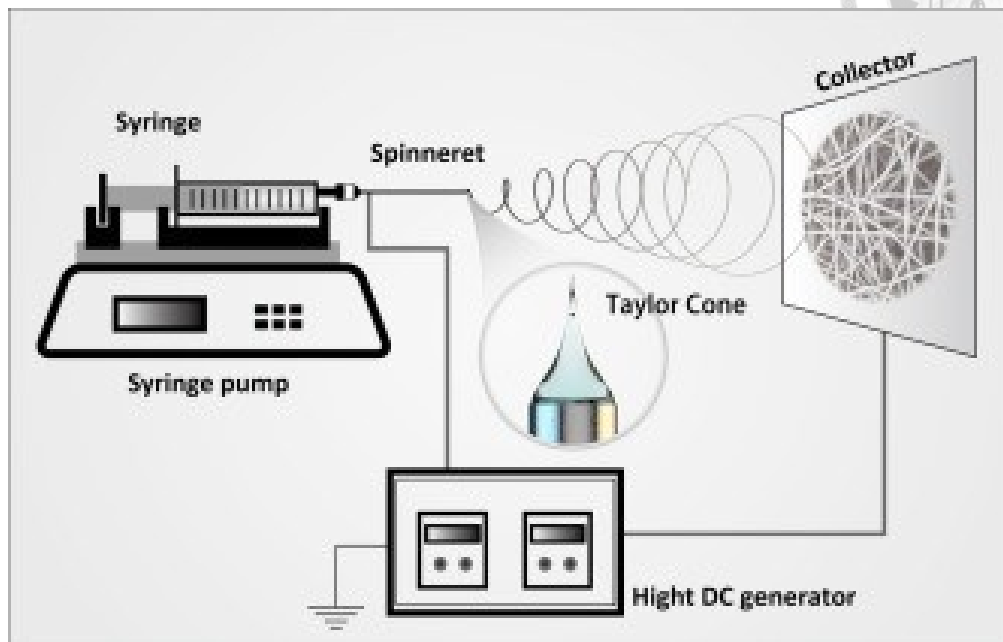
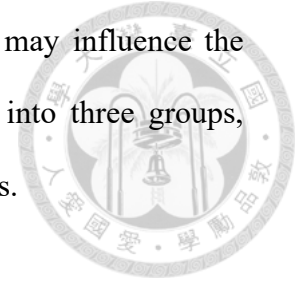


Figure 2. Basic electrospinning setup [15]

In the process, at the tip of a syringe, a polymer solution is held by its surface tension, and it is subjected to an electric field. This electric field induces an electric charge on the liquid surface. When the electric field reaches a critical value, the repulsive electrical forces overcome the surface tension forces. As a result, a charged jet of the solution is ejected from the tip of the Taylor cone, an unstable and a rapid whipping of the jet occurs in the space between the tip and collector which leads to evaporation of the solvent, leaving a polymer behind. The jet is only stable at the tip, which results in nonwoven fibers at the collector [17–19].

2.2.1.2 Parameters investigation

During electrospinning process, there are many factors that may influence the morphology of the fibers. Those parameters can be categorized into three groups, solution parameters, processing parameters, and ambient parameters.



Solution Parameters

Concentration

To form fibers, a minimum polymer solution concentration is required. At a low solution concentration, a mixture of beads and fibers is obtained. When the concentration increases, viscosity resistance raises as well [20–24] ; therefore, the beads transform to spindle-like, and finally form uniform fibers [25]. However, if the concentration is too high, it is impossible to form continuous fibers, because the flow of the solution at the tip of the needle cannot be maintained. Thus, high concentration will result in larger and discontinuous fibers [26].

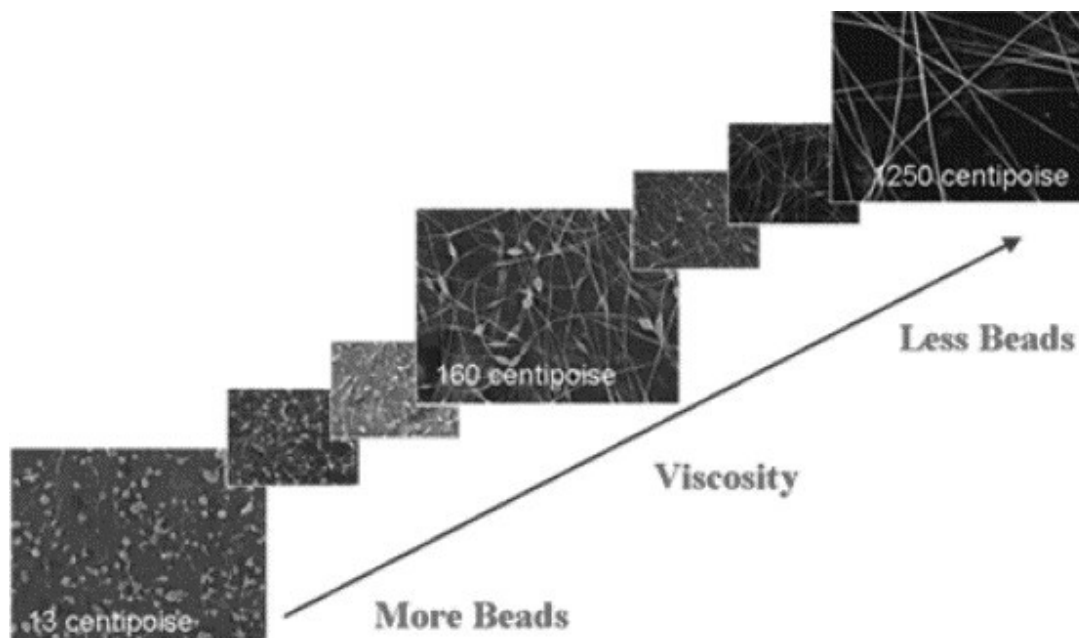


Figure 3. SEM photographs of electrospun nanofibers from different polymer concentration solutions [25]



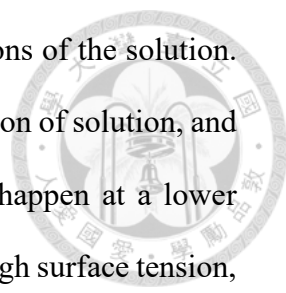
Molecular weight

A polymer solution with low molecular weight tends to form beads instead of fibers, while that with high molecular weight contributes to fibers with larger average diameters. Reasons are that molecular weight of the polymer reflects the number of entanglements of polymer chains in a solution, thus solution viscosity, which affects fibers' morphology. Chain entanglements provide interchain connectivity, which is significant to electrospinning, and make it possible for low polymer concentration to generate nanofibers [27]. Besides, sufficient intermolecular interactions can substitute for the interchain connectivity; hence, a polymer solution without high molecular weights but adequate intermolecular interactions can still fabricate nanofibers through electrospinning [28,29].

Viscosity

Concentration, molecular weight and viscosity correlate with each other, accordingly they have similar effects on the morphology of fibers. It has been discovered that solution with very low viscosity cannot form continuous fiber, as viscosity increases, it can form fibers with more uniform and larger diameter [20]. Nevertheless, extremely high viscosity solutions also have difficulties fabricating fibers, because they usually exhibit longer stress relaxation times, which prevent them from ejecting jets [17]. It is reported that the maximum spinning viscosities range from 1 to 215 poise, and each polymer has its own specific optimal viscosity, which consequently helps produce continuous fibers [30–33].

Surface tension



Surface tension more likely depends on the solvent compositions of the solution. The formation of droplets, bead, and fibers relies on the surface tension of solution, and a lower surface tension of the solution allows electrospinning to happen at a lower electric field, what's more, beads-free fibers can be obtained [24]. High surface tension, on the other hand, generally inhibits the electrospinning process due to instability of the jets and the generation of sprayed droplets [34]. Nonetheless, low surface tension of a solvent is not always suitable for electrospinning, only when other variables are held constant can it be the key factor that determines whether electrospinning succeeds or not [25,35,36].

Conductivity

Polymer type, solvent used and the availability of ionisable salts mainly determine the solution conductivity. It has been discovered that solutions with low conductivity brings about insufficient elongation of a jet by electrical force, which cause the failure of producing uniform fibers, and beads may be observed as well. On the other hand, if the conductivity increases, the diameter of the fibers decreases and beads-free fiber is obtained; yet, when electric fields are strong at the same time, it will cause dramatic bending instability and a wide distribution of fiber diameter [17,37]. Bending instability describes a phenomenon that the jet does not move along with one axis, instead, it bends in a different direction, as Figure 4 shows [38]. If the solution conductivity is not sufficient, adding ionic salts such as KH_2PO_4 , NaH_2PO_4 , NaCl can help solve the problem and eventually acquire smaller-diameter and beadless fiber [39]. Aside from fiber morphology, electrical conductivity also influences jet radius: jet radius varied inversely with the cube root of the electrical conductivity.

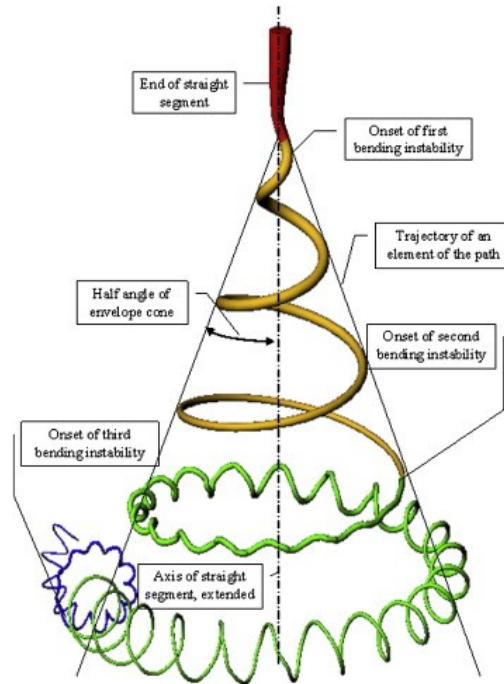


Figure 4. An electrospinning jet that contained three successive electrical bending instabilities [38]

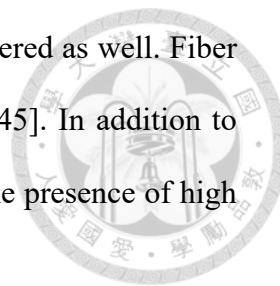
Processing Parameters

Applied voltage

Applied voltage along with electric field induce the necessary charges on the solution which is necessary for initiating the electrospinning process and fiber formation, so only after attaining the threshold voltage do fiber fabricate [17]. The impact of applied voltage, however, is disputable. Some have shown that it has little effect on the morphology of the electrospun fiber [40], others have proposed that under higher voltages, more polymer ejected and larger diameter fiber formed [35,41], still others have suggested that an increase of applied voltage led to greater electrostatic repulsive force on the fluid jet or the greater stretching of the solution which ultimately favor the smaller diameter fiber [42–44].

Some researchers have found that, it is the applied electric field that influences fiber's diameter, which means that except for applied voltage, polymer concentration

and the distance between the tip and the collector need to be considered as well. Fiber diameter decreases with the increase of the applied electric field [45]. In addition to fiber diameter, there's a greater probability of beads formation in the presence of high voltage [20].



Flow rate

The flow rate of the polymer solution from the syringe has impacts on the jet velocity and the material transfer rate [17]. Lower flow rate is more desirable because the solvent will then have enough time to evaporate; however, there exists a minimum value that allows the fiber to form [46]. As the flow rate raises, the fiber diameter and the pore diameter increases, what's more, high flow rates contribute to beaded fibers due to the lack of proper drying time before polymers reach the collector [46–49].

Type of collectors

Traditionally, an aluminum foil is used as a collector, but because of the difficulty in transferring the collected fibers, and as the needs for aligned fibers in various applications raise, more collectors have been developed. Following are several techniques that have been attempted to align electrospun nanofibers: a cylinder collector with high rotating speed [50,51], an auxiliary electrode/electrical field [52], and a thin wheel with sharp edge [53].

Researchers suggested that rotating a cylinder collector (Figure 5) at a very high speed up to thousands of rpm (round per min), electrospun nanofibers could be more or less oriented. The detailed mechanism was hypothesized as the following: when a linear speed of the rotating cylinder surface and the disposition rate of evaporated jet matches with each other, the fibers adhere on the surface of the cylinder in a circumferential

manner, and thus create a fair alignment in the end. Such speed is called “alignment speed”. On the other hand, if the surface speed of the cylinder is slower than the alignment speed, fibers will randomly deposit on the collector. In this method, there are still possibilities that orderless fibers are produced, reasons are that, motions of polymer jets are irregular and uncontrollable [50,51,54].

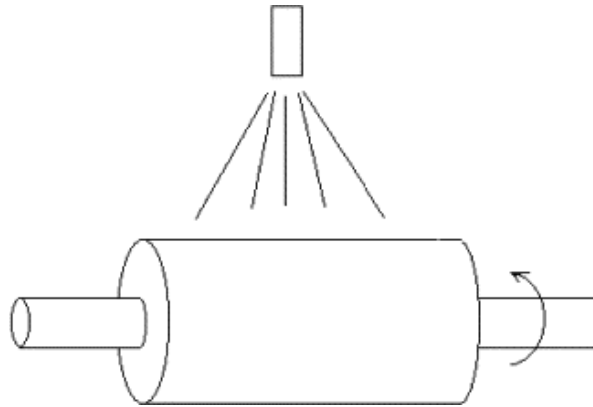


Figure 5. A schematic rotating collector for electrospun ultrafine fibers [54]

An auxiliary electrode/electrical field is an approach originally designed to fabricate tubular products for blood vessel prosthesis, urinary and bile duct applications. The feature of this invention is that, only by employing an auxiliary electrical field, the deposited fibers can be circumferentially oriented substantially (Figure 6) [52].

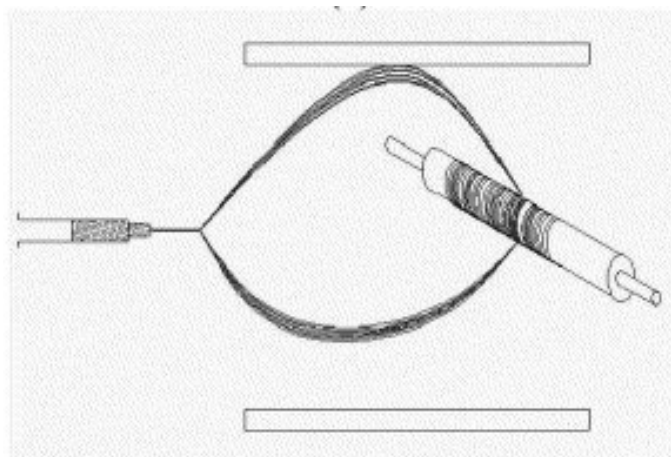


Figure 6. Aligning electrospun fibers with an auxiliary electrical field [52]

A thin wheel with sharp edge is a method to position and align nanofibers on a disk collector. The tip-like edge significantly concentrates the electrical field so that the spun nanofibers are mostly attracted to, which also allow them to be continuously wound on the edge of the rotating wheel. The mechanism is that, before reaching the electrically grounded collector, the nanofibers retain sufficient residual charges to repel each other, which influences the morphology of fiber depositions. As a result, once a nanofiber is attached to the wheel tip, it will exert a repulsive force on the next fiber attracted to the tip. The repulsion leads to a separation between the deposited nanofibers (Figure 7) [53,54].

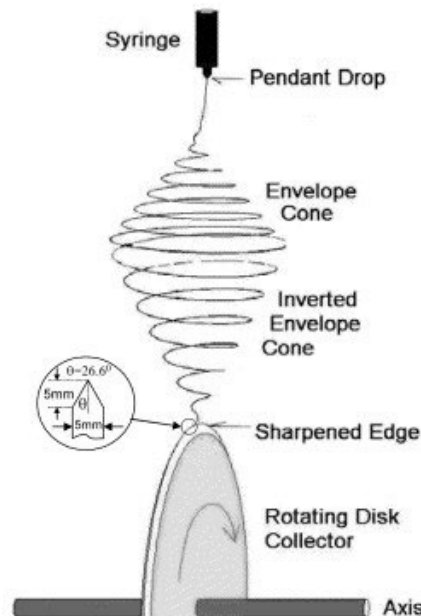


Figure 7. A set-up for thin-wheel electrospinning [53]

Tip to collector distance

The solvent evaporates between the distances between the tip to collector, and therefore, a minimum distance is required to offer fibers enough time to dry. If the distances are either too close or too far, beads will be observed [55–57]. Due to the factor that the influence of this parameter depends greatly on the speed that a solvent

evaporates, the optimum distance varies from different situation. Some have found that shorter distances will yield smaller fibers [36], while others have reported that closer distances will lead to flatter fibers [32].



Ambient Parameters

Humidity

As environment humidity increases, small circular pores will appear on the surface of the electrospun fibers, and further, increasing the humidity leads to the pores to fuse together and become bigger ones [58]. At an extremely low humidity, a volatile solvent may dry rapidly. Sometimes the evaporation rate is much faster than the removal rate of the solvent from the tip, which would cause a problem to electrospinning. Eventually, the electrospinning process may only be carried out for a few minutes before the needle tip is clogged [30]. As for high humidity, it has been reported to help the discharge of the electrospun fibers [59,60].

Temperature

There is an inverse relationship between viscosity and ambient temperature [17]. Studies have shown that as environment temperature increases, the fiber diameter decreases, and the attribution is the decreasing polymer solution viscosity as the temperature increases [61].

2.2.2 Pre-oxidation (Thermal stabilization)

Pre-oxidation is also known as the thermal stabilization process for an activated carbon precursor, which can increase the product yield rate [11,62]. Parameters such as heating rate, time, and temperature vary from different kinds of precursors. Lignin-type

material is said to be have the optimized condition when the heating rate is 1 °C/min or slower [11,63,64]. A successful pre-oxidation helps stabilized the fiber cloth by transforming the structure from thermoplastic to thermostatic, and prevent the fibers from melting, fusing, degrading or decomposing rapidly at high temperatures [64]. To be more specific, for cellulosic precursors, the whole process includes four stages [65]:

- (1) Stage I: Under 25-150 °C range, physical desorption happens to get rid of 12 % adsorbed water, accompanying by a small change in the lateral order (i.e. the side-by-side packing of the molecules within a linear polymer).
- (2) Stage II: At 150-240 °C, -H and -OH fragments within the cellulose (or lignin) unit are dehydrated. From past IR result, -C=O and C-C cleavage are also involved, and thus during this stage, the dehydration is intramolecular (i.e. exists within the molecule).
- (3) Stage III: when temperature climbs to 240-400 °C, more -C=O and C-C bonds break, and slower linkages through radical reactions happen (i.e. cross-linking). During this process, large amounts of tar, H₂O, CO, and CO₂ are created.
- (4) Stage IV: Beyond 400 °C, each cellulose unit breaks into a residual that consists of carbon atoms, which then polymerize through condensation reactions involving the removal of -H and transform into a graphite-like structure.

Usually, pre-oxidation is defined as the heat treatment with oxygen under 300 °C [11]. Therefore, during the process, stage 3 is possibly only partially completed. The transformation will continue in the next carbonization session.

2.2.3 Carbonization

Carbonization is also known as pyrolysis. It is usually executed under an inert environment with high temperature, which can go up to 700 – 1100 °C, and may not exceed 1300 °C [64]. Due to the fact that, as the treated temperature increases, the

carbon fiber will transform into a highly graphitic structure, comparing to less graphitic structure, the former one has fewer reactive carbons on the edges, which will hinder the later activation process, making it difficult to create highly porous ACFs [64].

As mentioned in the previous stage, during carbonization, above 400 °C, the fiber will continue to complete stage III and IV to arrange into the crystalized graphite structure. During the whole process, the weight loss varies between 40 – 70%, depending on the composition [12]. At stage I and II, the weight loss results from the evaporation of moisture, while in stage III, where the main loss happens, is attributed to the generation of volatile gas. After carbonization, activation is done to create a porous structure.

2.2.4 Physical Activation

Activation methods include chemical activation and physical activation. Most common activation reagents for chemical activation are: phosphoric acid (H_3PO_4), zinc chloride (ZnCl_2), and potassium hydroxide (KOH) [64]. Although chemical activation leads to higher activated carbon yield rate, it has a higher environmental cost, and the wasted reagents are more expensive to deal with. Out of sustainability concern, in this study, physical activation is focused.

For physical activation, two popular ones are CO_2 , and H_2O . During the physical activation processes with these two gases, as Figure 8 and Figure 9 show, carbon monoxide and hydrogen are generated. For both reagents, in the reversible reactions, the forward reaction is much faster (more than 100 times), and hence, when the concentration of CO and H_2 climb, it has an inhibiting effect on the forward reaction, which helps to control the gasification and further porosity development [64].

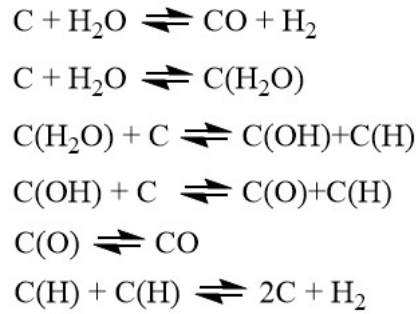


Figure 8. H₂O activation reactions (modified from [64])

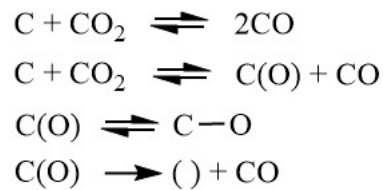


Figure 9. CO₂ activation reactions (modified from [64])

The carbon atoms on the surface have different reactivity depend on whether localized at the edges or the basal plane. These at the edges are usually more reactive. Except for constructing porosity, during activation, the carbon atoms also complexate with oxygen atoms, formulating oxygen-containing groups, while some of them are stable enough to stay until the end, some of them are broken down, leaving the unsaturated carbon atoms for further activation with the gas reagents [64].

If the carbonized sample used for activation contains inorganic impurities, some of them can act as gasification catalysts, and help construct mesopores. Examples such as salts, oxides, and metals of the series of alkali metals, alkali earth metals, and transition metals. A proposed mechanism of H₂O_(g) activating samples consisting of metal catalysts are shown in Figure 10 [64]. In these cases, H₂O tends to get contact with metal ions; then, the metals act as the oxygen carrier to further react with the carbon atoms. As mentioned before, some of the C(O) remain until the end of the activation, for those who does not last long, they are peeled off as carbon monoxide, leaving reactive carbon atoms behind for further activation.

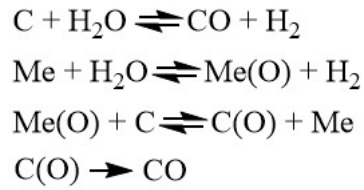


Figure 10. H₂O activation in presence of metal catalysts (modified from [64])

At the same activation temperature, comparing between CO₂ and H₂O activation, the former is slower than the latter. However, because of the slower reaction, CO₂ can construct better microporous structure [64]. For a richer pore structure, CO₂ is chosen for this study.

2.3 Adsorption mechanism

2.3.1 Physical adsorption (Physisorption)

Physical adsorption happens when an adsorbable gas contacts the surface of a solid. In this phenomenon, the gas is considered as the adsorptive (or adsorbate), while the solid is called the adsorbent [66]. Forces account for physisorption are van-der Waals forces, including long-range London dispersion forces and short-range intermolecular repulsion. Combination of these forces lead to the nonspecific, zero-chemical-bond molecular interactions [66]. Among porous materials, physisorption depends on three main factors, fluid-wall interactions, fluid-fluid interactions, and the effects that confined pore space has on fluids' state and thermodynamic stability amid narrow pores. The influences altogether govern the shape or type of the adsorption isotherm [66].

The adsorption isotherm depicts how the adsorbed gas amount change according to different relative pressure under a constant temperature. The most common methods to acquire the adsorption isotherms are volumetric (manometric) and gravimetric method. The gravimetric method contains a balance design used to measure the adsorption amount and the equilibrium pressure on the pressure sensor. It is mostly used

for adsorption that happens near room temperature. As for the volumetric method, with the adsorbent and gas amount in the dead space, the difference of the total gas amount induced to the sample cell can be specified, and therefore the adsorbed amount can be calculated. It is commonly measured with the adsorption of nitrogen, argon, and krypton at cryogenic temperatures, and CO₂ at 273 K, which are also widely used for surface area and pore-size characterization. In practical use, nitrogen at 77 K, argon at 87 K are popular methods for mesoporous materials, while carbon-dioxide at 273 K is more proper for microporous materials [67].

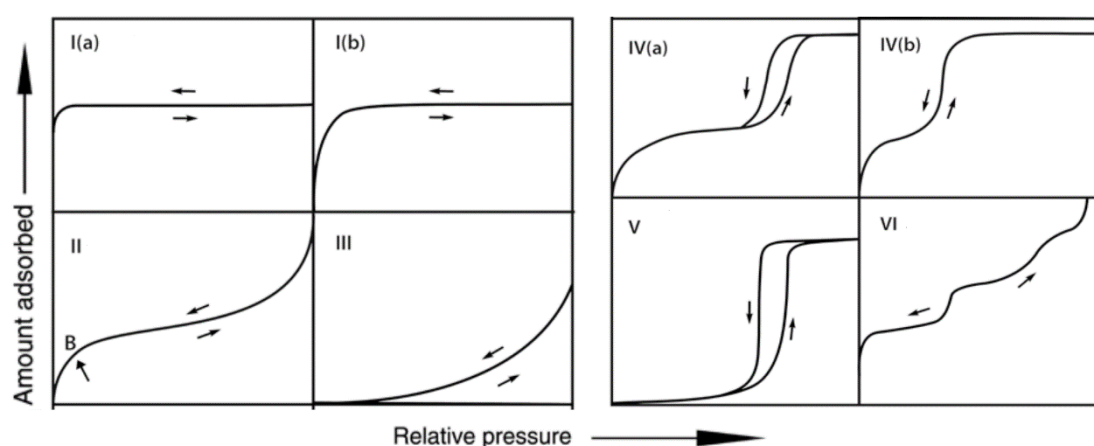
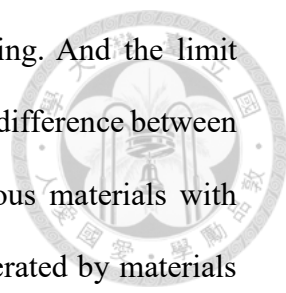


Figure 11. Classification of physisorption isotherms [68]

According to the International Union of Pure and Applied Chemistry (IUPAC), the newest classification of physisorption isotherms is shown in Figure 11 [68]. From the isotherm type, the main pore width of a specific material can be determined. IUPAC categorizes pore width into three groups: *macropores* are pores with widths exceeding about 50 nm; *mesopores* have pore widths between 2 nm and 50 nm; *micropores* mean that pores have widths less than about 2 nm [69].

Type 1 isotherms result from microporous solids that have small external surfaces, such as some activated carbons, molecular sieve zeolites, and several porous oxides. A steep rise at a low relative pressure is caused by enhanced adsorbent-adsorptive



interactions in narrow micropores, which result in micropore filling. And the limit adsorption amount is due to accessible micropore volume. As for the difference between Type I(a) and Type I(b) isotherms, the former indicate microporous materials with mainly narrow micropores (width $< \sim 1$ nm), and the latter are generated by materials possessing broader pore size distributions, from wider micropores to narrow mesopores ($< \sim 2.5$ nm) [68].

Type II isotherms result from most macroporous materials. Due to unlimited monolayer-multilayer adsorption, the branch rises abruptly at high relative pressure. The knee of the curve, where the arrow points to, is marked as Point B, and it is defined when the shape bends sharply. It usually matches the time when monolayer coverage completes, and multilayer adsorption initiates. If the curve arcs more smoothly, where Point B is less distinguishing, it suggests that monolayer coverage completion significantly overlaps with the initiation of multilayer adsorption. When relative pressure approaches 1, the thickness of the adsorbed multilayer typically occurs to increase infinitely [68].

Type III isotherms result from nonporous or macroporous solids. There is no Point B, which indicates no recognizable monolayer formation. On the surface of this kind of solid, the adsorbent-adsorbate interactions are weak and adsorbed molecules gather around most favorable sites. Comparing to Type II, the adsorbed gas amount is finite when relative pressure reaches 1 [68].

Type IV isotherms result from mesoporous adsorbents. In the beginning of the plot, it reflects the initial monolayer-multilayer adsorption on the mesopore walls. The next stage suggests pore condensation occurs, which is a phenomenon when a gas condenses to a liquid-like phase in a pore before the bulk liquid's saturation pressure. Characteristically, Type IV isotherms possess a final saturation plateau, and the length

varies. The main difference between the subtypes is hysteresis. Type IV(a) shows the hysteresis because of capillary condensation. It happens when the pore width exceeds a specific critical width, which varies according to adsorption system and temperature. For example, nitrogen (77 K) and argon (87 K) adsorption in cylindrical pores, hysteresis starts if pores are wider than ~ 4 nm. In cases where adsorbents have smaller-width mesopores, or have conical and cylindrical mesopores with closed tapered end, a Type IV(b) isotherm is noted [68].

Type V isotherms result from water adsorption on hydrophobic microporous and mesoporous adsorbents. At low relative pressure, the shape is similar to that of Type III, which also credits for weak adsorbent-adsorbate interactions, and molecules cluster at favorable sites. At higher relative pressure, pore filling occurs [68].

Type VI isotherms result from uniform nonporous surfaces. The reversible stepwise shape attributes to the layer-by-layer adsorption on this kind of material. The step-height indicates the capacity for each adsorbed layer, and the sharpness for each step varies between different systems and temperatures [68].

Within some types of physisorption isotherms, there are hysteresis loops. The form of hysteresis results from delayed condensation, which is caused by the metastability of the adsorbed multilayer and/or network effects [68]. Thus, from the type of hysteresis loops, it is possible to further conclude the pore shape and structure of a specific material.

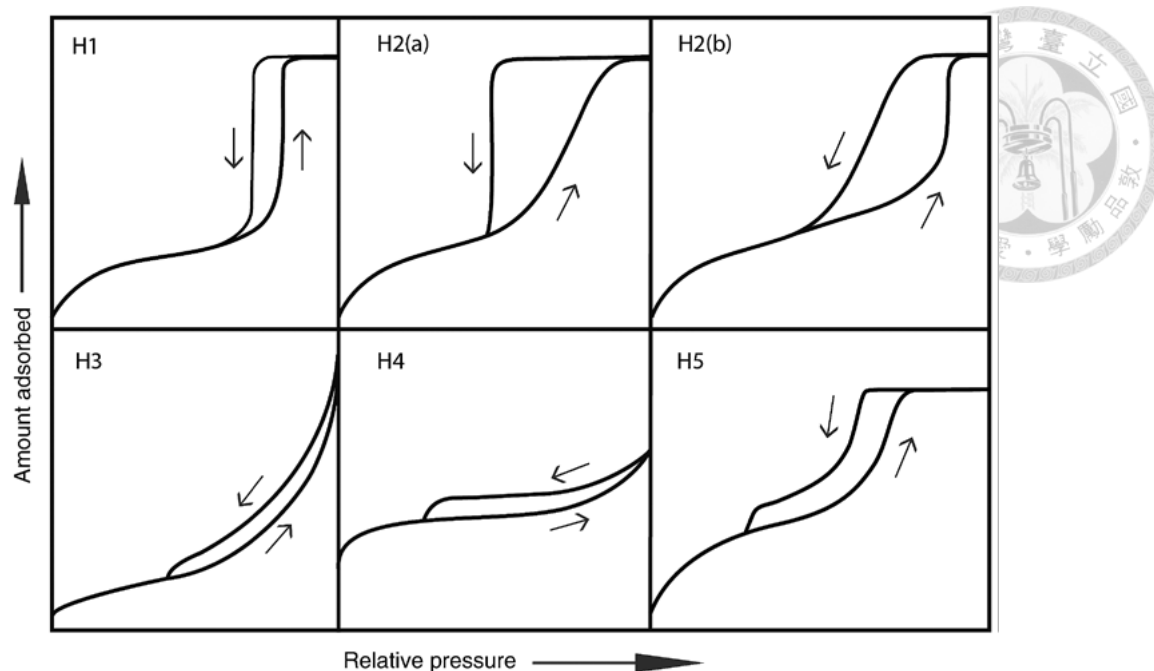


Figure 12. Classification of hysteresis loops [68]

Based on the recent classification from IUPAC, hysteresis loops types are shown in figure 2. Type H1 loop is discovered in materials that have a narrow range of uniform mesopores. The steep and narrow loop indicates delayed condensation, but network effects are usually trivial. Despite that, this type of loop has still been found in materials with networks of ink-bottle pores, where the neck width distribution resembles the pore/cavity width distribution [68].

Type H2 loops result from more complex pore structures, where network effects play a crucial role. H2(a) type has a very steep desorption branch, which is due to pore-blocking/percolation between narrow-range pore necks or to cavitation-induced evaporation. H2(b) type is related with pore blocking as well, but the neck width size distribution is rather wider [68].

Type H3 loops result from non-rigid aggregates of plate-like particles, such as certain clays, and as well as materials that possess pore networks consist of macropores with incomplete pore condensate filling. The adsorption branch is similar to a Type II

isotherm, while the desorption branch usually has a lower limit at the cavitation-induced relative pressure [68].

Type H4 loops result from narrow-slit-like pores, such as aggregated crystals of zeolites, several mesoporous zeolites, and miso-mesoporous carbons. The adsorption branch is a combination of Type I and Type II isotherms, which shows an obvious gas adsorption at a low relative pressure, indicating the micropore-filling phenomenon [68].

The physisorption above is often applied to measurement of materials' specific surface area and pore structure. As for physical adsorption in the metal ion adsorption field, it's another story.

For metal ion adsorption, physisorption mechanisms include van der Waals force, electrostatic forces [70]. Adsorbing through van der Waals force meaning that between adsorbates and adsorbents, there is no electron exchange, and the attraction is due to intermolecular attraction, which is a weak bond. In the case of metal-ion adsorption, adsorbates are adsorbed onto adsorbents when the pore size on the adsorbent has a similar scale as the adsorbates.

Electrostatic force simply means that the adsorption is based on coulomb principle. Therefore, metal ions are attracted to the adsorbent surface that carries the opposite charge. For activated carbons, according to the solution environment, below point of zero charge, positive charges are observed on the surface. Under such environment, it performs better at adsorbing hydrated metal ions that carry negative charges. On the other hand, after the point of zero charge, activated carbon carries negative charges, which make it a better adsorbent for negative hydrated metal ions [71].

2.3.2 Chemical adsorption (Chemisorption)

Chemisorption include ion exchange, complexation, and microprecipitation [70,72]. The surface of LACF consists of oxygen-functional groups and pi electrons, which are the places where chemisorption happens. For ion exchange, it happens when LACF exchanges -H on functional groups such as carboxylic acid with metal ions, allowing the construction of bond -COOM, where M indicates a metal ion. At places where the functional groups already lost the protons; then metal ions may directly chelate with the oxygen atoms. Microprecipitation mainly exists when the adsorbed metal ion is easily reduced, and it usually happens at the basal plane, where pi electrons are rich. The reaction is sometimes irreversible as the bond is too strong [72].

Chapter 3: Materials and Methods



3.1 Materials

Hardwood lignosulfonic acid sodium salt (HLS, $M_w \approx 8,000$ g/mol) from Borregaard, Sarpsborg, Norway, and poly(ethylene oxide) (PEO, $M_w = 600,000$ g/mol) from Acros, Livingston, NJ, USA were used to produce the lignosulfonate activated carbon fiber (LACF). All of the chemicals were used as received.

3.2 Methods

3.2.1 LACF Production

3.2.1.1 Electrospinning

Precursors for the LACF were HLS-PEO mixtures, which were prepared by the following steps: mixing HLS and PEO powder (HLS:PEO = 95:5 wt%) with vortex first; then dissolve the powders in deionized water under room temperature with a magnetic stirrer to generate a 20 wt% solution. The stirring speed was set to 100 rpm, and continuously stirred for 10 h. PEO and lignosulfonate are both polymers, they undergo shear-thinning as stirring time and speed increase. Thus, controlling these two parameters are important for preparing electrospinning solutions.

The apparatus was similar as those shown in the preliminary study [10]. The HLS solution was loaded into a 25 mL syringe, and charged at 15 kV DC power (EL50P0, Glassman High Voltage Inc., High Bridge, NJ, USA). The flow rate, syringe-to-collector distance, collector rotating rate, and needle gauge were set to 0.03 mL/min,

15 cm, 250 rpm, and 15 G, respectively. The electrospun HLS fibers were collected on a drum collector to form fiber mats. The whole set and the electrospun ligninosulfonate-based fiber are shown in Figure 13.

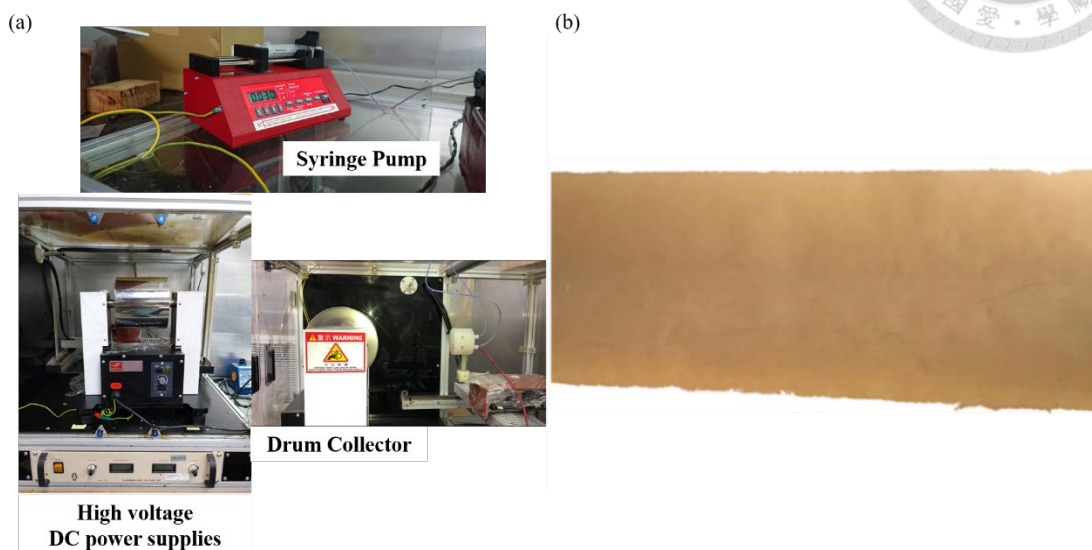


Figure 13. (a) electrospinning apparatus; (b) fabricated lignosulfonate fiber mat

3.2.1.2 Pre-oxidation, Carbonization and Activation

In this study, the LACF was fabricated through pre-oxidation in air, and a two-step carbonization/activation process as described in the preliminary research [10].

The pre-oxidation process was executed according to the following description—the fiber mat was heated to 100 °C at a rate of 1 °C/min, and hold for 30 min; then with the same rate, the temperature was raised to 300 °C, and hold for another 30 min; finally, it was cooled down to the room temperature.

After pre-oxidation, the HLS fiber mat went through the two-step carbonization/activation procedure (Figure 14). Carbonization was conducted under N₂ environment. The temperature was first raised to 400 °C at a rate of 1 °C/min, and hold for 5 min; then the as-spun fiber mat was heated to 700 °C at a rate of 12 °C/min, and hold for 1 h, followed by cooling down to the room temperature. Regarding the second

step, the carbon fiber was directly heated to 800 °C at a rate of 12 °C/min. When the goal temperature was reached, the gas flow was switched to pure CO₂, characterizing the starting point of activation, which continued for 30 min. At the end-point, the inlet gas was changed to N₂ again, and the activated carbon fiber was then cooled down to the room temperature.

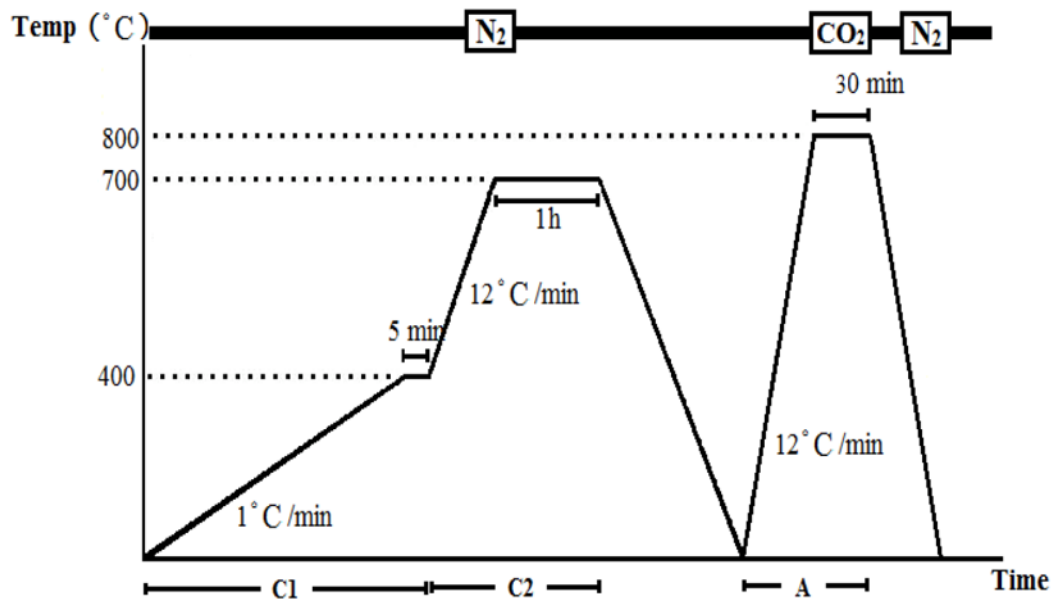


Figure 14. Two-step carbonization/activation process

3.2.2 Characterization of LACF

When it comes to the adsorption ability of activated carbon fibers, several factors have been reported to be vital, including fiber morphology [73], specific surface area, pore size distribution, and surface chemistry [74–77].

3.2.2.1 Physical characterization

Many models have been developed to explain the impacts of the porosity on adsorption. In 1995, Byrne and Marsh suggested a model for the highly defective carbonaceous structure derived from a cellulosic-type precursor. The model proposed

that the cage-like arrangements formed by defective graphene layers, when interconnected, created microporosity (molecular-sized spaces), which further resulted in intense dispersive forces within and can therefore assist an adsorption process (Figure 15) [73].

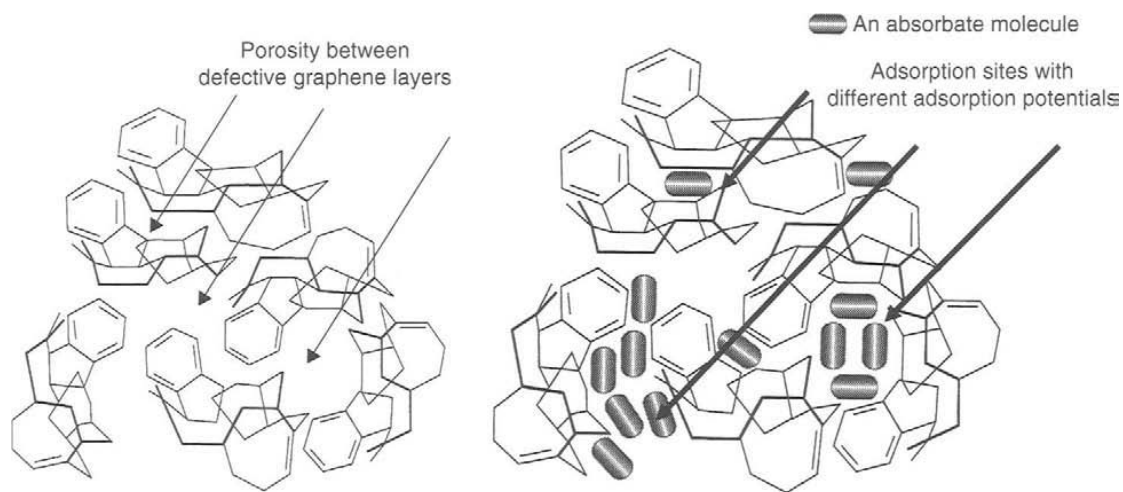
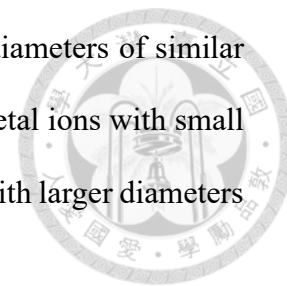


Figure 15. Possible highly defective carbonaceous structures [73]

The specific surface area (SSA) provides the information of the amount of area accessible to adsorbates. Therefore, intuitively, larger SSA usually indicates that the material has a greater potential to perform effective adsorption [77].

As for pore size distribution, overall, comparing with powdered and granular activated carbons, fibrous activated carbon normally lacks macropores, and exhibit a rather monodispersed pore size distribution [74]. The pore size of an adsorbent is critical to adsorption efficiency in two ways. First of all, as pore size decreases, the adsorption strength increases. There are two reasons for the phenomenon, the contact points between the surface of adsorbent and adsorbate increases, and the adsorption potentials for each pore increases, because as micropore width inclines to less than about twice the adsorbate's diameter, the adsorption potential for each opposing pore wall begins to overlap, merging into a larger value [74]. Secondly, it has been generally

accepted that an adsorbent is able to adsorb substances that have diameters of similar dimensions [78]. For example, Kadirvelu et al. [79] showed that metal ions with small diameter were more easily adsorbed onto micropores, while those with larger diameters (i.e. Pb(II)) were inclined to be adsorbed to mesopores.



3.2.2.1.1 Scanning Electron Microscope (SEM)

Fiber morphology was examined by a scanning electron microscope (SEM, HITACHI TM-1000, Tokyo, Japan). Before analysis, the sample was attached to an aluminum carrier with a sticker, and then sent into the chamber of the apparatus. The analysis started after the chamber was vacuumed.

3.2.2.1.2 Weight Loss

Weight loss was calculated by Equation 1. LPF stands for the product after pre-oxidation, abbreviating from “Lignosulfonate Pre-oxidized Fiber” (i.e. the fiber cloth before activation). The numerator is the weight difference before and after activation, and the denominator is the weight before activation. Weight loss was used to evaluate the production efficiency, the more, the better.

$$\text{Weight Loss(\%)} = (W_{\text{LPF}} - W_{\text{LACF}} / W_{\text{LPF}}) \times 100 \quad \text{Equation 1}$$

3.2.2.1.3 Specific Surface Area and Pore Size Distribution

Specific surface area and pore-sized distribution were measured by surface area and pore size analyzer (NT2LX-1, NOVA touchTM, Quantachrome Instruments, Boynton Beach, Florida, USA). Before analysis, the LACFs were washed with deionized water for 10 min using ultrasonic atomizer to remove tars on the surface and dried in a vacuum oven at 60 °C for 12 h. After water wash, samples were degassed at

573.15 K for 12 h using N₂ to eliminate impurities within the materials. When degas finished, analysis was followed by N₂ (at 77 K) adsorption-desorption process.

Specific surface area and pore size distribution were further calculated from the N₂ isotherm. Brunauer-Emmett-Teller (BET) equation was used to obtain the specific surface area, specifically, it computes the isotherm data in the BET linear region, where the relative pressure P/P₀ ranged from 0.05 to 0.3 [80]. Quenched Solid Density Functional Theory (QSDFT) was applied to model the pore size distribution, which only involves the adsorption branch for calculation [68].

3.2.2.1.3.1 Brunauer-Emmett-Teller Method (BET method)

Another important index for optimizing porous carbons is specific surface area [67]. The most common method to evaluate the feature is Brunauer-Emmett-Teller (BET) theory, which requires transforming the measured adsorption isotherm into a BET plot (Figure 16) [81]. From the plot, the monolayer capacity (n_m) can be determined, and through using the molecular cross-sectional area, the specific surface area can be further calculated [67]. The monolayer capacity (n_m) is calculated through Equation 2 [67,81], where n_a is the amount of gas adsorbed, expressed in moles per gram, and is related with W in the plot; C is an empirical constant that implies the attractive adsorbent-adsorbate interactions, and P/P₀ is relative pressure [81].

$$\frac{P/P_0}{n_a[1-(P/P_0)]} = \frac{1}{n_m C} + \frac{C-1}{n_m C} \cdot \frac{P}{P_0} \quad \text{Equation 2}$$

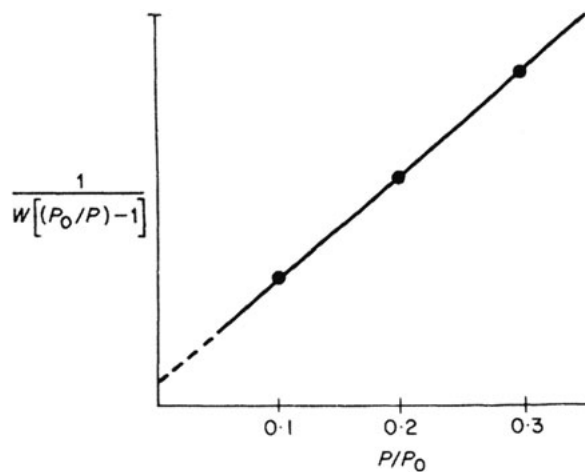


Figure 16. Typical BET plot [81]

As the equation shows, to apply BET method, the plot needs to be in a linear form [82]. Initially, Emmett and Teller discovered that various adsorbents display linear BET plots when relative pressure (P/P_0) is between 0.05 to 0.25; therefore, this range is regarded as the classical linear BET pressure range, which is applicable for macro-, and mesoporous materials (pore width $> 4\text{nm}$; basically Type II and IV(a) materials), and the BET-area can be considered as the “probe accessible area”[68]. As for microporous materials, due to the existence of micropore volume filling, which is difficult to be separated from monolayer formation at a relative low pressure (below 0.1), the traditional pressure range needs to be adjusted [67].

To find a reliable linear range of the BET plot for microporous solids, Llewellyn et al. suggested a procedure based on two criteria [82] that has been adopted by the International Organization for Standardization [83]:

- a) C needs to be positive (i.e. any negative intercept on the BET plot implies that one is outside the valid range of the BET equation);
- b) application of the BET equation needs to be limited to the range where the term $n_a[1-(P/P_0)]$ or $n_a(P_0-P)$ constantly increases with P/P_0 .

In microporous materials, the specific surface area calculated through BET equation should be regarded as “equivalent” surface area. An example is shown here with a BET plot for a microporous activated carbon fiber (ACF) [67].

As Figure 17 shows, when applying to the traditional relative pressure range, the microporous activated carbon BET plot does not display an exact linear form, which suggests that the chosen range is incorrect. Furthermore, the intercept on x axis is negative, implying that the C-constant is negative, which contradicts to the reality. Under the circumstance, the BET area is reported to be $1008 \text{ m}^2 / \text{g}$, but the data should not be used.

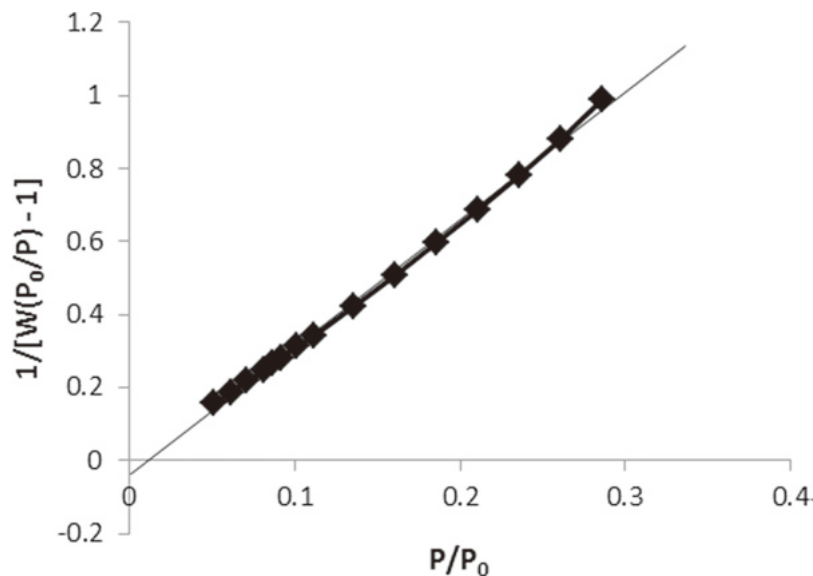


Figure 17. BET plot for an ACF adopting the classical relative pressure range (0.05–0.25)

In order to obtain a more reliable result, the method suggested by Llewellyn et al. [82] is now implemented. Through leveraging an alternative BET plot like Figure 18, where V represents the adsorbed gas volume, relating with n_a , a more proper pressure range can be determined. In this case, the range where $V[1 - (P/P_0)]$ consistently increases with P/P_0 occurs between 0.026–0.071; thus, the BET range is altered to this much lower relative pressure.

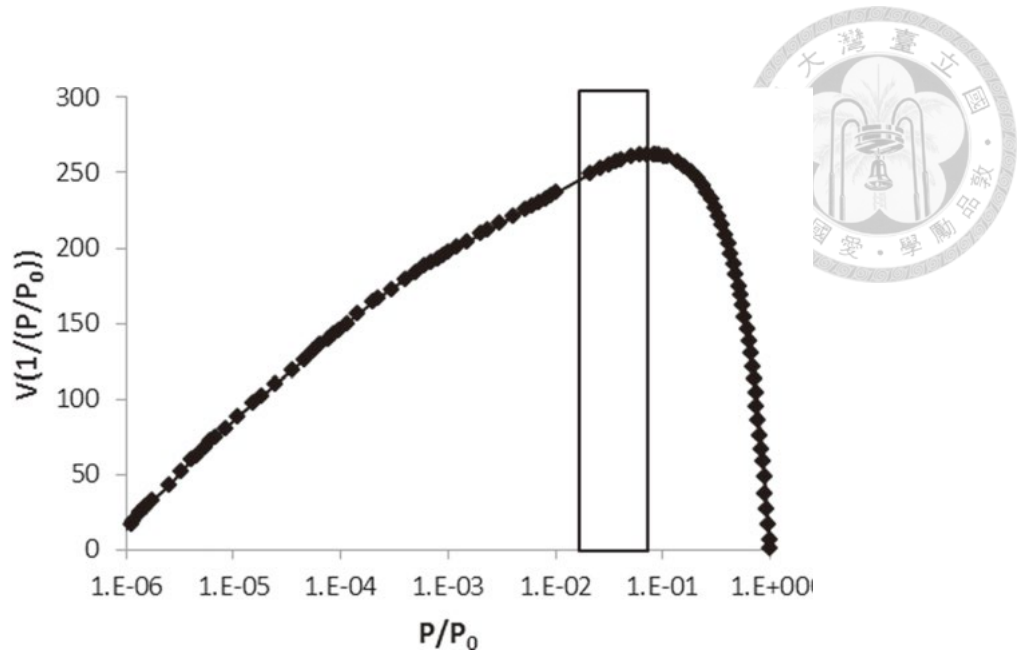


Figure 18. Plot of P/P_0 vs. $V[1-(P/P_0)]$

Figure 19 shows the BET plot result under the range of 0.026–0.071, which has a higher correlation coefficient, and the resulting “equivalent” BET area is 1167 m^2/g . Although it cannot be considered as the true surface area, the method along with BET equation improve the reproducibility of BET area determination for microporous materials and the comparison of BET area data between labs [67].

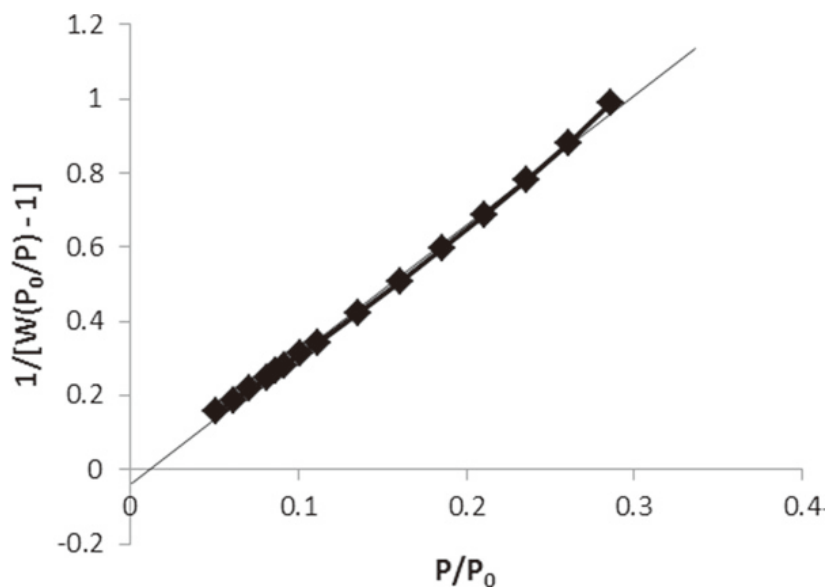


Figure 19. BET plot for the same ACF adopting the criteria



3.2.2.1.3.2 Quenched solid density functional theory (QSDFT)

Quenched solid density functional theory is an improved method for pore size distribution calculations for micro- and mesoporous materials [84]. Before QSDFT, the most popular pore-size distribution (PSD) analysis for these materials was nonlocal density functional theory (NLDFT). However, the disadvantage for NLDFT is it assumes that the solid surface of a material is molecularly smooth, and predicts that the adsorption isotherms contain pronounced layering steps [67]. QSDFT resolves the problem. It takes the surface heterogeneity effects into account, and the solid is treated as one of the components of the adsorbate-adsorbent system [67].

The pore-size distribution calculation is based on a generalized adsorption equation (GAE) as Equation 3 shows, and it is also called integral adsorption equation:

$$N_{\text{exp}}(P/P_0) = \int_{H_{\text{min}}}^{H_{\text{max}}} N_{\text{QSDFT}}(P/P_0, w) f(w) dw \quad \text{Equation 3}$$

where H_{min} and H_{max} are the minimum and maximum pore sizes in the kernel. The kernel $N_{\text{QSDFT}}(P/P_0, w)$ represents a sum of theoretical isotherms in pores of various diameters, which include the whole range of micro- and mesopores accessible in the adsorption experiment [84].

The scheme of QSDFT theory for generating a pore size distribution plot is correlate the kernel of theoretical adsorption (or desorption) isotherms with the experimental adsorption (desorption) isotherms through the integral adsorption equation, as Figure 20 displays [67].

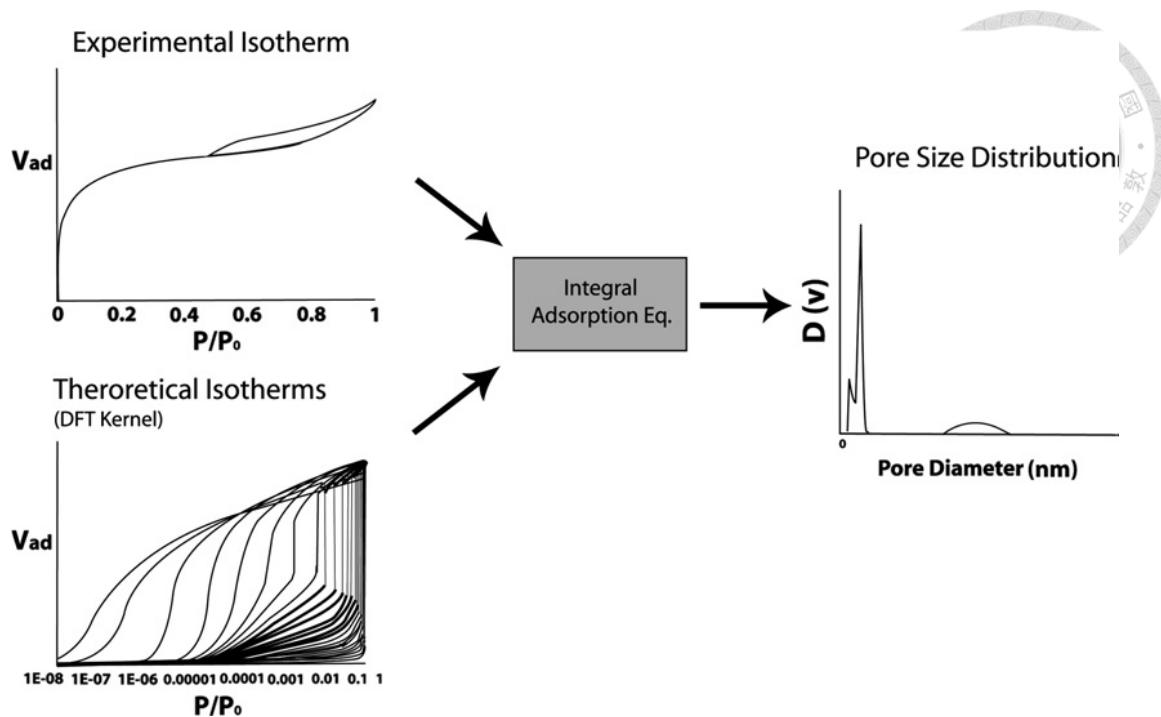


Figure 20. Scheme of QSDFT model [67]

3.2.2.2 Chemical characterization

Some ions, such as heavy metals, their adsorption behaviors seem to be described as “trapped on the surface of the basal planes”, depending mostly on the specific surface area and porosity of carbon; other ions, for instance, alkali, alkali-earth and several transition ions are adsorbed through cationic exchange mechanism, which depends on the surface chemistry of activated carbon fiber [76].

However, as activated carbon fiber goes through the heat treatment in an inert atmosphere, specifically N_2 , the oxygen-containing functional groups will be removed, while basic delocalized π -electrons on the condensed polyaromatic sheets will develop [74,85,86]. Therefore, in these cases, the graphene structures, which contain rich π -electrons play an important role during adsorption. For example, the adsorption mechanism of ions such as platinum, gold, and silver, is the chemical adsorption-

reduction process. Because of their high redox potential, they are mostly adsorbed and reduced through obtaining the π -electrons [76].

In the following sessions, LCF represents samples without activation, LACF30 and LACF60 respectively is the abbreviation for samples activated for 30 and 60 minutes.

3.2.2.2.1 Zeta Potential and Point of zero charge

The instrument used was Particle Size and Zeta Potential Analyzer (Malvern, Zetasizer Nano). Before the measurement, LCF, LACF30, and LACF60 were respectively mixed with distilled water to create a 0.05% (w/v) suspension. For each sample, duplicate tests were implemented, and the average zeta potential was recorded.

For point of zero charge, only LACF60 was examined. Suspensions with various pH were prepared with HNO₃ and NaOH, including pH = 1.0, 2.1, 3.2, 4.4, and 5.6. For both zeta potential and point of zero charge, the suspensions were stirred in the ultrasonic vibrator for 24 h before being examined.

3.2.2.2.2 Surface functional groups (Qualification/Quantification)

3.2.2.2.3.1 Fourier transform infrared (FTIR) spectroscopy

Fourier Transform Infrared Spectrometer from Perkin Elmer Spectrum 100 was used to examine the surface functional groups. Scanning ranged from 450–4000 cm⁻¹. For the amount of KBr used, because carbon usually has strong signal, the mix of LACF:KBr for was 1:100. After mixing, the sample was pressed into a pellet.

3.2.2.2.3.2 X-ray Photoelectron Spectroscopy (XPS/ESCA)

XPS can show the proportion of each functional group. The instrument used was from ULVAC-PHI PHI 5000 Versaprobe II. Peak deconvolution method and the area

calculation was implemented by XPSPEAK version 4.1 software, consisting of two steps [87]. First, position, Gaussian: Lorentzian ratio (G:L), and full width at half maximum (FWHM) were fixed to do 100 iterations. Seven peaks were deconvoluted in total, each was arbitrarily fixed according to Table 1 [88]. G:L ratio was fixed at 80%, and FWHM was fixed at 1.5. Then, position and G:L ratio limit was freed, and 100 iterations were performed again.

Table 1. Fixed positions in peak-deconvolution-step-1 [88]

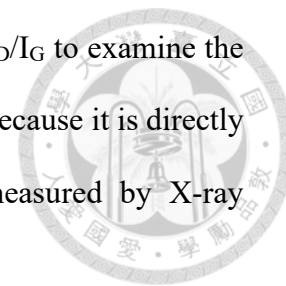
Peak ID	Assignment	Fixed position
1	vacancy carbon	283.8
2	conjugated carbon	284.9
3	non-conjugated carbon	285.9
4	phenol,lactone,ether	286.6
5	quinone,pyrone	287.7
6	carboxyl,lactone	289.5
7	pi-pi*	291.4

3.2.2.2.3.3 Raman Spectroscopy

Raman spectroscopy was carried out to determine the carbon structure within the material. The analysis progressed under room temperature, using a custom-built 785 nm Confocal Micro Raman System, and the spectrophotometer, MR-Spec-Red (focal length: 20 cm; grating: 1200 1/mm; detector: Andor iVac CCD). The laser power was set to 10mW; exposure time was 30 seconds for each scan, while each measurement contained 4 scans; the resolution was 1 cm^{-1} ; the scan range was fixed between 880—1830 cm^{-1} .

In the Raman spectrum, two characteristic peaks for activated carbon fibers are I_D and I_G . I_D appears around 1360 cm^{-1} , which represents for the deflection of crystalline structure [89]; I_G locates around 1580 cm^{-1} , which indicates the existence of C=C bonds

that mainly construct the graphene structure. It is common to use I_D/I_G to examine the graphene structure ratio within an activated carbon fiber material, because it is directly proportional to the crystalline size along basal plane ($1/L_a$) measured by X-ray Diffraction (XRD) [90].



3.2.3 Characterization of LACF with metal ion

3.2.3.1 Energy dispersive spectroscopy (EDS)

Energy dispersive spectroscopy was implemented along with SEM. It is able to identify the surface elemental composition for a certain selected area within a material. Samples being examined include the LACF with and without adsorbed ions. The ones after metal ion adsorption are abbreviated as LACF-M. Among them, LACF with Cu(II) is called LACF-Cu, while LACF with Au(III) is called LACF-Au.

3.2.3.2 Fourier transform infrared (FTIR) spectroscopy

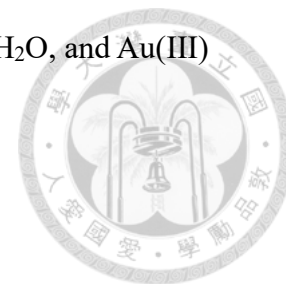
Surface functional groups were again qualified by FTIR after adsorption, for the purpose of examining whether the peaks shift or not, which served as another evidence to verify the adsorption mechanism. Furthermore, LACF-M after desorption were analyzed as well. The list of samples being compared are LACF, LACF-Cu, desorbed LACF-Cu, LACF-Au, and desorbed LACF-Au.

3.2.4 Mono-component Metal Recovery experiments (Batch/Column)

3.2.4.1 Batch Adsorption tests

The amount of activated carbon and solution used was suggested by ASTM D3860 [91]. For adsorbate concentration between 10 to 100 ppm, solution sample volume (mL) / carbon dry weight equals to 100 (mL)/ 0.04(g).

For metal ion preparation, Cu(II) was prepared from $\text{CuSO}_4 \cdot 5\text{H}_2\text{O}$, and Au(III) was prepared from HAuCl_4 . Chemicals were used as received.



Cu(II) /Au(III) adsorption according to various pH

0.4 mM Cu(II) and Au(III) solution were respectively prepared, for the latter, due to convenience, the powders were first dissolved in HCl, and then dilute for further usage. NaOH and HNO_3 were used to adjust the solution to the desired pH values. After solution was prepared, LACFs were added right after. The suspension was shaken in an incubator for 1 day until equilibrium was reached. After the adsorption, LACF was filtered off through 0.45 μm syringe filter. Filtered solution was examined through atomic absorption spectrum to calculate the adsorption capacity.

Cu(II) / Au(III) adsorption according to various concentration (Isotherm)

A. Experimental details for Cu(II) adsorption are as follows:

- (1) Prepared pH = 5.4 buffer solution 0.05 M, 2 L with $\text{CH}_3\text{COOH}_{(\text{aq})}/\text{CH}_3\text{COONa}_{(\text{s})}$ and distilled water. The main purpose of using buffer was to maintain the same adsorption environment during the whole process.
- (2) Dissolved $\text{CuSO}_4 \cdot \text{H}_2\text{O}_{(\text{s})}$ with the pH = 5.4 buffer to prepare Cu(II) stock solution 1.0 mM (deriving from CuSO_4 250 ppm), 2 L.
- (3) Diluted the Cu(II) stock solution to desired concentrations with the buffer. Concentrations used were: 0.04, 0.10, 0.17, 0.23, 0.30, 0.36, 0.42, 0.49, 0.62, 0.74, 0.87, 1.00 mM. Prepared 100 mL for each concentration.
- (4) Prepared 12 clean vials. For each concentration, measured 50 mL, and poured it into a 50×90 mm 110 mL vial. At the same time, measured 10 mL for future atomic absorption spectroscopy tests to determine the Cu(II) concentration before adsorption. After this step, there would be 12 vials with different concentrations.

- (5) Added 0.02 g LACF into each vial.
- (6) Put 12 vials on a shaker incubator inside a programmable temperature and humidity tester to keep the adsorption test under a 30 °C environment.
- (7) Shook all the vials for 24 h to ensure the adsorption reaches the equilibrium state.
- (8) After 24 h, separated the LACF and Cu(II) solution with syringe filters.
- (9) Diluted the post-adsorption Cu(II) solution to 3 different concentrations for atomic absorption spectroscopy tests.



B. Experimental details for Au(III) adsorption are as follows:

- (1) Prepared pH = 2.17 buffer solution 2 L with 0.2 M HCl /0.2 M KCl and distilled water. The main purpose of using buffer was to maintain the same adsorption environment during the whole process.
- (2) Dissolved one bottle of AuCl_{3(s)} (500 mg) in 500 mL 0.1 M HCl to prepare 1000 ppm stock solution.
- (3) Diluted the Au(III) stock solution to desired concentrations with the buffer. After mixing the stock solution with the buffer, the pH environment was changed to 1.79. Concentrations used were: 0.04, 0.10, 0.17, 0.23, 0.30, 0.36, 0.42, 0.49, 0.62, 0.74, 0.87, 1.00 mM. Prepare 100mL for each concentration.
- (4) Prepared 12 clean vials. For each concentration, measured 50 mL, and poured it into a 50×90 mm 110 mL vial. At the same time, measured 10 mL for future atomic absorption spectroscopy tests to determine the Au(III) concentration before adsorption. After this step, there would be 12 vials with different concentrations.
- (5) Add 0.02 g LACF into each vial.
- (6) Put 12 vials on a shaker incubator inside a programmable temperature and humidity tester to keep the adsorption test under a 30 °C environment.
- (7) Shook all the vials for 24 h to ensure the adsorption reaches the equilibrium state.

- (8) After 24 h, separated the LACF and Au(III) solution with syringe filters.
- (9) Diluted the post-adsorption Au(III) solution to 3 different concentrations for atomic absorption spectroscopy tests.



Cu(II) / Au(III) adsorption according to various contact time (Kinetics)

The concentration was chosen according to ASTM D3860 [91], which should be adjusted to obtain 10–85% adsorbate removal.

A. Experimental details for Cu(II) adsorption are as follows:

- (1) Prepared pH = 5.4 buffer solution 0.05 M, 2 L with $\text{CH}_3\text{COOH}_{(\text{aq})}/\text{CH}_3\text{COONa}_{(\text{s})}$ and distilled water. The main purpose of using buffer was to maintain the same adsorption environment during the whole process.
- (2) Dissolved $\text{CuSO}_4 \cdot \text{H}_2\text{O}_{(\text{s})}$ with the pH = 5.4 buffer to prepare Cu(II) stock solution 1.0 mM (deriving from CuSO_4 250 ppm), 2 L.
- (3) Diluted the Cu(II) stock solution to desired concentrations with the buffer. Considered the result from isotherm test, the concentration chosen was 0.42 mM (2L).
- (4) Prepared 15 clean vials (50×90 mm 110 mL). Measured 50 mL Cu(II) solution and poured it into each vial. At the same time, measured 10mL for future atomic absorption spectroscopy tests to determine the Cu(II) concentration before adsorption. After this step, there would be 15 vials all with the same concentration.
- (5) Added 0.02 g LACF into each vial.
- (6) Put 15 vials on a shaker incubator inside a programmable temperature and humidity tester to keep the adsorption test under a 30 °C environment.
- (7) Shook the vials for various time duration. The time chosen was: 2, 5, 10, 15, 20, 30, 45, 60, 75, 90, 120, 180, 250, 360, 480, 1440 min.

(8) When the time was reached, separated the LACF and Cu(II) solution with syringe filters.

(9) Diluted the post-adsorption Cu(II) solution to 3 different concentrations for atomic absorption spectroscopy tests.



B. Experimental details for Au(III) adsorption are as follows:

(1) Prepared pH = 2.17 buffer solution 2 L with 0.2 M HCl /0.2 M KCl and distilled water. The main purpose of using buffer was to maintain the same adsorption environment during the whole process.

(2) Dissolved one bottle of AuCl_{3(s)} (500 mg) in 500 mL 0.1 M HCl to prepare 1000 ppm stock solution.

(3) Diluted the Au(III) stock solution to desired concentrations with the buffer. Considered the result from isotherm test, the concentration chosen was 0.42 mM (2L). After dilution, the pH changed to 1.79.

(4) Prepared 15 clean vials (50×90 mm 110 mL). Measured 50 mL Au(III) solution and poured it into each vial. At the same time, measured 10 mL for future atomic absorption spectroscopy tests to determine the Au(III) concentration before adsorption. After this step, there would be 15 vials all with the same concentration.

(5) Added 0.02 g LACF into each vial.

(6) Put 15 vials on a shaker incubator inside a programmable temperature and humidity tester to keep the adsorption test under a 30 °C environment.

(7) Shook the vials for various time duration. The time chosen was: 2, 5, 10, 15, 20, 30, 45, 60, 75, 90, 120, 180, 250, 360, 480, 1440 min.

(8) When the time was reached, separated the LACF and Au(III) solution with syringe filters.

(9) Diluted the post-adsorption Au(III) solution to 3 different concentrations for atomic absorption spectroscopy tests.



Cu(II) / Au(III) desorption/re-adsorption

Under pH = 5.4, Cu(II) adsorption was performed, and the adsorption reaction time was set for 240 min according to the kinetic test. After the first adsorption equilibrium, LACF and the solution were separated, and LACF was sent to the oven to dry at 60 °C for 5.5 h. After drying, the sample was then added to HNO₃ for desorption. Desorption lasted for another 6 h. Then, the sample was again filtered and sent into oven to dry at 80 °C for 2.5 h. The cycle was repeated for 3 times, and for each cycle, the solution concentration was measured before and after adsorption.

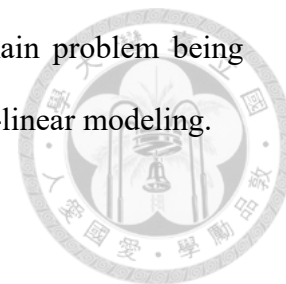
Regeneration test was similar for Au(III), but the adsorption reaction time was set to 360 min, and the desorption time was altered to 8 h. The recover reagent used was a mixture of NaOH and acetone.

Batch Adsorption data analysis

Simpler models are better, so for both isotherm and kinetic models, only models with just 2-3 parameters are used. The advantage of using nonlinear fitting is that it won't break the error distribution structure for the experimental data. However, the disadvantage is that the parameters are difficult to determine because the local minimum cannot be easily calculated, leading to the unstableness for parameter estimation. Therefore, algorithm and weight method chosen for fitting are quite important. Here, the Levenberg-Marquardt iteration algorithm was used.

Many past studies have focused on linear modeling [92,93]. Although linear regression is easier when it comes to model interpretation, and it does not suffer from the difficulty of local minimum determination, it has another disadvantage. The change

of the error structure after transforming the data points is the main problem being discussed in past literatures [93,94]. Hence, this study adopted non-linear modeling.



Isotherm models

Adsorption isotherm models are one of the important tools to estimate adsorption capacity, and the adsorption mechanism. In this study, the models used for fitting were Langmuir, Freundlich, and Redlich-Peterson model.

Langmuir isotherm model assumes that adsorption happens on a homogeneous surface. It is suitable for low concentration adsorption and has four assumptions [95,96]:

- (1) There are many activation sites on an adsorbent, and each of them can adsorb one adsorbate.
- (2) Every adsorption site has the same affinity to the adsorbate.
- (3) Each adsorbate's adsorption behavior is independent of one another
- (4) The maximum adsorption capacity is reached when every adsorption site adsorbs one layer of adsorbate.

The relationship between adsorbate and the equilibrium adsorption capacity can be described in Equation 4,

$$q_e = \frac{Q_{\max} b C_e}{1 + b C_e} \quad \text{Equation 4}$$

where q_e (mmol/g) is the equilibrium adsorption capacity; Q_{\max} is the maximum adsorption capacity (mmol/g), which also equals to K_R/a_R , the Redlich-Peterson parameters that will be introduced in the later paragraphs; C_e (mmol/L) is the metal ion equilibrium concentration; b is the Langmuir constant related to the energy of adsorption. Although it simplifies the adsorption behavior, it is conveniently used for calculating the adsorption energy.

Freundlich model [95,96] is useful when the adsorbate has a high concentration. It assumes that adsorption happens on a heterogeneous surface, where the adsorption heat distributes non-uniformly all over the surface, and the model can account for multiple-layer adsorption. The relationship is described in Equation 5.

$$q_e = K_F C_e^{1/n} \quad \text{Equation 5}$$

where q_e (mmol/g) is the equilibrium adsorption capacity; K_F is the Freundlich constant (mmol/g)(L/mmol)^{1/n}, which also equals to K_R/a_R ; C_e (mmol/L) is the metal ion equilibrium concentration; n is the heterogeneity factor, and it is equivalent to $1-\beta$, the constant fitted from the following Redlich-Peterson model.

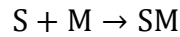
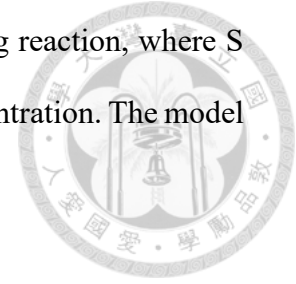
Redlich-Peterson (R-P) mode [96] can be used when the adsorbate concentration is either high or low. For high concentrations, the model is simplified to Freundlich model, on the other hand, in low concentrations, when $\beta=1$, the model is reduced to Langmuir model. The relationship between Redlich-Peterson and Freundlich, or Redlich-Peterson and Langmuir is called nested. The model is described in Equation 6.

$$q_e = \frac{K_R C_e}{1 + a_R C_e^\beta} \quad \text{Equation 6}$$

where q_e (mmol/g) is the equilibrium adsorption capacity; K_R (L/g) and a_R (L/mmol) are the R-P isotherm constants; C_e (mmol/L) is the metal ion equilibrium concentration; β is the R-P isotherm exponent, which is dimensionless and lies between 0 to 1.

Kinetic models

Pseudo-first kinetic model [97–99] is defined by the following reaction, where S equals to the adsorbent surface, and M equals to the adsorbate concentration. The model can be described as Equation 7.



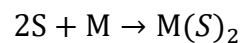
The model has four assumptions:

- (1) Adsorption does not involve the interaction between adsorbate.
- (2) Adsorption energy depends on how much the adsorbent surface was covered by the adsorbate.
- (3) Maximum adsorption capacity equals to a single layer adsorption.
- (4) M is static.

$$q_t = q_e(1 - \exp^{-k_1 t}) \quad \text{Equation 7}$$

where q_e and q_t (mmol/g) respectively represents for the adsorption capacity at equilibrium t_e and time t (min); k_1 (min^{-1}) is the pseudo-first-order rate constant.

Pseudo-second kinetic model [100] is defined by the reaction below, where S equals to the adsorbent surface, and M is equivalent to the adsorbate concentration. The model assumes that the rate-limiting step may involve chemical adsorption that is related with sharing or exchanging electrons between adsorbates and adsorbents. The relationship is described in Equation 8.



$$q_t = \frac{k_2 q_e^2}{1 + k_2 q_e t} \quad \text{Equation 8}$$

Chapter 4: Results and Discussion



4.1 Characterization

4.1.1 Physical Characterization

4.1.1.1 LACFs fiber morphology

Figure 21 - Figure 22 are the SEM photos from LACFs, it is clearly shown that fibers went through high temperature carbonization and activation may fuse together, implying that fiber diameters vary, and could further induce various pore sizes.

Figure 21 shows the difference between water-washed fibers (b), and those without water wash (a). It is obvious that after water wash, tars and salt crystals [101] on the surface of the fibers were greatly reduced, which was helpful for adsorption because fewer pores were blocked by tars. However, the fact that there were still tars left on the fiber surface implied that the water wash period could be longer, with a view to obtaining smoother and cleaner fibers.

Figure 22 displays a clear morphology of the LACF. The fibers appear to be crispy, which are the evidence of high-temperature carbonization. Besides, the crispy defective fibers were crossing each other, forming a nest/cage-like structure. This defective nest/cage-like structure could create dispersive forces that assist the adsorbent to get adsorbates [73].

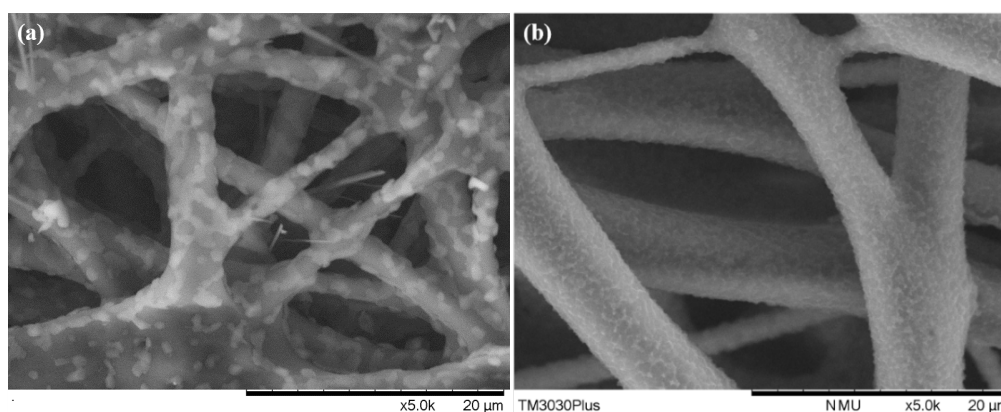


Figure 21. LACFs (a) without water wash; (b) after water wash for 10 mins

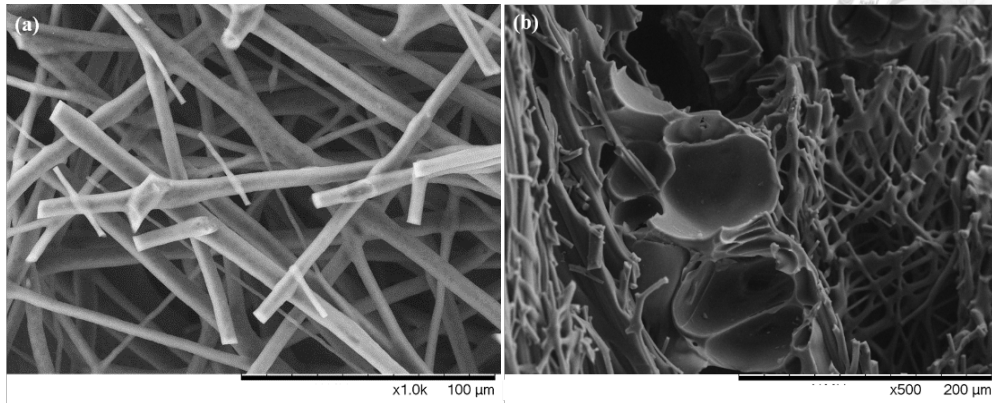


Figure 22. LACF morphology (a) nest-like; (b) cage-like

4.1.1.2 Specific surface area and pore size distribution

Figure 23 is the typical N_2 (77.35 K) isotherm from LACF. According to IUPAC's (International Union of Pure and Applied Chemistry chemical nomenclature) definition [68], The mild difference between Figure 23 and the type IV(a) curve shown in IUPAC's report was that, the initial knee part (where relative pressure is between 0.0—0.2) here was not as bent. Therefore, it implied that, aside from mesopores, other kinds of pore size may exist as well, which can be certified by the pore size distribution analysis in the later paragraphs.

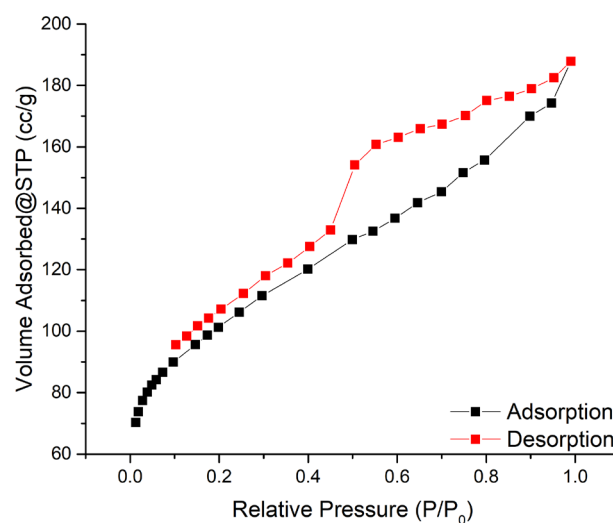


Figure 23. Typical N_2 (77.35 K) adsorption-desorption isotherm of LACF

On top of isotherm shape, the pattern of the hysteresis loop also characterizes the pore structure. This type of hysteresis loop is akin to that of H2-b type referring to IUPAC [68]. The desorption branch decreased abruptly around 0.50, which may be caused by pore-blocking, indicating that there were ink-bottle pore connections within the materials, whose bottle-neck size distributed rather widely [68].

From the isotherm, specific surface area was further calculated by the BET equation. Comparing between samples without activation (LCF), with 30-min activation (LACF30), with 60-min activation (LACF60), the result is shown in Figure 24. LACF60 had the highest specific surface area; however, because the variance was rather large, it did not show significant difference from LACF30. It was verified that activation helped increase specific surface area.

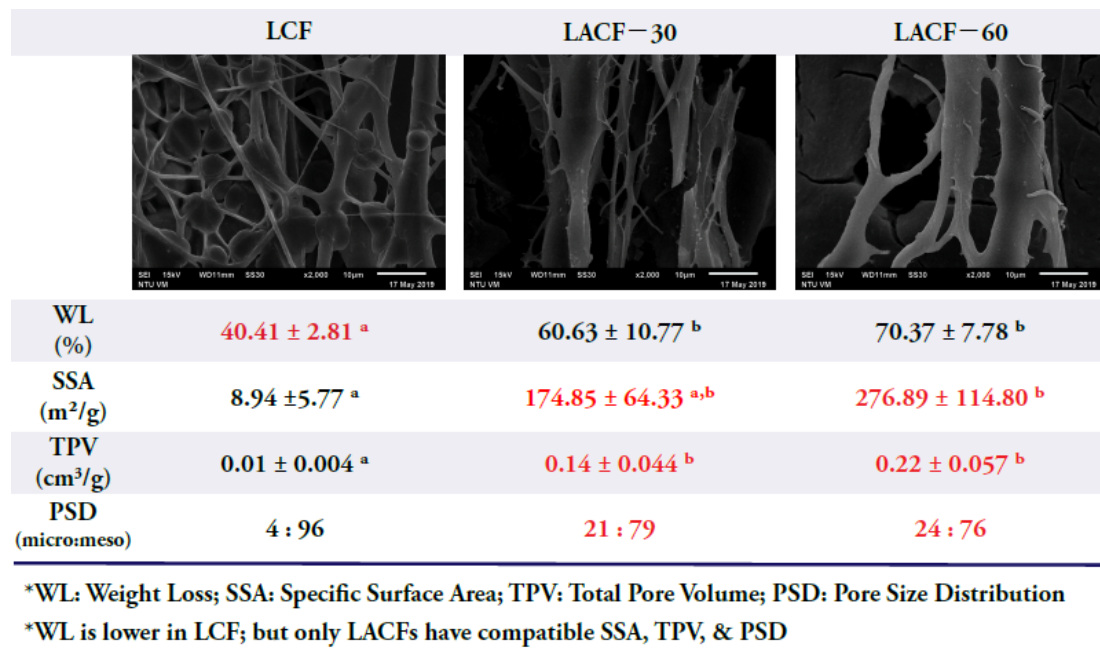


Figure 24. Physical characterization of LCF, LACF30 and LACF60

QSDFT model was used to compute pore volume and simulate the pore size distribution from the isotherm. The largest pore volume obtained from the sample was near 0.22 ± 0.057 cm³/g, which was fewer than commercial activated carbon (0.56–

1.20 cm³/g), but compatible enough to similar biosorbents. Again, the total pore volume was larger in samples that were activated but did not show significant difference between LACF30 and LACF60.

For the pore size distribution, from Figure 25, it could be observed that, except for mesopores, micropores existed as well. To be more specific, most of the pore size distributed between 1.6–20 nm. By calculation, the LACFs micro/meso- pore ratio is around 25:75. From application's point of view, usually adsorbents can adsorb substrates that have similar diameters with it. For example, the LACF can be a useful adsorbent for metal-ion adsorption from waste water, because hydrated metal ions' diameters are mostly within the micropore or mesopore region [102].

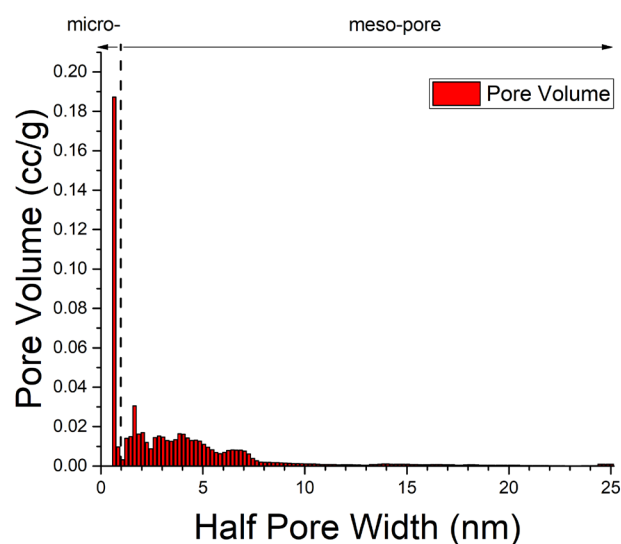


Figure 25. QSDFT pore size distribution

As for the weight loss, according to Figure 24, activation for longer time indeed caused higher weight loss. In LACF60 samples, it could reach as high as 70%, however, it is reasonable for physical activated carbon fibers. The low yield rate is a trade-off for higher specific surface area and better pore structures. All in all, activated samples won over carbon fibers, but longer activation time on average might not lead to better physical features. In the next session, chemical characterization was used to further

distinguish the activated sample, so as to pick the optimized one for further adsorption application.



4.1.2 Chemical Characterization

4.1.2.1 Zeta Potential and Point of zero charge

The result for zeta potential and point of zero charge are shown in Table 2 and Figure 26 respectively. Comparing between non-activated and activated samples, LCF had larger zeta potential. The reason may lie in that, zeta potential is determined by both minerals and organic compounds [103]. As LCF endured shorter and lower-temperature heat treatment, more minerals may be left, which offset the lack of organic compounds and contributed to the zeta potential. The assumption could be further verified through elemental analysis, where LCF possessed the highest residuals other than C, H, O, and N.

Table 2. Zeta potential of CF and LACF

	LCF	LACF-30	LACF-60
Zeta potential	-44.65	-36.65	-40.05

For LACF-30 and LACF-60, the latter had higher zeta potential. As activation time increases, the oxygen-containing surface functional groups may increase. These organic compounds may carry negative charge when suspended in dH₂O and contribute to the zeta potential.

In terms of point of zero charge (PZC), i.e. the pH point where the zeta potential equals to zero, LACF-60 was used to examined. According to Figure 26, the PZC is around 3.5. Above the PZC, the surface carries negative charges. When initial pH was around 6, the zeta potential could reach as negative as -20 mV and reach +20 mV otherwise.

The low PZC may be related with the dissociation of carboxylic groups [104]. Carboxylic groups bonded with aromatic rings have a pKa around 4.2, meaning that as pH gets larger than pKa, more hydrogen atoms leave the carboxylic groups, and thus create more negative surface charges, accounting for the steep slope between pH 3-4.

If electrostatic force between surface charge and carbon metal ions is the adsorption mechanism, for Cu(II), adsorption should perform better in the region where the initial pH is larger than 3.5. In contrast, as Au(III) exists in the solution in AuCl_4^- form, high adsorption capacity could be observed in the acidic region.

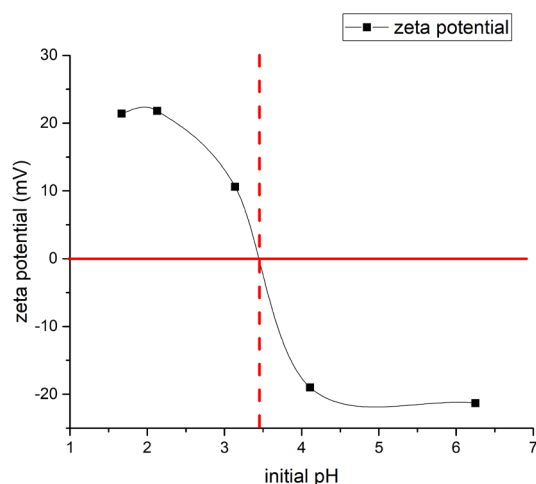


Figure 26. Point of zero charge

4.1.2.2 Surface functional groups

FTIR(Qualification)

In this session, because LACF with 30 and 60-min activation both had the same trend, only the latter one is displayed. Peak assignment for lignosulfonate, LCF, and LACF are shown in Figure 27 and Table 3.

Overall, surface functional group number decreased after lignosulfonate was carbonized, and increased after activation. The rather low intensity in LCF may also result from the fact that black carbon fibers have high absorbance [105]. Initially, the

raw material lignosulfonate had 11 obvious peaks: peak around 3428 cm^{-1} indicated O-H stretching vibration, 2937 and 2851 cm^{-1} respectively showed C-H stretching vibration in methyl and methylene groups, 1610 - 1421 cm^{-1} originated from aromatic skeletal vibrations, 1210 resulted from C-O stretching, 1040 cm^{-1} and 621 cm^{-1} were the features for S—O vibrations in sulfonate groups [106–109]. After carbonization and activation, these peaks' intensities changed and the positions shifted, which corresponded to previous research [1].

Comparing between lignosulfonate and the other two samples, the main difference happened at 3428 cm^{-1} and 500 - 1741 cm^{-1} region. The peak intensity at 3428 cm^{-1} largely decreased, meaning that OH groups in LCF and LACF decreased, which contributed to their hydrophobic property. In the 1000 cm^{-1} region, starting from around 1731 cm^{-1} , where oxygen-containing functional groups C=O stretching peaks appeared [70], LCF and LACF had similar trends. LACF's peaks had higher intensity, and the main difference happened around 1600 , 1400 and 1100 cm^{-1} , indicating that there were more oxygen-containing functional groups in LACF.

At around 1600 cm^{-1} , the peak represented C-O from aromatic rings, which was more obviously observed in LACF, as it is a feature for oxygen-containing functional groups. The peak around 1400 cm^{-1} could prove the existence of phenolic groups, which was observable in LCF and LACF, verifying that phenolic groups were stable during heat treatments.

The peak at around 1100 cm^{-1} , originally was at 1210 cm^{-1} for lignosulfonate, it shifted in both CF and LACF. The reason may result from the different kind of C-O bond. In lignosulfonate, the C-O bonds mostly exist in G & S type lignin, while in LCF and LACF, C-O bonds were also used to crosslink long chains. 1040 cm^{-1} had a more complex combination, in lignosulfonate it represented the sulfonate groups; however,

in LCF and LACF, the shape and intensity varied. In LCF, the small peak might imply the decrease in sulfonate groups, as in LACF, it can be also be contributed by the anhydride groups [110,111]. The persistence of sulfonate groups even after activation may enhance the adsorption capability of LACF.

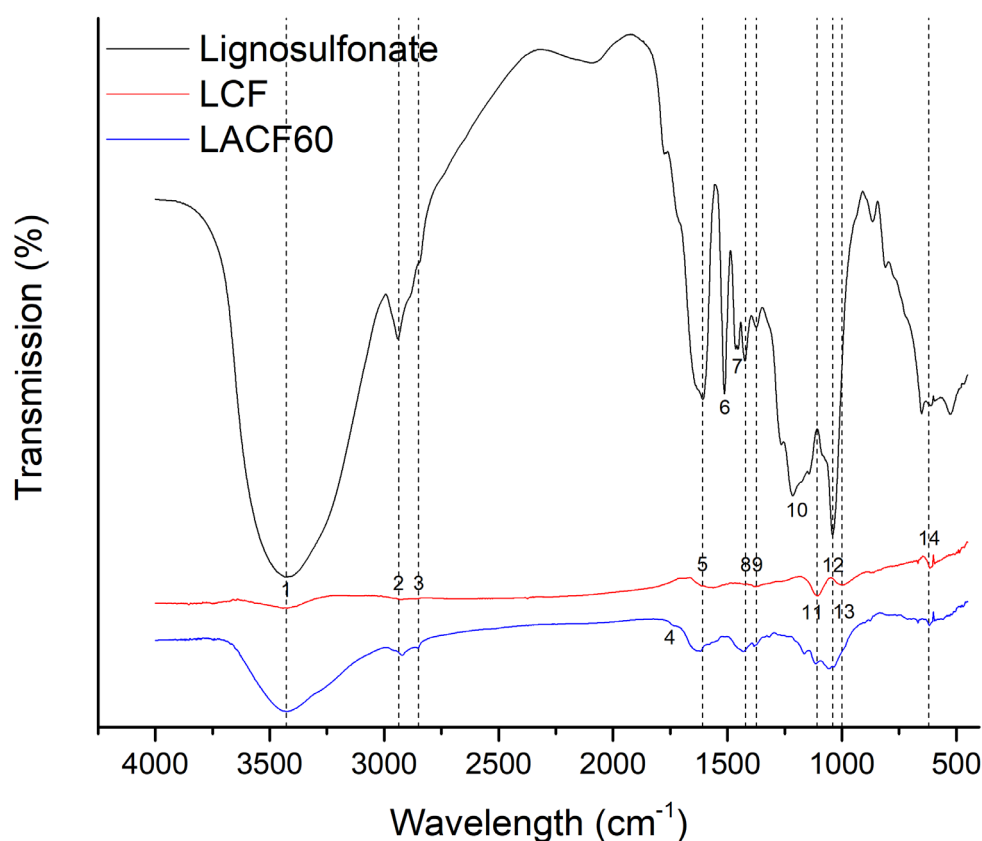
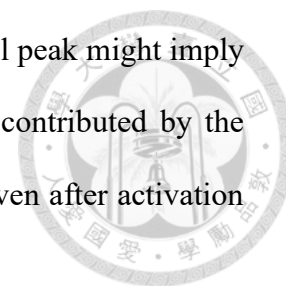
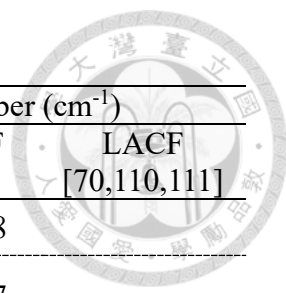


Figure 27. FTIR spectrum of LACF

From the FTIR result, a scheme for the chemical structure change from lignosulfonate to LACF is proposed (Figure 28). The starting raw material was hardwood lignosulfonate which mainly contains G and S-type lignin. Pre-oxidation was then executed as mentioned before, to help crosslink the units. At lower temperatures, dehydration and radical formation from α -o-4 and β -o-4 linkages occurred [112–114]. After, radicals started to cross-link with one another to form longer chains. When the temperature exceeded 270 °C, more C-O-C bonds started to break down, and long chains begin to crosslink [115].

Table 3. FTIR peak assignment



#	Assignment [106–109]	Wavenumber (cm ⁻¹)		
		Ligno- sulfonate	LCF [70]	LACF [70,110,111]
1	O–H stretching		3428	
2	C–H stretching in methyl groups		2937	
3	C–H stretching in methylene groups	2851	-	2851
4	C=O stretching in esters (carboxylic groups, aldehydes, ketones)	-	-	1731
5	C–O stretching & C=C Aromatic skeletal stretching	1610	1580	1626 (broad)
6	C=C Aromatic skeletal stretching (G, S rings)	1510	-	-
7	Aromatic skeletal vibration with asymmetric C-H deformation	1459	-	
8	C=C Aromatic skeletal stretching	1421	-	1421 (broad)
9	Phenolic O-H & aliphatic C-H in methyl groups	1374	1374	
10	Aromatic ring (G) breathing with C-O & C=O stretching	1210	-	-
11	C–O stretching/	-	1108	1040 (broad)
12	S–O in sulfonic groups	1040	-	(anhydride)
13		-	1000	
14	S–O in sulfonic groups		621	

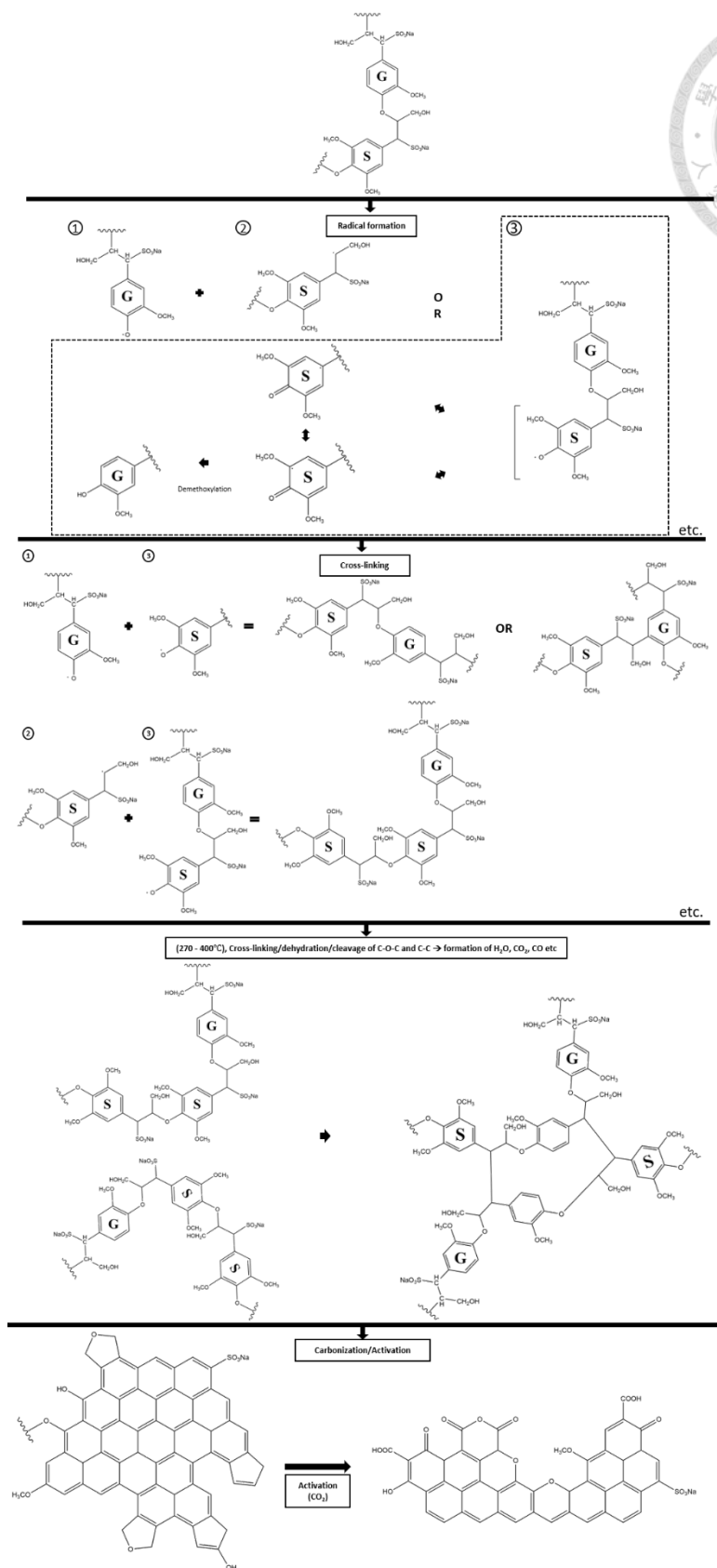
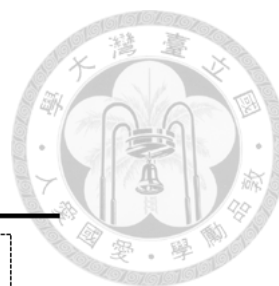


Figure 28. Scheme of Lignosulfonate transforming to LACF (modified from

[70,112,113])

The pre-oxidation temperature was 300 °C; therefore, the cross-linking from long chains into a larger network might only complete partially. More will be condensed during carbonization, which was implemented at higher than 400 °C. During carbonization, C-C bonds broke, and the radicals randomly repolymerized into polyaromatic forms [113]. As carbonization was executed under inert N₂ gas, and temperature increased up until 800 °C, many functional groups — except phenol and methoxyl groups, because of their stability under high temperature — were eliminated as presented in the FTIR result.

For activation, a series of reactions (Figure 29) happened to formulate the oxygen-containing groups [64]. According to the reactions, CO₂ acted as oxidation agent, not only reacting to carbon atoms, but also oxidized the hydroxyl groups to a higher oxidation state, such as carboxyl and anhydride groups. As a result, carbon monoxide and vacancies on the activated carbon were created [64].

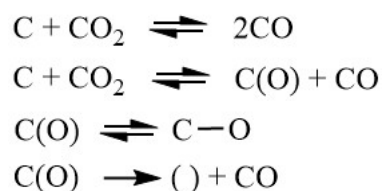


Figure 29. Reaction with CO₂ (() denotes a vacant site[64])

Comparing to other physical activation methods, such as H₂O, CO₂ is rather slow, but assist with the creation of micropores [64]. This also resulted in the better property for LACF that was activated for a longer time, including a higher micropore proportion and more surface functional groups. The former was verified in physical characterization sessions; the latter will be shown in the next surface functional group quantification analysis.



Elemental Analysis (Quantification)

Quantification-wise, Table 4 shows the result of elemental analysis, including carbon, hydrogen, oxygen, nitrogen, and sulfur contents. Overall, carbon content was more dominated within activated samples (LACF30 and LACF60) than non-activated samples. The reason is that, during activation process, the operating temperature was higher than that of carbonization, allowing the formation of more graphite-like structure. However, as activation time increases, carbon ratio declined while oxygen ratio climbed, leading to the decrease of C/O ratio. This can be attributed to the fact that more defective carbons participated in activation process, which will be verified in the following XPS C1s result.

The carbonization and activation process were both implemented under a nitrogen environment; thus, it was expected that nitrogen may be grafted onto the structure. Because activation temperature is higher than carbonization, more nitrogen component may react with the carbon structure, leading to a slight increase in the nitrogen percentage. In all samples, nitrogen occupied less than 1% of the structure.

In terms of sulfur content, it decreased in activated samples, but still retained around 3 %, corresponding with the existence of S—O peak in FTIR. Other than C, H, O, N, and S, there were still other components such as ashes and metal ions, whose proportion declined in LACFs because of the enhanced bond-breaking under longer and higher heat treatment.

Table 4. Elemental Analysis of LCF, LACF30 and LACF60

	C (%)	H (%)	O (%)	N (%)	S (%)	Other*(%)	C/O
LCF	60.63	2.31	22.78	0.50	6.37	7.40	2.66
LACF30	65.55	2.32	22.94	0.59	3.80	4.80	2.86
LACF60	63.35	2.46	24.51	0.67	3.23	5.78	2.58

*other components include ash and metal ions (eg. Na⁺), obtained through calculating 100-(C+H+O+N+S).

X-ray Photoelectron Spectroscopy (Quantification)

To further verify the ratio of different carbon structure, XPS analysis was implemented. Peak convolution result is shown in Figure 30 and the correspondent functional group identification is displayed in Table 5. Within all samples, peak 7 was hardly seen; thus here, the attention will be focused on peak 1-6. Peaks over 284 are aromatic signals, and those under 282 represent lack of crystallinity.

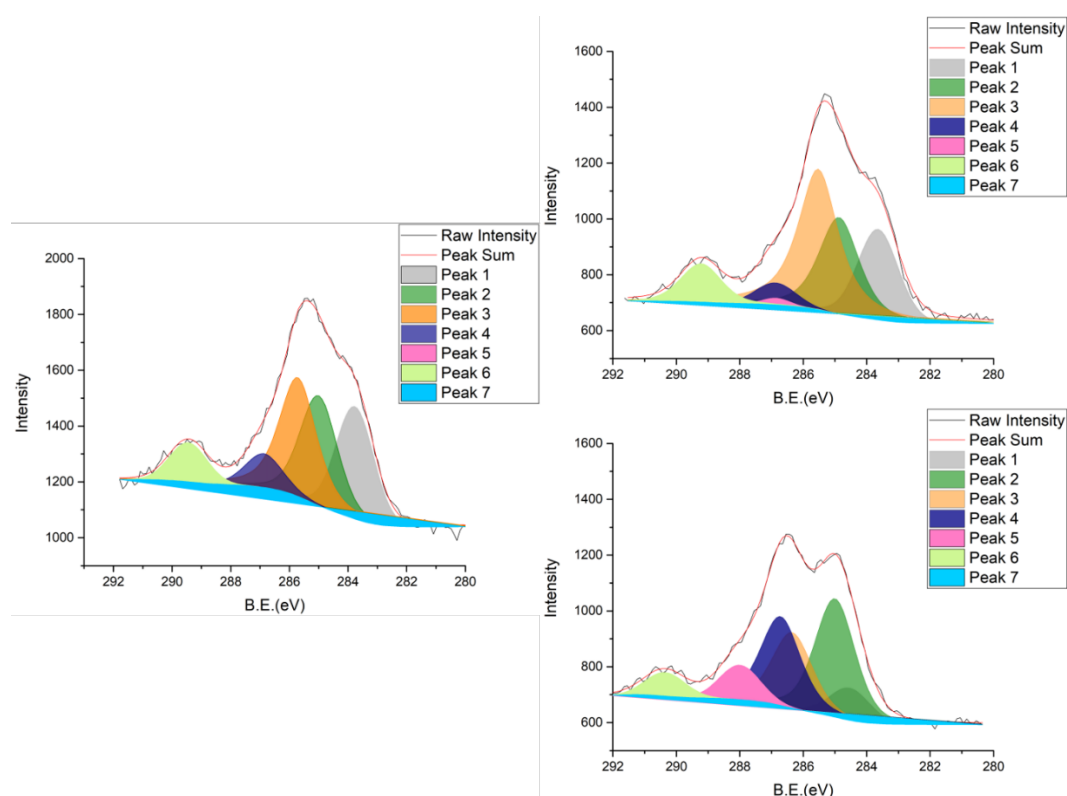
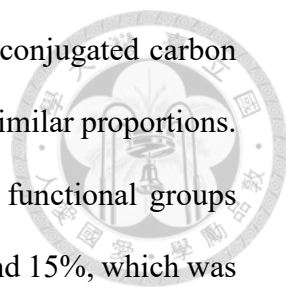


Figure 30. XPS C1s spectra. Left: CF; Right: above: LACF30; below: LACF60



LCF and LACF30 samples shared a similar trend, where non-conjugated carbon accounted for the largest ratio. Vacancy and conjugated carbon had similar proportions. For conjugated carbon, it may come from the graphene layers or functional groups (peak 4, 5, and 6), the combination of the latter accumulated to around 15%, which was below half of 40%. Thus, it is reasonable to conclude that more conjugated carbon comes from the graphene structure. Peak 4 and 6, respectively represents phenol, lactone, ether, and carboxy, lactone groups, both possessed similar low proportions within the structure. Peak 5, representing basic functional groups, quinone and pyrone, stands for 0% in CF and 2.93% in LACF30, suggesting that the amount of basic functional groups was quite few on the surface.

LACF60's conjugated carbon accounted for the largest ratio. From the increase ratio in peak 4 and 5, the LACF60 had more aromatic rings carrying oxygen-containing functional groups. While comparing between acidic functional groups, peak 4 and 6, phenol, lactone, and ether turned out to occupy more of the structure. One thing worth noticing is that, the ratio of basic functional groups also climbed. However, contrasting to acidic groups, basic groups were much fewer. Therefore, while considering for all basic features, LACF60 was still more acidic than LACF30 or CF. Overall, LACF60 contained more peaks over 284, implying that LACF60 contained more aromatic functional groups and can be a preferable adsorbent.

Table 5. XPS C1s LACF30 and LACF60 functional group ratio

Peak	Assignment	CF		LACF30		LACF60	
		(%)	Position	(%)	Position	(%)	Position
1	vacancy carbon	24.42	283.77	22.45	283.72	7.66	284.54
2	conjugated carbon	26.63	285.00	20.59	285	31.91	285
3	non-conjugated carbon	32.36	285.71	40.21	285.44	20.95	286.35
4	phenol, lactone, ether	8.11	286.87	6.06	286.62	25.43	286.72
5	quinone, pyrone	0.00	294.39	2.93	287.26	8.07	288.00
6	carboxyl, lactone	8.48	289.45	7.77	289.24	5.67	290.37
7	$\pi - \pi^*$	0.00	291.18	0.00	291.03	0.31	291.15

4.1.2.3 Graphene structure within LACF

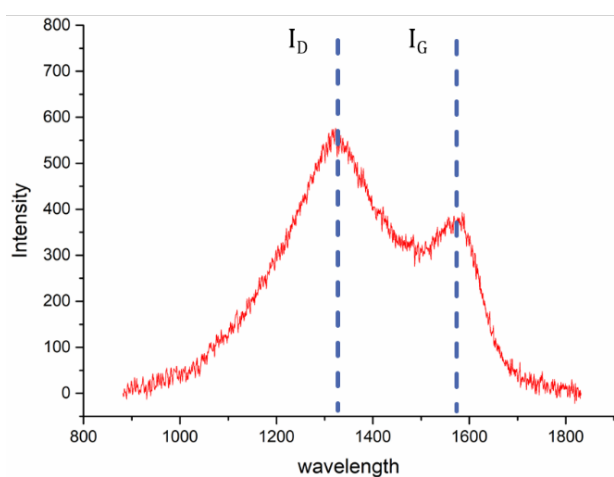


Figure 31. Raman Spectrum of LACF

According to the current and previous preliminary study [11], after high temperature carbonization, the main content of the material was carbon, which accounts for 50 % of the composition. The result matched with that of FTIR, that most of other

functional groups have been eliminated. Thus, in this study, carbon structure was further investigated.

From Figure 31, characteristic peaks for activated carbon fibers were shown respectively around 1374 cm^{-1} and 1580 cm^{-1} . The former represented for the amorphous graphite structure, while the latter stood for crystallized graphene structure. Regarding the calculation, I_D/I_G was around 1.53, indicating that the material was mainly composed of amorphous carbon structures. Nevertheless, the existence of the I_G peak verifies that part of the material consisted of graphene structures, meaning that π electrons exist. That is to say, electron rich regions were present on the surface, which would a helpful feature for adsorption performance.



4.1.3 Characterization of LACF with metal ion

To verify the existence of adsorbed metal ions, EDS was implemented. Further, as a supplementary for exploring adsorption mechanism, LACF-M was evaluated through FTIR.

4.1.3.1 Energy dispersive spectroscopy (EDS)

Original LACF, and LACF-M were all examined under EDS. The results along with the SEM photos were shown in Figure 32, Figure 33, and Figure 34. Figure 32 exhibited the original LACF. From the selected region, it is again certified that after carbonization and activation, sodium and sulfur still existed on the LACF surface. Furthermore, calcium ion was also present.

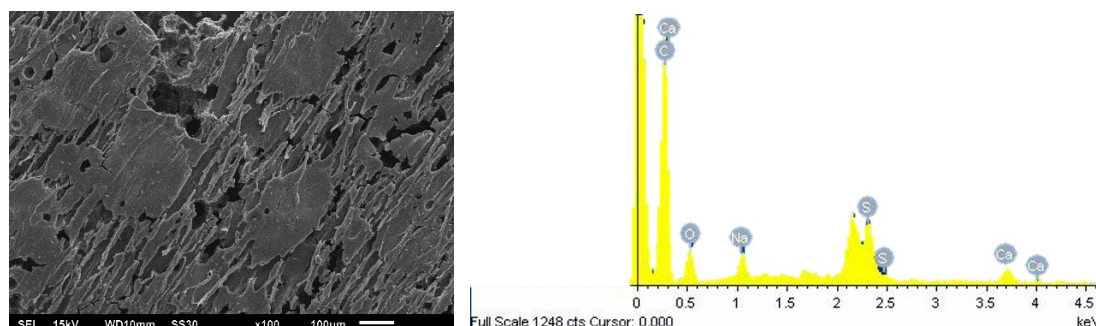


Figure 32. EDS for LACF. Left: examined area; right: element detection

The result of LACF-Cu was shown in Figure 33. Before being examined under EDS, observing from the surface of the sample, there was no clear difference between LACF and LACF-Cu, both appear to be black activated carbon fiber. Only when sent under EDS, could the adsorption of Cu(II) be verified. The signal of Cu and Na occurs at a similar position. Therefore, in LACF-Cu, as Cu's intensity was much stronger, it masked Na's signal.

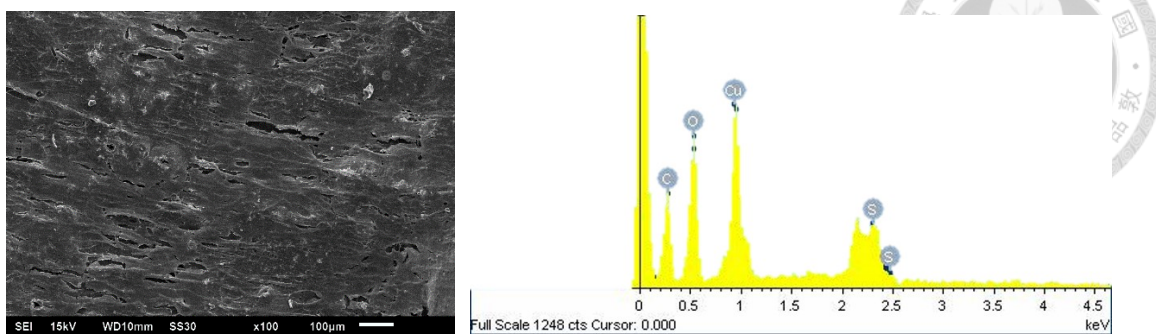


Figure 33. EDS for LACF-Cu. Left: examined area; right: element detection

EDS results for LACF-Au was presented in Figure 34. The adsorption of Au(III) can be clearly seen even without EDS. The whole piece of LACF was observed yellow, indicating the reduction of gold. Under EDS, from the selected region, except for Au, only oxygen and an impurity Br element were examined.

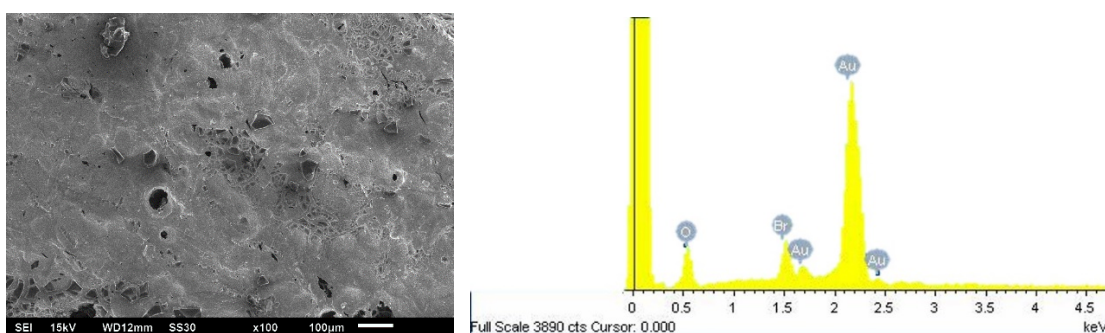


Figure 34. EDS for LACF-Au. Left: examined area; right: element detection

4.1.3.2 Fourier transform infrared (FTIR) spectroscopy

Original LACF sample, LACF-Cu, LACF-Au, LACF-Cu des (the sample that Cu(II) got desorbed), and LACF-Au des (the sample that Au(III) got desorbed) were all examined (Figure 35) to investigate the possible adsorption mechanism.

For Au(III) adsorption, a new peak at 1567 cm^{-1} appeared, peak at 1237 became a broader band, and the one at 1099 shifted. The newly raised peak at 1567 cm^{-1} can be resulted from asymmetric stretching of different carboxylate groups, showing that

carboxylic acid groups were deprotonated by Au(III) during the adsorption process[96]. Changes at 1237 and 1099 indicated that the form of C-O bond was altered, which can be attributed to the C-O-Au bond. A slightly shift and peak intensity change was observed around 620 cm^{-1} , indicating that the sulfonate groups may participate in adsorption through forming complexes with Au ions.

From LACF-Cu curve, the main change happened in 1237 and 1099 cm^{-1} . It went in a different direction than LACF-Au, here, the peak decreased, also indicating that the C-O bond may be used during Cu(II) adsorption. The change around 620 cm^{-1} was observed, implying that sulfonate groups may have formed complexes with Cu ions as well. Other peaks overall remained the same. Comparing LACF-Au and LACF-Cu, more changes happen in the former one, implying that Au(III) adsorption might involve more oxygen-containing functional groups.

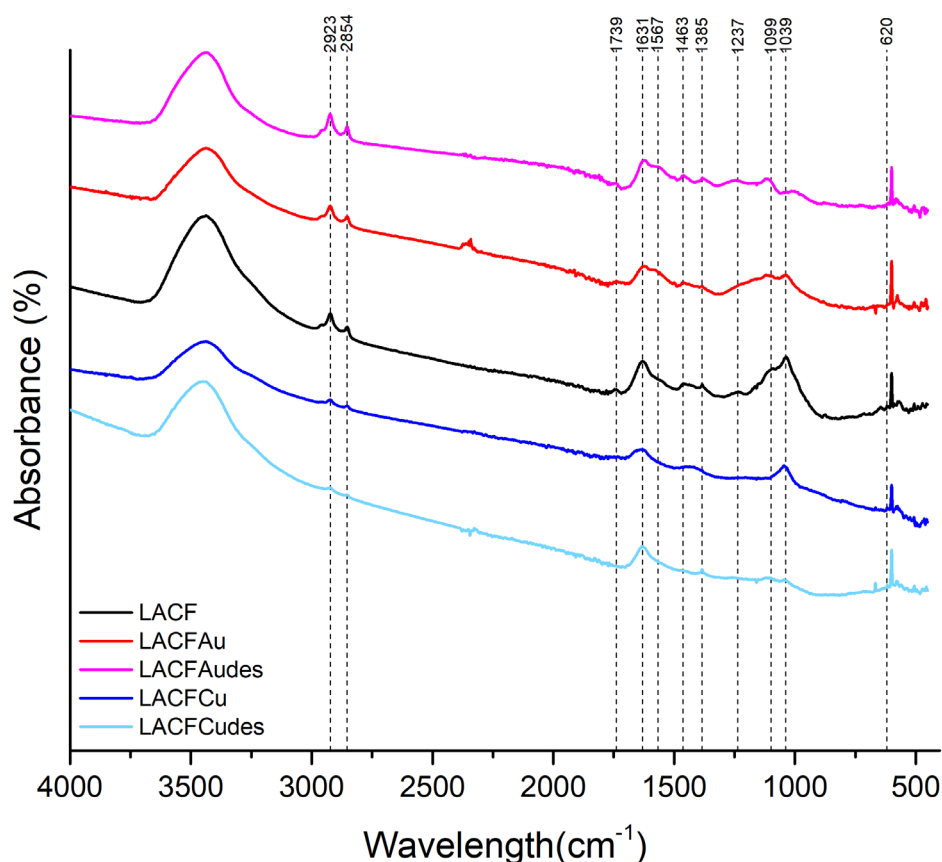


Figure 35. FTIR for LACF – before, after adsorption, and after desorption

The desorption curves show that, the LACF was successfully recovered. LACFAudes and LACFCudes both have similar positions as LACF. The underlying desorption mechanism may be ion exchange. The desorption agent exchanged its hydrogen with the metal ions to recover the surface functional groups, allowing LACF to adsorb again in the next cycle. However, comparing the recover efficiency, LACFAudes still contained the peak in LACFAu, indicating part of the functional groups were not recovered, and there might be Au ions remained bonded, which can explain for the rather unideal re-adsorption efficiency shown in the later session.

4.2 Batch Adsorption experiment

4.2.1 Cu(II)/Au(III) adsorption according to various pH

From previous zeta potential test (by various pH), it was shown that the solution environment will greatly affect the surface charge of LACF. As one of the possible adsorption mechanisms is through coulomb electrostatic force, in this session, adsorption performance by various initial pH environment will be examined. The optimized pH would be applied to isotherm, kinetic and adsorption-desorption cycle test.

Figure 36 and Figure 37 respectively showed Cu(II) and Au(III) adsorption as a function of solution pH.

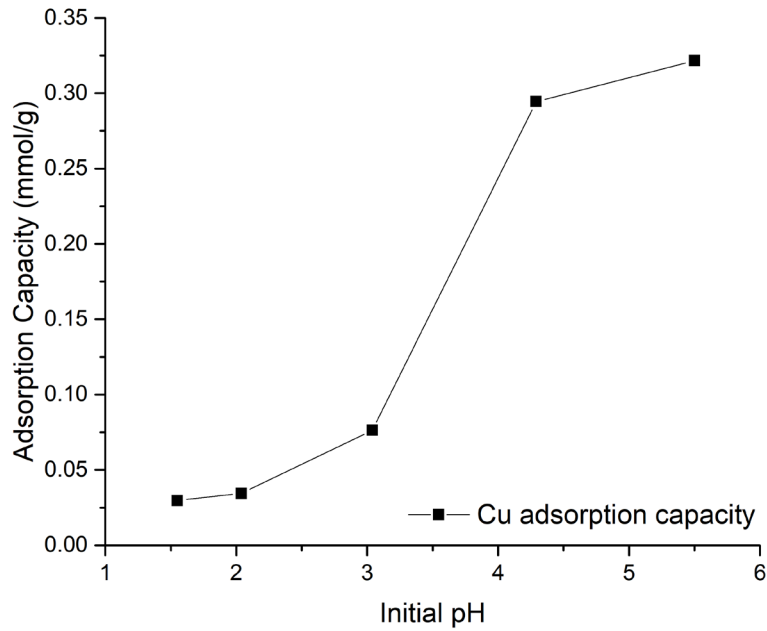


Figure 36. Effect of pH solution on Cu(II) adsorption

According to Figure 36, Cu(II) adsorption was greatly affected by the solution environment, and the trend can be mapped to the zeta potential test results. Recall that the LACF's point of zero charge occurred at around 3.5, below this point, the surface mainly carried positive charge; after the point, the surface was covered with large amount of negative charge. Cu(II) adsorption efficiency tripled after the point of zero charge, implying that one of the adsorption mechanisms for copper metal ions was through electrostatic force. As negative surface charge increased, more positive Cu(II) ions were attracted to the LACF.

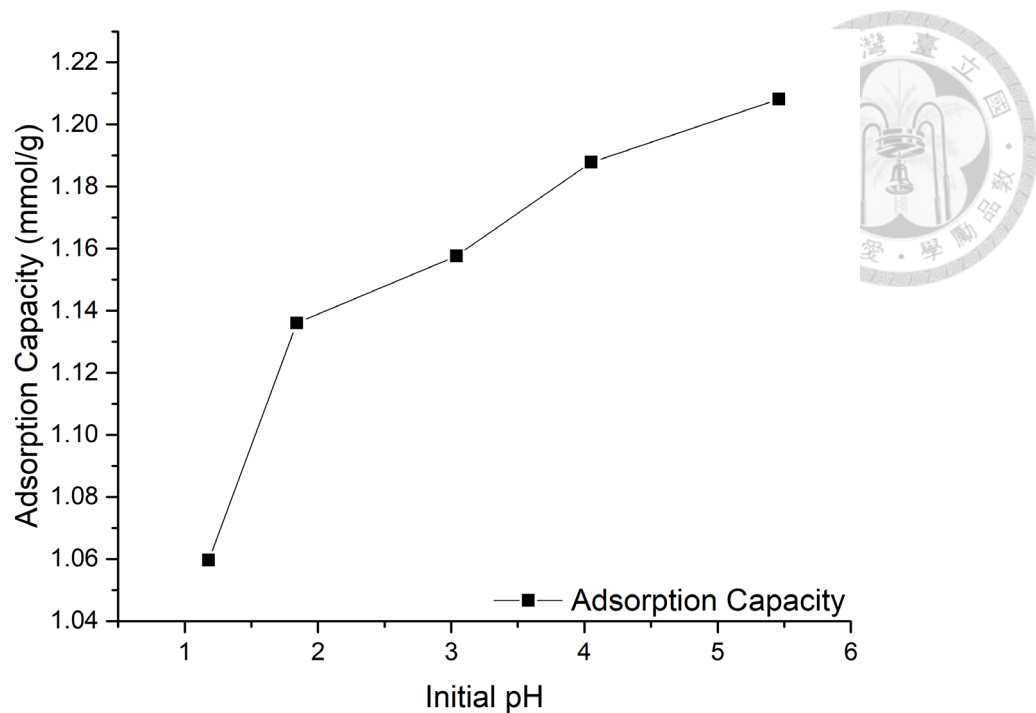


Figure 37. Effect of pH solution on Au(III) adsorption

Similar to Cu(II) adsorption, Au adsorption capacity increased with the pH, but the range was narrower. In solution, Au(III) mainly existed as AuCl_4^- ; therefore, it is reasonable that in acidic environment, when activated carbon carried positive charges, it still displayed good adsorption performance. When pH climbs, the hydrogens on oxygen-containing functional groups were mostly affected, which contributed to the charge change on the surface. However, Au(III) adsorption did not vary that much with the trend, the reason can be that, one of the underlying adsorption mechanisms for gold was through pi electrons on the graphene surface. The ions directly interact with the electrons and reduced to Au(s) on the LACF. As a result, LACF-Au is observably yellow from the moment LACF starts to adsorb.

4.2.2 Cu(II)/Au(III) adsorption according to various concentration (Isotherm)

Models used here are Langmuir, Freundlich and Redlich-Peterson. From the mathematical models shown in materials and methods session, the R-P model will

reduce to Freundlich model when the concentration is high; reduce to Langmuir model when $\beta = 1$ [96]. Thus, the relationship between R-P and Freundlich models, R-P and Langmuir models are called nested models. The relationship between Freundlich and Langmuir models is called non-nested [116].

To evaluate the model fitting result, quality control (residual analysis) and model parameters were examined. Further, to compare among these three models and select one that is most likely to account for the dataset, corrected Akaike's Information Criteria (AICc) was used because it is suitable for both nested and non-nested situations.

For each metal isotherm dataset, two versions of modeling were done, one included all data point (abbreviated as "original"), and the other excluded points that were out-of-trend (abbreviated as "excluded"). Evaluate the quality control results from both datasets; then, for further adsorption energy calculation, choose the dataset that resulted in a better fitting result.

4.2.2.1 Cu(II) isotherm modeling

Figure 38 shows the plot of the isotherm test with the fitted curves. After performing the non-linear regression, residual analysis was done for quality control. Overall, the fitting results from the excluded dataset were better. Next, the estimated parameters will be evaluated.

Estimated parameters from fitted models are presented in Table 6. For both datasets, parameters predicted from Langmuir and Freundlich were significantly larger than 0, meaning that these parameters will have impacts on predicting equilibrium adsorption capacity, given the metal ion equilibrium concentration in the solution. On the other hand, the fitting result from Redlich-Peterson model showed wide standard errors for K_r and a_r in both datasets. Because the range that the true parameter might fall in was rather wide, it increased the uncertainty for parameter estimation, indicating that

Redlich-Peterson might not be a proper model to explain this Cu(II) isotherm data. To select the best model, in the next session, the result from corrected Akaike's Information Criteria (AICc) will be examined.

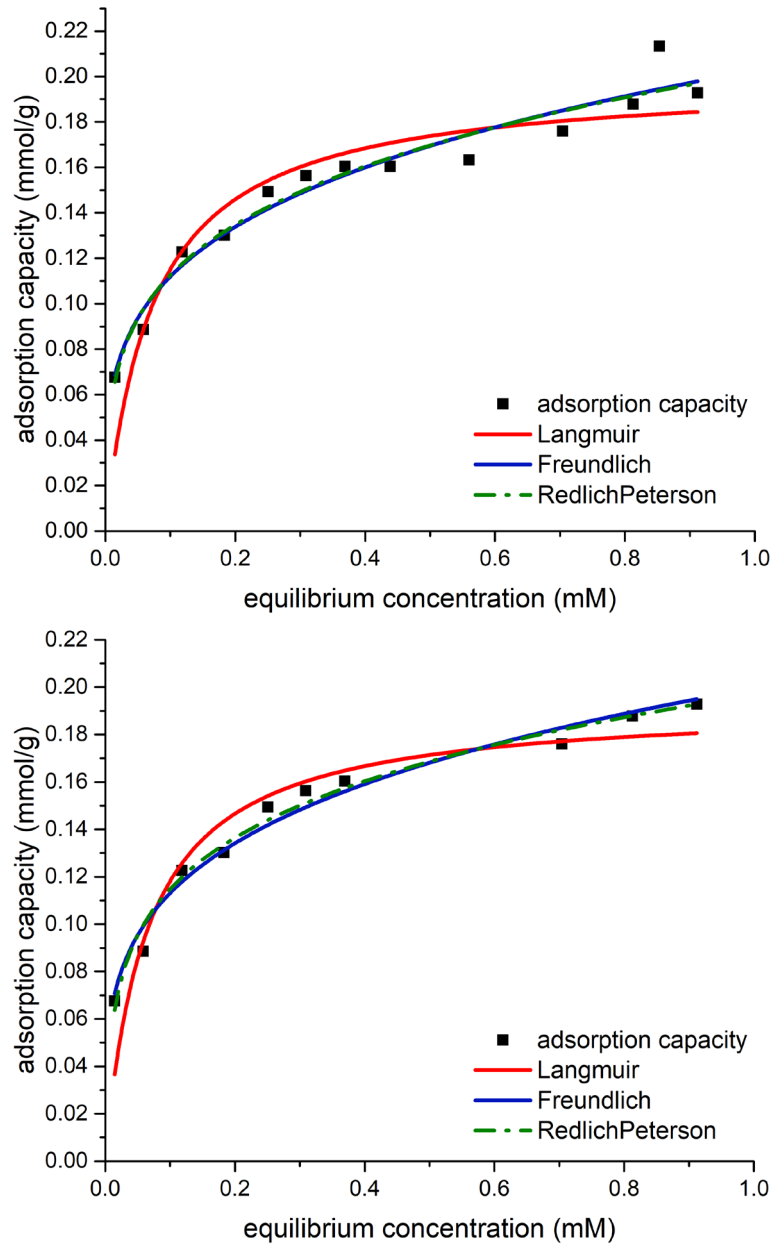
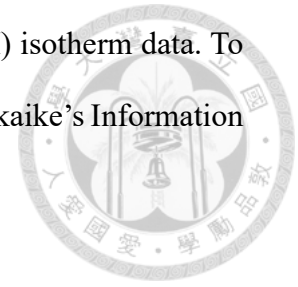


Figure 38. Batch isotherm test: Cu-original(above); Cu-excluded(below)

Table 6. Cu(II) adsorption isotherm modeling result

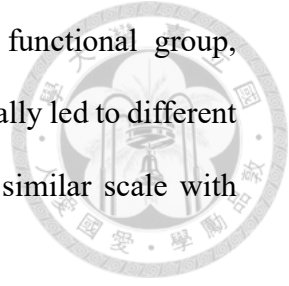
Isotherm model	Parameters	Cu ²⁺	Cu ²⁺ (excluded)
Langmuir	Q _{max} (mmol/g)	0.189 (0.010) *	0.184(0.011) *
	b(L/mmol)	18.698(4.747) *	20.875(5.550) *
	Residual standard error	0.046	0.045
Freundlich	K _f	0.203(0.004) *	0.201(0.004) *
	n	3.838(0.235) *	3.925(0.215) *
	Residual standard error	0.022	0.018
Redlich-Peterson	K _r	63.897(168.601)	29.900(29.120)
	a _r	316.093(832.311)	149.844(145.018)
	β	0.751(0.036) *	0.772(0.030) *
	Residual standard error	0.022	0.018

Note: ¹numbers in parenthesis are standard error.²star mark (*) means the parameter is significantly larger than 0

The reason of using AICc instead of the original AIC is that the sample size (n) used in this study was only around 10, comparing with the parameters being estimated (p), n is not much larger. The difference of AICc between models is more meaningful than the number itself. It represents the likelihood of one model being more correct than another. To be more specific, a difference of 6 corresponds to a 95% chance that the model with the lower score is correct.

Table 7 shows the AICc calculation result from all fitted models. In terms of model selection, Freundlich model had the lowest AICc score for both datasets, indicating that Cu(II) adsorption on LACF was best described by the Freundlich isotherm model. According to previous material characterization, possible factors that might contribute to this heterogeneous adsorption behavior were various surface functional groups and ununiform pore size distribution. Both led to different adsorption attraction for

adsorbates, the former consisted of different oxygen-containing functional group, creating diverse attraction forces to adsorbates, while the latter naturally led to different affinity for adsorbates because not every pore diameter was in a similar scale with Cu(II).



However, it is also worth noticing that, although the Langmuir model was not the best one for describing Cu(II) ion, its model fitting result passed the quality control test. Thus, Langmuir model can still be used to calculate the free-energy [96].

Table 7. AICc calculation for each model fitting result (Cu²⁺)

Model	Cu ²⁺	Cu ²⁺ (excluded)
Langmuir	-333.359	-201.636
Freundlich	-358.605	-223.228
Redlich-Peterson	-354.768	-218.688

4.2.2.2 Au(III) isotherm modeling

Figure 39 shows the plot of the isotherm test with the fitted curves. After performing the non-linear regression, residual analysis was done for quality control. Overall, the fitting results from the original dataset had better quality. Next, the estimated parameters will be evaluated.

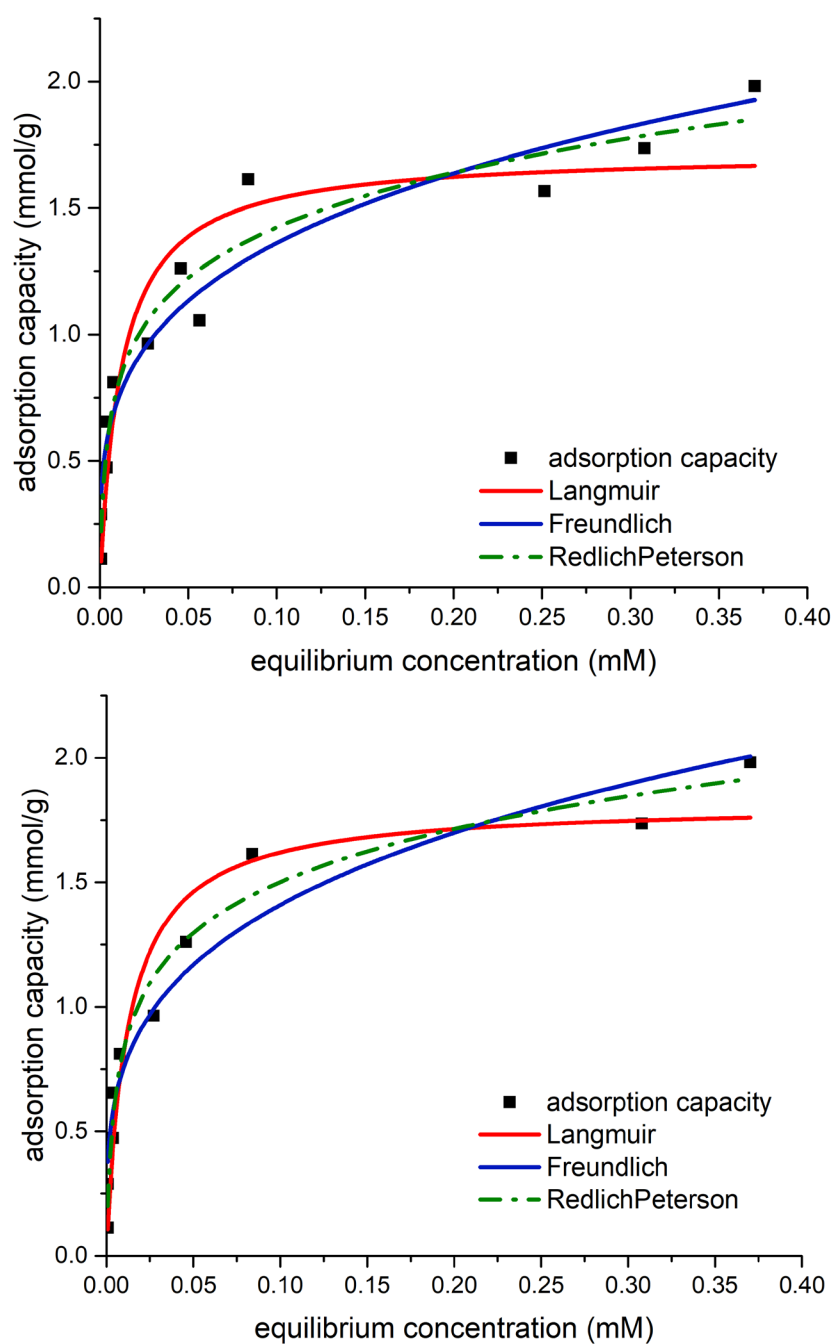


Figure 39. Batch isotherm test: Au-original(above); Au-excluded(below)

Estimated parameters from fitted models were presented in Table 8. For both datasets, parameters predicted from all models were significantly larger than 0, meaning that these parameters had impacts on predicting equilibrium adsorption capacity, given the metal ion equilibrium concentration in the solution. However, the fitted parameters from the Redlich-Peterson exhibited a rather wide standard error, which increased the

uncertainty of parameter estimation. The result indicated that Redlich-Peterson model might not be suitable for explaining the Au(III) isotherm data. To select the most appropriate model, in the next paragraph, the result from corrected Akaike's Information Criteria (AICc) will be evaluated.

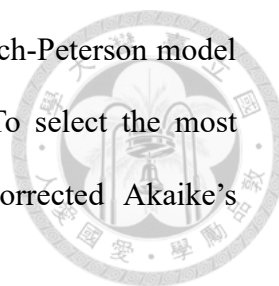


Table 8. Au isotherm modeling result (calculate from R)

Isotherm model	Parameters	Au ³⁺	Au ³⁺ (excluded)
Langmuir	Q _{max} (mmol/g)	1.595 (0.126) *	1.704 (0.148) *
	b(L/mmol)	117.784 (32.554) *	107.794 (28.369) *
	Residual standard error	0.207	0.195
Freundlich	K _f	2.812 (0.329) *	2.972 (0.413) *
	n	3.043 (0.341) *	2.969 (0.358) *
	Residual standard error	0.235	0.252
Redlich-Peterson	K _r	310.465 (116.410) *	283.664 (95.956) *
	a _r	143.699 (47.499)*	126.925 (37.784) *
	β	0.840 (0.062) *	0.853 (0.064) *
	Residual standard error	0.167	0.159

Note: ¹numbers in parenthesis are standard error.²star mark (*) means the parameter is significantly larger than 0

Table 9 shows the AICc calculation result from all fitted models. For both datasets, the Langmuir model was the lowest among comparison. Therefore, it indicated that Au(III) adsorption on LACF was best explained by Langmuir model. Although, from previous chemical characterization, it is shown that the surface of the LACF contains functional groups, so the true relationship might not be exactly Langmuir-like (i.e. homogeneous adsorption sites on the material).

One possible reason that the Langmuir model described better was because Au(III) adsorption depended largely on π electrons, which existed everywhere on the surface. Comparing to binding with functional groups, if most Au(III) ions tend to reduce to Au through exchanging electrons, it was possible that the surface looked rather homogeneous for Au(III) ions. The fitting result also served as an index, showing that it is reasonable to use the Langmuir model to estimate for parameters and calculate adsorption free energy.

Table 9. AICc calculation for each model fitting result (Au^{3+})

Model	Au^{3+}	Au^{3+} (excluded)
Langmuir	-21.20223	-20.45618
Freundlich	-5.903896	-6.367689
Redlich-Peterson	-15.55302	-14.459

4.2.2.3 Calculation for Free-energy of adsorption of the system

For copper adsorption system, Langmuir model fitting results from w/o out-of-trend data was used for free-energy calculation, because this dataset performed better at goodness-of-fit.

For gold adsorption system, because original and w/o out-of-trend dataset performed similar at goodness-of-fit. Langmuir model fitting results from the original isotherm data was used for free-energy calculation.

Table 10 showed the necessary parameters and calculation results. The equilibrium concentration used in both cases were the first data point after the bending of the curves. According to Liu, for a dilute solution consists of charged adsorbate, it is valid to use Langmuir equilibrium constant to calculate free-energy if the constant is corrected with activity coefficient (γ_e) [117]. Calculation showed that copper adsorption system's free-

energy was -26.94kJ/mol, which lied between physisorption and chemisorption, and was closer to physisorption. Gold adsorption system's free-energy was -33.23kJ/mol, which also lied between physisorption and chemisorption. Comparing to copper adsorption, gold adsorption might be composed of more chemisorption.

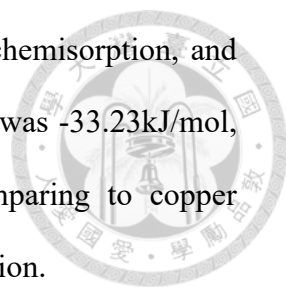


Table 10. Free-energy calculation for Cu(II) and Au(III)

Parameters	Cu^{2+} (excluded)	Au^{3+} (original)
Metal ion concentration(mM)	0.369	0.08387
Temperature(K)		303
ϵ (water @ 303K)		76.546
Metal ion charge	+2	+3
α (ion size, pm)	600	900
(cannot find Au's, instead refer to other 3+ ion's)		
Buffer solution	0.05M CH_3COOH/CH_3COONa	0.0584M HCl/KCl
pH	5.4	1.79
I_e (mol/L)	0.051476	0.0589
γ_e	0.474	0.220
b (L/mol)	20,875	117,784
$K_a = b/\gamma_e$	44,040	53,5382
$\Delta_{ads}G^0 = -RT\ln K_a$ (kJ/mol)	-26.94	-33.23

The adsorbate pH and concentration for kinetics test were determined by the above pH and isotherm analysis results. The optimal pH environment for Cu(II) adsorption was between pH = 5-6, but according to calculation, $Cu_{(s)}$ precipitates at around pH = 5.5. Thus, pH = 5.4 was chosen for the following kinetics test. Au(III) performed similarly well among tested pH environment. Out of convenience consideration, the pH=2.17 was chosen as it was close to the pH value of Au(III) stock solution.

As described in ASTM, solution concentration should be adjusted such that 10—85% of adsorbate removal can be achieved for kinetics analysis. To compare the adsorption capacity of different adsorbates, Cu(II) concentration was first determined;

then Au(III) concentration followed. According to the Cu(II) isotherm test, the knee point of the plateau curve was when the initial adsorbate concentration was 0.42 mM, and the adsorption percentage was around 15%, satisfying ASTM regulation. Thus, both Cu(II) and Au(III) concentration were fixed to 0.42 mM in the following session.

4.2.3 Cu(II)/Au(III) adsorption according to various contact time (Kinetics)

To analyze the adsorption kinetic test, pseudo-first- and pseudo-second-order models were used for fitting. As kinetic data is a type of time series data, to estimate the quality of fitted kinetic models, “standardized residuals v.s. fitted values” plot, “normal Q-Q” plots, and normality tests were used. Overall, the error distribution did not show severe heteroskedasticity problem and distributed normally. Thus, both first-order and second-order models passed the quality control test. In the next session, the estimated parameters will be examined.

Estimated parameters from fitted kinetic models were presented in Table 11. All parameters appeared to be significant, indicating that given an adsorption duration (t), these parameters will influence the predicted equilibrium adsorption capacity. To choose a model that can better explain the data, in the next paragraph, corrected AIC test will be performed.

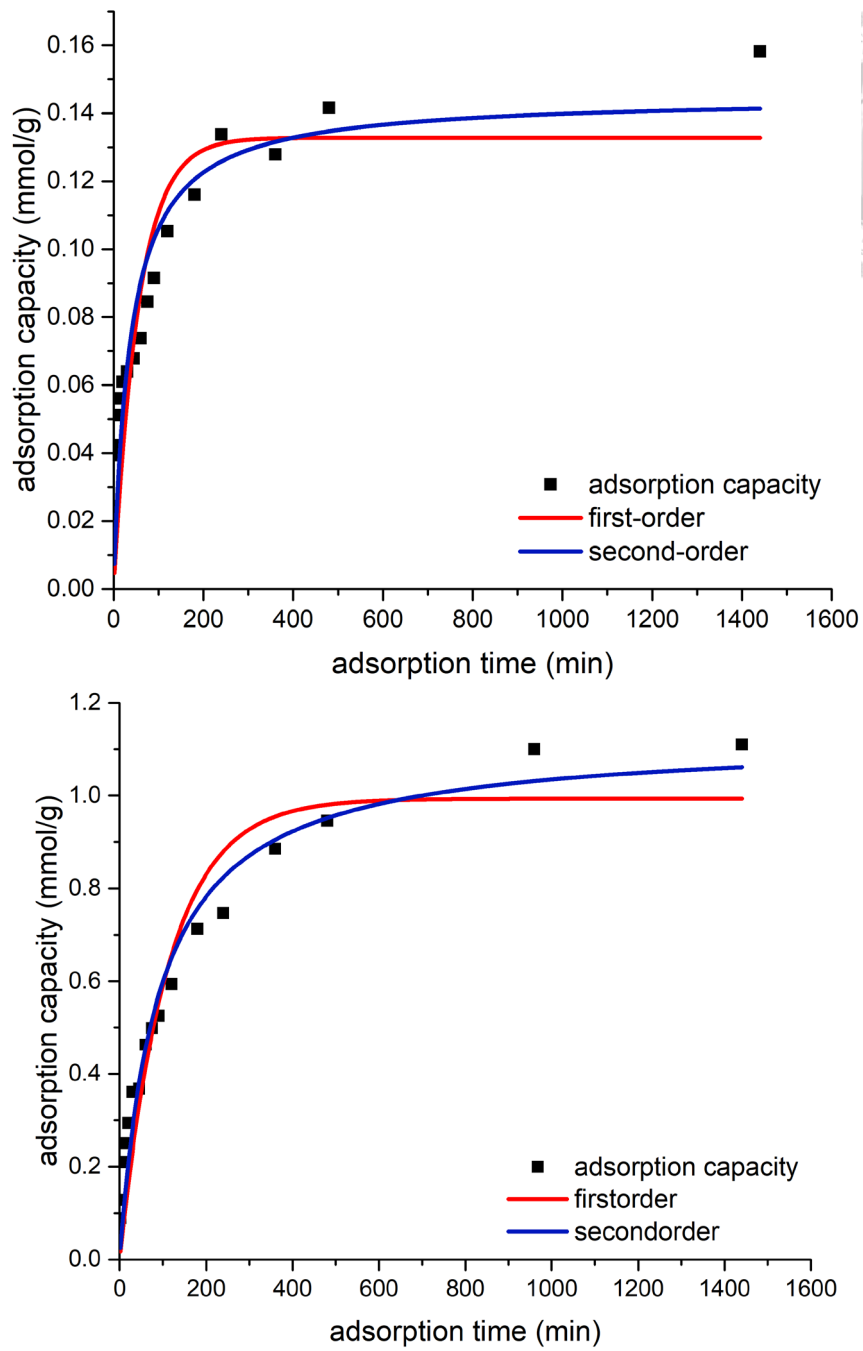


Figure 40. Batch kinetics test: Cu(II)(above); Au(III)(below)

Table 11. Estimated parameters from kinetic models

Kinetic model		Cu ²⁺	Au ³⁺
First-order	q _e	0.117 (0.012) *	0.906 (0.070) *
	k	0.030 (0.009) *	0.013 (0.002) *
Second-order	q _e	0.128 (0.011) *	1.029 (0.065) *
	k ₂	0.354 (0.134) *	0.015 (0.003) *

Note: ¹numbers in parenthesis are standard error. ²star mark (*) means the parameter is significantly larger than 0

Table 12. AICc calculation for each model fitting result

Model	Cu ²⁺	Au ³⁺
First-order	-626.4292	-221.0134
Second-order	-633.9946	-230.3926

As model with a lower AICc has a higher chance to correctly account for the dataset, for both Cu(II) and Au(III) adsorption, second-order kinetic model was preferred. Pseudo-second-order model assumes that chemical adsorption may involve in the rate-limiting step. One possible mechanism can be valency-force dependent, for which adsorbate and adsorbents interacted through electron exchange.

To sum up, according to isotherm and kinetic tests, the main mechanism for Cu(II) and Au(III) adsorption should consist of both physisorption and chemisorption, while the former had a larger impact.

4.3 Desorption and Recycle of LACFs

For Cu(II) and Au(III) metal ions, 3 cycles of adsorption-desorption were done, and the results were shown in Figure 41 and Figure 42.

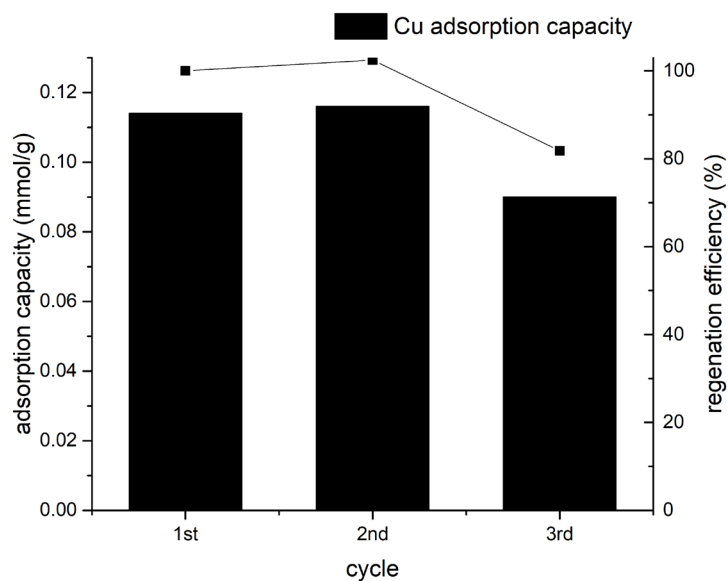


Figure 41. 3-cycle Cu(II) adsorption-desorption

In Cu(II) adsorption, the adsorption efficiency remained unchanged until the second cycle, and decreased to around 80% in the 3rd cycle. The rather stable adsorption performance resulted from the adsorption mechanism. As calculated before, Cu(II) adsorption largely involved physisorption, meaning that it was more easily to desorb. While the LACF was recovered more completely, it could retain the same adsorption capability as before.

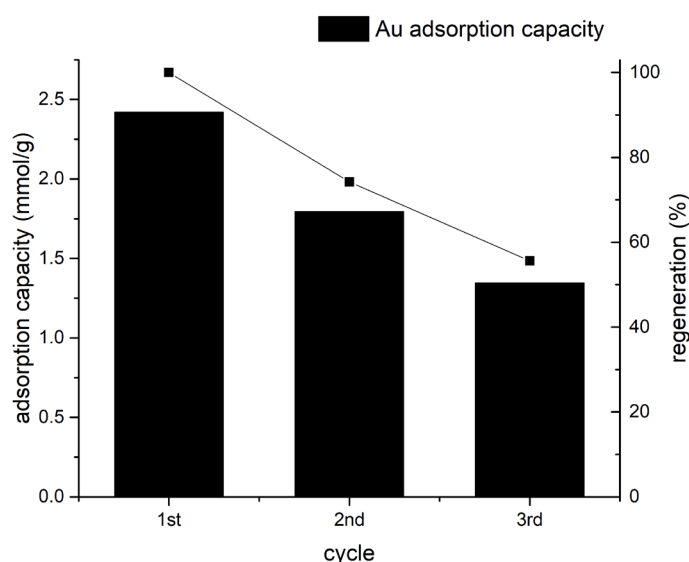
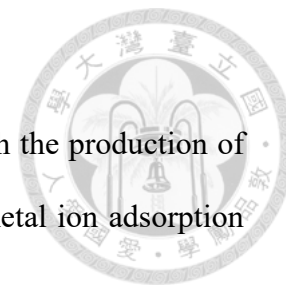


Figure 42. 3-cycle Au (III) adsorption-desorption

Au(III) recover on the other hand, the adsorption capacity gradually decreased with the cycle number, and the regeneration rate was 50% at the 3rd cycle. At the macroscope, after desorption, part of the LACF retained the yellow color, along with the FTIR result, implying that Au(III) desorption was not done completely, a stronger desorption agent was needed for a better desorption result. Furthermore, this as well verified that, Au ions had stronger bonds with LACF, indicating that more chemisorption involved.

Chapter 5: Conclusions and Recommendations

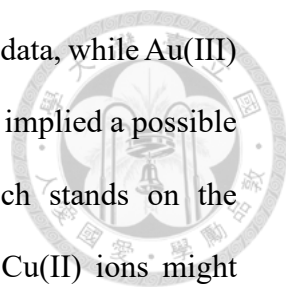


The study mainly focuses on two parts, the first part deal with the production of lignosulfonate activated carbon fiber, and the second part is the metal ion adsorption behavior study.

Result showed that LACF30 and LACF60 were found to have superior physical properties than CF, indicating that physical activation successfully introduced desired pore structures. From the chemical characterization result, LACF60 stood out, because it was composed of significantly more acidic functional groups, including phenolic, carboxylic, and anhydride. Although comparing to LACF30, it had a higher weight loss, when it comes to adsorption application, surface function was more important. The acidic groups provide activation site for metal ions to bind to, along with the help of porous structure. Hence, LACF60 was chosen as the optimal sample to implement the second metal ion adsorption experiment.

Batch adsorption experiment was used to evaluate the metal ion adsorption mechanism on LACF60. Adsorption capacity change according to various pH was implemented first to determine the better pH environment for adsorption. The result showed that, for copper metal ion, as pH climbed the adsorption capacity increased as well. However, when initial pH was larger than 5.4, Cu(II) would precipitate. Thus, the optimized adsorption environment for copper metal ions was set to pH = 5.4. On the other hand, Au(III) adsorption was not influenced by pH as much, from this experiment, the most suitable pH environment was around pH = 2.0. As pH changed, zeta potential varied. Due to the fact that Cu(II) was more sensitive to this pH change, the adsorption mechanism may involve electrostatic force.

Isotherm and kinetic modeling respectively offered a quantitative way to calculate the adsorption energy and observe the determinative reaction step. For Cu(II)



adsorption, Freundlich model could account for more variance in the data, while Au(III) adsorption was better described by Langmuir model. The result also implied a possible different adsorption mechanism for each of them. As Freundlich stands on the assumption that adsorption happens on a heterogeneous surface, Cu(II) ions might depend more on the physical adsorption through affinity between pores and ions. While the pores were not uniform, it may contribute to the heterogeneous adsorption behavior. Langmuir model stands on the assumption that adsorption is homogeneous. Among LACF, the crystalized graphite structure is where the homogeneous adsorption might occur. If Au(III) was mainly adsorbed on the area, it may rely on the pi electrons on the basal panel, precipitating to the solid form as soon as being adsorbed.

The kinetic result provided evidence that Cu(II) and Au(III) adsorption were both a mix of physisorption and chemisorption, with the former being closer to pure-physisorption. Another evidence for supporting the result was the FTIR spectra on metal-ion adsorbed samples. Peaks regarding carboxylic groups were altered, indicating that it may involve in the adsorption process through ion exchange or complexation mechanism. To sum up, possible mechanisms for Cu(II) adsorption include van der Waals force, electrostatic force, and ion exchange, while Au(III) adsorption involved microprecipitation, and ion exchange mechanism.

Finally, LACF was also tested for regeneration. The result implies that, after 3 cycles of adsorption-desorption, no matter for Cu(II) or Au(III) adsorption, LACF was still functional. However, as Au(III) adsorption was more difficult to desorb, stronger recover reagent is needed for a more efficient recovery. All in all, lignosulfonate activated carbon fiber was useful for recovering valuable metal ions. Production-wise, it naturally consists of sulfur elements that are beneficial to adsorption; function-wise,

comparing to traditional granular form, the fiber form is more convenient for recycling,
and adsorb compatibly effective.




References

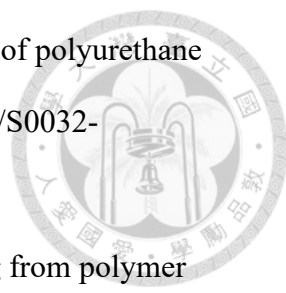
1. Myglovets, M.; Poddubnaya, O. I.; Sevastyanova, O.; Lindström, M. E.; Gawdzik, B.; Sobiesiak, M.; Tsyba, M. M.; Sapsay, V. I.; Klymchuk, D. O.; Puziy, A. M. Preparation of carbon adsorbents from lignosulfonate by phosphoric acid activation for the adsorption of metal ions. *Carbon N. Y.* **2014**, *80*, 771–783, DOI:10.1016/j.carbon.2014.09.032.
2. Suhas; Carrott, P. J. M.; Ribeiro Carrott, M. M. L. Lignin – from natural adsorbent to activated carbon: A review. *Bioresour. Technol.* **2007**, *98*, 2301–2312, DOI:10.1016/j.biortech.2006.08.008.
3. Li, T.; Takkellapati, S. The current and emerging sources of technical lignins and their applications. *Biofuels, Bioprod. Biorefining* **2018**, *12*, 756–787, DOI:10.1002/bbb.1913.
4. Chen, Y.; Zi, F.; Hu, X.; Yu, H.; Nie, Y.; Yang, P.; Cheng, H.; Wang, Q.; Qin, X.; Chen, S.; Zhang, Y. Grafting of organic sulfur-containing functional groups on activated carbon for gold(I) adsorption from thiosulfate solution. *Hydrometallurgy* **2019**, DOI:10.1016/j.hydromet.2019.02.007.
5. Yang, X.; Wan, Y.; Zheng, Y.; He, F.; Yu, Z.; Huang, J.; Wang, H.; Ok, Y. S.; Jiang, Y.; Gao, B. Surface functional groups of carbon-based adsorbents and their roles in the removal of heavy metals from aqueous solutions: A critical review. *Chem. Eng. J.* 2019.
6. Hsu, E.; Barmak, K.; West, A. C.; Park, A.-H. A. Advancements in the treatment and processing of electronic waste with sustainability: a review of metal extraction and recovery technologies. *Green Chem.* **2019**, *21*, 919–936, DOI:10.1039/C8GC03688H.
7. UNEP; PACE; ITU; ILO; UNIDO; UNU; Unitar; WBSCD; WEF *A New*


- Circular Vision for Electronics Time for a Global Reboot*; Geneva, 2019;
8. Lee, T.; Ooi, C. H.; Othman, R.; Yeoh, F. Y. Activated carbon fiber - The hybrid of carbon fiber and activated carbon. *Rev. Adv. Mater. Sci.* **2014**.
 9. Suzuki, M. Activated carbon fiber: Fundamentals and applications. *Carbon N. Y.* **1994**, *32*, 577–586, DOI:10.1016/0008-6223(94)90075-2.
 10. Chang, F.-C.; Yen, S.-H.; Wang, S.-H. Developing Lignosulfonate-Based Activated Carbon Fibers. *Materials (Basel)*. **2018**, *11*, 1877–1888, DOI:10.3390/ma11101877.
 11. Yen, S.-H.; Chang, F.-C. Effects of Fiber Processing Conditions on the Yield, Carbon Content, and Diameter of Lignosulfonate-based Carbon Fibers. *BioResources* **2016**, *11*, 10158–10172, DOI:10.15376/biores.11.4.10158-10172.
 12. Vergunst, T.; Kapteijn, F.; Moulijn, J. A. Carbon coating of ceramic monolithic substrates. In *Studies in Surface Science and Catalysis*; Delmon, B., Jacobs, P. A., Maggi, R., Martens, J. A., Grange, P., Poncelet, G. B. T.-S. in S. S. and C., Eds.; Elsevier, 1998; Vol. 118, pp. 175–183 ISBN 0167-2991.
 13. Aro, T.; Fatehi, P. Production and Application of Lignosulfonates and Sulfonated Lignin. *ChemSusChem* **2017**, *10*, 1861–1877, DOI:10.1002/cssc.201700082.
 14. Flatt, R.; Schober, I. Superplasticizers and the rheology of concrete. In *Understanding the Rheology of Concrete*; Roussel, N. B. T.-U. the R. of C., Ed.; Elsevier, 2012; pp. 144–208 ISBN 978-0-85709-028-7.
 15. Huang, Y.; Miao, Y. E.; Liu, T. Electrospun fibrous membranes for efficient heavy metal removal. *J. Appl. Polym. Sci.* **2014**, *131*, DOI:10.1002/app.40864.
 16. Greiner, A.; Wendorff, J. H. Electrospinning: A Fascinating Method for the

- Preparation of Ultrathin Fibers. *Angew. Chemie Int. Ed.* **2007**, *46*, 5670–5703, DOI:10.1002/anie.200604646.
17. Bhardwaj, N.; Kundu, S. C. Electrospinning: A fascinating fiber fabrication technique. *Biotechnol. Adv.* **2010**, *28*, 325–347, DOI:10.1016/j.biotechadv.2010.01.004.
18. Taylor, G. Electrically Driven Jets. *Proc. R. Soc. A Math. Phys. Eng. Sci.* **1969**, *313*, 453–475, DOI:10.1098/rspa.1969.0205.
19. Yarin, A. L.; Koombhongse, S.; Reneker, D. H. Bending instability in electrospinning of nanofibers. *J. Appl. Phys.* **2001**, *89*, 3018–3026, DOI:10.1063/1.1333035.
20. Deitzel, J. .; Kleinmeyer, J.; Harris, D.; Beck Tan, N. . The effect of processing variables on the morphology of electrospun nanofibers and textiles. *Polymer (Guildf)*. **2001**, *42*, 261–272, DOI:10.1016/S0032-3861(00)00250-0.
21. Liu, H.; Hsieh, Y.-L. Lo Ultrafine fibrous cellulose membranes from electrospinning of cellulose acetate. *J. Polym. Sci. Part B Polym. Phys.* **2002**, *40*, 2119–2129, DOI:10.1002/polb.10261.
22. Ryu, Y. J.; Kim, H. Y.; Lee, K. H.; Park, H. C.; Lee, D. R. Transport properties of electrospun nylon 6 nonwoven mats. *Eur. Polym. J.* **2003**, *39*, 1883–1889, DOI:10.1016/S0014-3057(03)00096-X.
23. McKee, M. G.; Wilkes, G. L.; Colby, R. H.; Long, T. E. Correlations of Solution Rheology with Electrospun Fiber Formation of Linear and Branched Polyesters. *Macromolecules* **2004**, *37*, 1760–1767, DOI:10.1021/ma035689h.
24. Haghi, A. K.; Akbari, M. Trends in electrospinning of natural nanofibers. *Phys. status solidi* **2007**, *204*, 1830–1834, DOI:10.1002/pssa.200675301.
25. Fong, H.; Reneker, D. H. Elastomeric nanofibers of styrene-butadiene-styrene


- triblock copolymer. *J. Polym. Sci. Part B Polym. Phys.* **1999**, *37*, 3488–3493, DOI:10.1002/(SICI)1099-0488(19991215)37:24<3488::AID-POLB9>3.0.CO;2-M.
26. Sukigara, S.; Gandhi, M.; Ayutsede, J.; Micklus, M.; Ko, F. Regeneration of Bombyx mori silk by electrospinning—part 1: processing parameters and geometric properties. *Polymer (Guildf)*. **2003**, *44*, 5721–5727, DOI:10.1016/S0032-3861(03)00532-9.
27. Tan, S.-H.; Inai, R.; Kotaki, M.; Ramakrishna, S. Systematic parameter study for ultra-fine fiber fabrication via electrospinning process. *Polymer (Guildf)*. **2005**, *46*, 6128–6134, DOI:10.1016/j.polymer.2005.05.068.
28. Burger, C.; Hsiao, B. S.; Chu, B. Nanofibrous Materials and Their Applications. *Annu. Rev. Mater. Res.* **2006**, *36*, 333–368, DOI:10.1146/annurev.matsci.36.011205.123537.
29. McKee, M. G.; Layman, J. M.; Cashion, M. P.; Long, T. E. Phospholipid Nonwoven Electrospun Membranes. *Science (80-.)*. **2006**, *311*, 353–355, DOI:10.1126/science.1119790.
30. Baumgarten, P. K. Electrostatic spinning of acrylic microfibers. *J. Colloid Interface Sci.* **1971**, *36*, 71–79, DOI:10.1016/0021-9797(71)90241-4.
31. Doshi, J.; Reneker, D. H. Electrospinning process and applications of electrospun fibers. *J. Electrostat.* **1995**, *35*, 151–160, DOI:10.1016/0304-3886(95)00041-8.
32. Buchko, C. J.; Chen, L. C.; Shen, Y.; Martin, D. C. Processing and microstructural characterization of porous biocompatible protein polymer thin films. *Polymer (Guildf)*. **1999**, *40*, 7397–7407, DOI:10.1016/S0032-3861(98)00866-0.

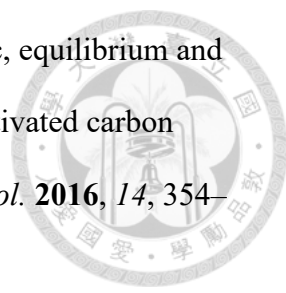
- 
33. Deitzel, J. Electrospinning of polymer nanofibers with specific surface chemistry. *Polymer (Guildf)*. **2002**, *43*, 1025–1029, DOI:10.1016/S0032-3861(01)00594-8.
34. Hohman, M. M.; Shin, M.; Rutledge, G.; Brenner, M. P. Electrospinning and electrically forced jets. II. Applications. *Phys. Fluids* **2001**, *13*, 2221–2236, DOI:10.1063/1.1384013.
35. Zhang, C.; Yuan, X.; Wu, L.; Han, Y.; Sheng, J. Study on morphology of electrospun poly(vinyl alcohol) mats. *Eur. Polym. J.* **2005**, *41*, 423–432, DOI:10.1016/j.eurpolymj.2004.10.027.
36. Pham, Q. P.; Sharma, U.; Mikos, A. G. Electrospun Poly(ϵ -caprolactone) Microfiber and Multilayer Nanofiber/Microfiber Scaffolds: Characterization of Scaffolds and Measurement of Cellular Infiltration. *Biomacromolecules* **2006**, *7*, 2796–2805, DOI:10.1021/bm060680j.
37. Hayati, I.; Bailey, A.; Tadros, T. . Investigations into the mechanism of electrohydrodynamic spraying of liquids. *J. Colloid Interface Sci.* **1987**, *117*, 222–230, DOI:10.1016/0021-9797(87)90186-X.
38. Reneker, D. H.; Yarin, A. L. Electrospinning jets and polymer nanofibers. *Polymer (Guildf)*. **2008**, *49*, 2387–2425, DOI:10.1016/j.polymer.2008.02.002.
39. Zong, X.; Kim, K.; Fang, D.; Ran, S.; Hsiao, B. S.; Chu, B. Structure and process relationship of electrospun bioabsorbable nanofiber membranes. *Polymer (Guildf)*. **2002**, *43*, 4403–4412, DOI:10.1016/S0032-3861(02)00275-6.
40. Reneker, D. H.; Chun, I. Nanometre diameter fibres of polymer, produced by electrospinning. *Nanotechnology* **1996**, *7*, 216–223, DOI:10.1088/0957-4484/7/3/009.

- 
41. Demir, M. ; Yilgor, I.; Yilgor, E.; Erman, B. Electrospinning of polyurethane fibers. *Polymer (Guildf)*. **2002**, *43*, 3303–3309, DOI:10.1016/S0032-3861(02)00136-2.
42. Larrondo, L.; St. John Manley, R. Electrostatic fiber spinning from polymer melts. II. Examination of the flow field in an electrically driven jet. *J. Polym. Sci. Polym. Phys. Ed*. **1981**, *19*, 921–932, DOI:10.1002/pol.1981.180190602.
43. Larrondo, L.; St. John Manley, R. Electrostatic fiber spinning from polymer melts. I. Experimental observations on fiber formation and properties. *J. Polym. Sci. Polym. Phys. Ed*. **1981**, *19*, 909–920, DOI:10.1002/pol.1981.180190601.
44. Larrondo, L.; St. John Manley, R. Electrostatic fiber spinning from polymer melts. III. Electrostatic deformation of a pendant drop of polymer melt. *J. Polym. Sci. Polym. Phys. Ed*. **1981**, *19*, 933–940, DOI:10.1002/pol.1981.180190603.
45. Yördem, O. S.; Papila, M.; Menceloğlu, Y. Z. Effects of electrospinning parameters on polyacrylonitrile nanofiber diameter: An investigation by response surface methodology. *Mater. Des.* **2008**, *29*, 34–44, DOI:10.1016/j.matdes.2006.12.013.
46. Yuan, X.; Zhang, Y.; Dong, C.; Sheng, J. Morphology of ultrafine polysulfone fibers prepared by electrospinning. *Polym. Int.* **2004**, *53*, 1704–1710, DOI:10.1002/pi.1538.
47. Wannatong, L.; Sirivat, A.; Supaphol, P. Effects of solvents on electrospun polymeric fibers: preliminary study on polystyrene. *Polym. Int.* **2004**, *53*, 1851–1859, DOI:10.1002/pi.1599.
48. Kim, K.-H.; Jeong, L.; Park, H.-N.; Shin, S.-Y.; Park, W.-H.; Lee, S.-C.; Kim,

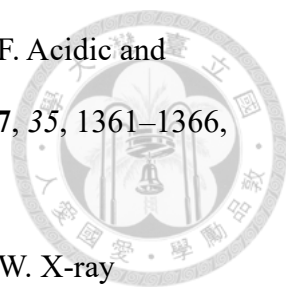
- 
- T.-I.; Park, Y.-J.; Seol, Y.-J.; Lee, Y.-M.; Ku, Y.; Rhyu, I.-C.; Han, S.-B.; Chung, C.-P. Biological efficacy of silk fibroin nanofiber membranes for guided bone regeneration. *J. Biotechnol.* **2005**, *120*, 327–339, DOI:10.1016/j.jbiotec.2005.06.033.
49. Zuo, W.; Zhu, M.; Yang, W.; Yu, H.; Chen, Y.; Zhang, Y. Experimental study on relationship between jet instability and formation of beaded fibers during electrospinning. *Polym. Eng. Sci.* **2005**, *45*, 704–709, DOI:10.1002/pen.20304.
50. Boland, E. D.; Wnek, G. E.; Simpson, D. G.; Pawlowski, K. J.; Bowlin, G. L. Tailoring tissue engineering scaffolds using electrostatic processing techniques: A study of poly(glycolic acid) electrospinning. *J. Macromol. Sci. - Pure Appl. Chem.* **2001**, *38 A*, 1231–1243, DOI:10.1081/MA-100108380.
51. Matthews, J. A.; Wnek, G. E.; Simpson, D. G.; Bowlin, G. L. Electrospinning of Collagen Nanofibers. *Biomacromolecules* **2002**, *3*, 232–238, DOI:10.1021/bm015533u.
52. Bornat, A. Production of Electrostatically Spun Products 1987.
53. Theron, A.; Zussman, E.; Yarin, A. L. Electrostatic field-assisted alignment of electrospun nanofibres. *Nanotechnology* **2001**, *12*, 384–390, DOI:10.1088/0957-4484/12/3/329.
54. Huang, Z.-M.; Zhang, Y.-Z.; Kotaki, M.; Ramakrishna, S. A review on polymer nanofibers by electrospinning and their applications in nanocomposites. *Compos. Sci. Technol.* **2003**, *63*, 2223–2253, DOI:10.1016/S0266-3538(03)00178-7.
55. Lee, J. S.; Choi, K. H.; Ghim, H. Do; Kim, S. S.; Chun, D. H.; Kim, H. Y.; Lyoo, W. S. Role of molecular weight of atactic poly(vinyl alcohol) (PVA) in the structure and properties of PVA nanofabric prepared by electrospinning. *J.*

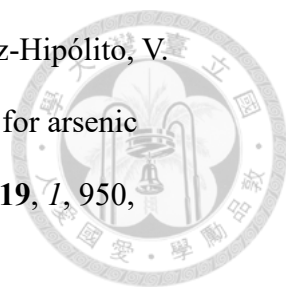
- Appl. Polym. Sci.* **2004**, *93*, 1638–1646, DOI:10.1002/app.20602.
56. Geng, X.; Kwon, O. H.; Jang, J. Electrospinning of chitosan dissolved in concentrated acetic acid solution. *Biomaterials* **2005**, *26*, 5427–5432, DOI:10.1016/j.biomaterials.2005.01.066.
57. Ki, C. S.; Baek, D. H.; Gang, K. D.; Lee, K. H.; Um, I. C.; Park, Y. H. Characterization of gelatin nanofiber prepared from gelatin–formic acid solution. *Polymer (Guildf)*. **2005**, *46*, 5094–5102, DOI:10.1016/j.polymer.2005.04.040.
58. Casper, C. L.; Stephens, J. S.; Tassi, N. G.; Chase, D. B.; Rabolt, J. F. Controlling Surface Morphology of Electrospun Polystyrene Fibers: Effect of Humidity and Molecular Weight in the Electrospinning Process. *Macromolecules* **2004**, *37*, 573–578, DOI:10.1021/ma0351975.
59. Li, D.; Xia, Y. Electrospinning of Nanofibers: Reinventing the Wheel? *Adv. Mater.* **2004**, *16*, 1151–1170, DOI:10.1002/adma.200400719.
60. Li, M.; Mondrinos, M. J.; Gandhi, M. R.; Ko, F. K.; Weiss, A. S.; Lelkes, P. I. Electrospun protein fibers as matrices for tissue engineering. *Biomaterials* **2005**, *26*, 5999–6008, DOI:10.1016/j.biomaterials.2005.03.030.
61. Mit-uppatham, C.; Nithitanakul, M.; Supaphol, P. Ultrafine Electrospun Polyamide-6 Fibers: Effect of Solution Conditions on Morphology and Average Fiber Diameter. *Macromol. Chem. Phys.* **2004**, *205*, 2327–2338, DOI:10.1002/macp.200400225.
62. Worasuwannarak, N.; Hatori, S.; Nakagawa, H.; Miura, K. Effect of oxidation pre-treatment at 220 to 270 °C on the carbonization and activation behavior of phenolic resin fiber. *Carbon N. Y.* **2003**, *41*, 933–944, DOI:10.1016/S0008-6223(02)00426-8.

- 
63. Norberg, I. Carbon Fibres from Kraft Lignin TT - Kolfiber från sulfatlignin (swe), KTH Royal Institute of Technology: Wood Chemistry and Pulp Technology, Fibre and Polymer Technology, School of Chemical Science and Engineering (CHE), KTH, 2012.
64. Yue, Z.; Economy, J. Carbonization and activation for production of activated carbon fibers. In *Activated Carbon Fiber and Textiles*; Chen, J. Y., Ed.; Elsevier: Oxford, 2017; pp. 61–139 ISBN 9780081006788.
65. Park, S.-J. Precursors and Manufacturing of Carbon Fibers. In *Springer Series in Materials Science*; Park, S.-J., Ed.; Springer Singapore: Singapore, 2018; Vol. 210, pp. 31–67 ISBN 978-981-13-0538-2.
66. Thommes, M. Physical Adsorption Characterization of Nanoporous Materials. *Chemie Ing. Tech.* **2010**, *82*, 1059–1073, DOI:10.1002/cite.201000064.
67. Thommes, M.; Cychosz, K. A.; Neimark, A. V. Advanced Physical Adsorption Characterization of Nanoporous Carbons. In *Novel Carbon Adsorbents*; Tascón, J. M. D., Ed.; Elsevier: Oxford, 2012; pp. 107–145 ISBN 9780080977447.
68. Thommes, M.; Kaneko, K.; Neimark, A. V.; Olivier, J. P.; Rodriguez-Reinoso, F.; Rouquerol, J.; Sing, K. S. W. Physisorption of gases, with special reference to the evaluation of surface area and pore size distribution (IUPAC Technical Report). *Pure Appl. Chem.* **2015**, *87*, 1051–1069, DOI:10.1515/pac-2014-1117.
69. Sing, K. S. W. Reporting physisorption data for gas/solid systems with special reference to the determination of surface area and porosity (Recommendations 1984). *Pure Appl. Chem.* **1985**, *57*, 603–619, DOI:10.1351/pac198557040603.
70. Bansal, R. C.; Goyal, M. *Activated carbon adsorption*; 1st Editio.; ICE Publishing: Boca Raton, 2005; ISBN 9781420028812.

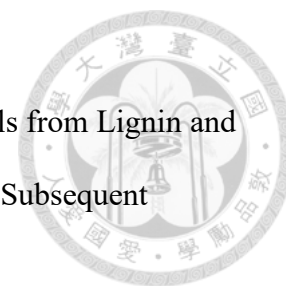
- 
71. Belhamdi, B.; Merzougui, Z.; Trari, M.; Addoun, A. A kinetic, equilibrium and thermodynamic study of l-phenylalanine adsorption using activated carbon based on agricultural waste (date stones). *J. Appl. Res. Technol.* **2016**, *14*, 354–366, DOI:10.1016/j.jart.2016.08.004.
72. Das, N. Recovery of precious metals through biosorption - A review. *Hydrometallurgy* **2010**, *103*, 180–189, DOI:10.1016/j.hydromet.2010.03.016.
73. Marsh, H.; Rodríguez-Reinoso, F. *Activated Carbon*; Elsevier, 2006; ISBN 9780080444635.
74. Li, L.; Quinlivan, P. A.; Knappe, D. R. U. Effects of activated carbon surface chemistry and pore structure on the adsorption of organic contaminants from aqueous solution. *Carbon N. Y.* **2002**, *40*, 2085–2100, DOI:10.1016/S0008-6223(02)00069-6.
75. Di Natale, F.; Orefice, M.; La Motta, F.; Erto, A.; Lancia, A. Unveiling the potentialities of activated carbon in recovering palladium from model leaching solutions. *Sep. Purif. Technol.* **2017**, *174*, 183–193, DOI:10.1016/j.seppur.2016.10.022.
76. Alfarra, A.; Frackowiak, E.; Béguin, F. The HSAB concept as a means to interpret the adsorption of metal ions onto activated carbons. *Appl. Surf. Sci.* **2004**, *228*, 84–92, DOI:10.1016/j.apsusc.2003.12.033.
77. Frost, H.; Düren, T.; Snurr, R. Q. Effects of surface area, free volume, and heat of adsorption on hydrogen uptake in metal-organic frameworks. *J. Phys. Chem. B* **2006**, *110*, 9565–9570, DOI:10.1021/jp060433.
78. Reid, C. R.; Thomas, K. M. Adsorption Kinetics and Size Exclusion Properties of Probe Molecules for the Selective Porosity in a Carbon Molecular Sieve Used for Air Separation. *J. Phys. Chem. B* **2001**, *105*, 10619–10629,

- DOI:10.1021/jp0108263.
79. Kadirvelu, K.; Faur-Brasquet, C.; Cloirec, P. Le Removal of Cu(II), Pb(II), and Ni(II) by Adsorption onto Activated Carbon Cloths. *Langmuir* **2000**, *16*, 8404–8409, DOI:10.1021/la0004810.
80. Hu, S.; Hsieh, Y.-L. Ultrafine microporous and mesoporous activated carbon fibers from alkali lignin. *J. Mater. Chem. A* **2013**, *1*, 11279, DOI:10.1039/c3ta12538f.
81. Lowell, S.; Shields, J. E.; Thomas, M. A.; Thommes, M. Surface Area Analysis from the Langmuir and BET Theories. In *Characterization of Porous Solids and Powders: Surface Area, Pore Size and Density*; Lowell, S., Shields, J. E., Thomas, M. A., Thommes, M., Eds.; Springer Netherlands: Dordrecht, 2004; pp. 58–81 ISBN 978-1-4020-2303-3.
82. Rouquerol, J.; Llewellyn, P.; Rouquerol, F. Is the bet equation applicable to microporous adsorbents? In *Studies in Surface Science and Catalysis*; 2007; Vol. 160, pp. 49–56.
83. ISO [International Organization for Standardization] Determination of the specific surface area of solids by gas adsorption - BET method (ISO 9277:2010(E)). *Ref. number ISO* **2010**, 9277, 30 pp., DOI:10.1007/s11367-011-0297-3.
84. Neimark, A. V.; Lin, Y.; Ravikovitch, P. I.; Thommes, M. Quenched solid density functional theory and pore size analysis of micro-mesoporous carbons. *Carbon N. Y.* **2009**, *47*, 1617–1628, DOI:10.1016/j.carbon.2009.01.050.
85. Leon y Leon, C. A.; Solar, J. M.; Calemma, V.; Radovic, L. R. Evidence for the protonation of basal plane sites on carbon. *Carbon N. Y.* **1992**, *30*, 797–811, DOI:10.1016/0008-6223(92)90164-R.

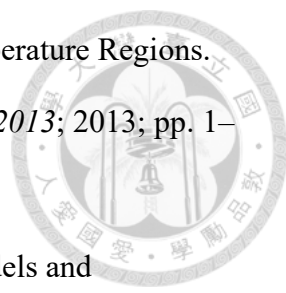
- 
86. Barton, S. S.; Evans, M. J. B.; Halliop, E.; MacDonald, J. A. F. Acidic and basic sites on the surface of porous carbon. *Carbon N. Y.* **1997**, *35*, 1361–1366, DOI:10.1016/S0008-6223(97)00080-8.
87. Tze, W. T. Y.; Bernhardt, G.; Gardner, D. J.; Christiansen, A. W. X-ray photoelectron spectroscopy of wood treated with hydroxymethylated resorcinol. *Int. J. Adhes. Adhes.* **2006**, *26*, 550–554, DOI:10.1016/j.ijadhadh.2005.08.002.
88. Schönherr, J.; Buchheim, J.; Scholz, P.; Adelhelm, P. Boehm Titration Revisited (Part II): A Comparison of Boehm Titration with Other Analytical Techniques on the Quantification of Oxygen-Containing Surface Groups for a Variety of Carbon Materials. *C* **2018**, *4*, 22, DOI:10.3390/c4020022.
89. Cheng, S.; Zhang, L.; Xia, H.; Peng, J.; Shu, J.; Li, C. Ultrasound and microwave-assisted preparation of Fe-activated carbon as an effective low-cost adsorbent for dyes wastewater treatment. *RSC Adv.* **2016**, *6*, 78936–78946, DOI:10.1039/c6ra14082c.
90. Shimodaira, N.; Masui, A. Raman spectroscopic investigations of activated carbon materials. *J. Appl. Phys.* **2002**, *92*, 902–909, DOI:10.1063/1.1487434.
91. ASTM International Standard Practice for Determination of Adsorptive Capacity of Activated Carbon by Aqueous Phase Isotherm Technique. *ASTM Stand.* **2004**, *15*, 1–4, DOI:10.1520/D3860-98R08.2.
92. Peng, M.; Nguyen, A. V.; Wang, J.; Miller, R. A critical review of the model fitting quality and parameter stability of equilibrium adsorption models. *Adv. Colloid Interface Sci.* **2018**, *262*, 50–68, DOI:10.1016/j.cis.2018.10.001.
93. López-Luna, J.; Ramírez-Montes, L. E.; Martínez-Vargas, S.; Martínez, A. I.; Mijangos-Ricardez, O. F.; González-Chávez, M. del C. A.; Carrillo-González,

- 
- R.; Solís-Domínguez, F. A.; Cuevas-Díaz, M. del C.; Vázquez-Hipólito, V. Linear and nonlinear kinetic and isotherm adsorption models for arsenic removal by manganese ferrite nanoparticles. *SN Appl. Sci.* **2019**, *1*, 950, DOI:10.1007/s42452-019-0977-3.
94. Kinniburgh, D. G. General Purpose Adsorption Isotherms. *Environ. Sci. Technol.* **1986**, *20*, 895–904, DOI:10.1021/es00151a008.
95. Redlich, O.; Peterson, D. L. A useful adsorption isotherm. *J. Phys. Chem.* **1959**, *63*, 1024, DOI:10.1021/j150576a611.
96. Ramos, S. N. do C.; Xavier, A. L. P.; Teodoro, F. S.; Elias, M. M. C.; Gonçalves, F. J.; Gil, L. F.; de Freitas, R. P.; Gurgel, L. V. A. Modeling mono- and multi-component adsorption of cobalt(II), copper(II), and nickel(II) metal ions from aqueous solution onto a new carboxylated sugarcane bagasse. Part I: Batch adsorption study. *Ind. Crops Prod.* **2015**, *74*, 357–371, DOI:10.1016/j.indcrop.2015.05.022.
97. Lagergren, S. Zur Theorie der sogenannten Adsorption gelöster Stoffe. *Zeitschrift für Chemie und Ind. der Kolloide* **1907**, *2*, 15–15, DOI:10.1007/BF01501332.
98. Largitte, L.; Pasquier, R. A review of the kinetics adsorption models and their application to the adsorption of lead by an activated carbon. *Chem. Eng. Res. Des.* **2016**, *109*, 495–504, DOI:10.1016/j.cherd.2016.02.006.
99. Tan, K. L.; Hameed, B. H. Insight into the adsorption kinetics models for the removal of contaminants from aqueous solutions. *J. Taiwan Inst. Chem. Eng.* **2017**, *74*, 25–48, DOI:10.1016/j.jtice.2017.01.024.
100. Ho, Y. S.; McKay, G. Pseudo-second order model for sorption processes. *Process Biochem.* **1999**, *34*, 451–465, DOI:https://doi.org/10.1016/S0032-

- 9592(98)00112-5.
101. Leitner, S.; Gratzl, G.; Paulik, C.; Weber, H. Carbon Materials from Lignin and Sodium Lignosulfonate via Diisocyanate Cross-Linking and Subsequent Carbonization. *C* **2015**, *1*, 43–57, DOI:10.3390/c1010043.
102. Shin, S.; Jang, J.; Yoon, S.-H.; Mochida, I. A study on the effect of heat treatment on functional groups of pitch based activated carbon fiber using FTIR. *Carbon N. Y.* **1997**, *35*, 1739–1743, DOI:10.1016/S0008-6223(97)00132-2.
103. Qi, F.; Yan, Y.; Lamb, D.; Naidu, R.; Bolan, N. S.; Liu, Y.; Ok, Y. S.; Donne, S. W.; Semple, K. T. Thermal stability of biochar and its effects on cadmium sorption capacity. *Bioresour. Technol.* **2017**, DOI:10.1016/j.biortech.2017.07.033.
104. Chingombe, P.; Saha, B.; Wakeman, R. J. Surface modification and characterisation of a coal-based activated carbon. *Carbon N. Y.* **2005**, *43*, 3132–3143, DOI:10.1016/j.carbon.2005.06.021.
105. Li, J.; Su, S.; Zhou, L.; Kunderát, V.; Abbot, A. M.; Mushtaq, F.; Ouyang, D.; James, D.; Roberts, D.; Ye, H. Carbon nanowalls grown by microwave plasma enhanced chemical vapor deposition during the carbonization of polyacrylonitrile fibers. *J. Appl. Phys.* **2013**, *113*, 024313, DOI:10.1063/1.4774218.
106. Ying, W.; Shi, Z.; Yang, H.; Xu, G.; Zheng, Z.; Yang, J. Effect of alkaline lignin modification on cellulase–lignin interactions and enzymatic saccharification yield. *Biotechnol. Biofuels* **2018**, *11*, 214, DOI:10.1186/s13068-018-1217-6.
107. Liu, C.; Xu, J.; Hu, J.; Zhang, H.; Xiao, R. Metal Ion-Catalyzed Hydrothermal Liquefaction of Calcium Lignosulfonate in Subcritical Water. *Chem. Eng.*



- Technol.* **2017**, *40*, 1092–1100, DOI:10.1002/ceat.201600650.
108. Chen, J.; Liu, C.; Wu, S.; Liang, J.; Lei, M. Enhancing the quality of bio-oil from catalytic pyrolysis of kraft black liquor lignin. *RSC Adv.* **2016**, *6*, 107970–107976, DOI:10.1039/c6ra18923g.
109. Rashid, T.; Kait, C. F.; Murugesan, T. A “Fourier Transformed Infrared” Compound Study of Lignin Recovered from a Formic Acid Process. *Procedia Eng.* **2016**, *148*, 1312–1319, DOI:10.1016/j.proeng.2016.06.547.
110. Lin-Vien, D.; Colthup, N. B.; Fateley, W. G.; Grasselli, J. G. Compounds Containing the Carbonyl Group. In *The Handbook of Infrared and Raman Characteristic Frequencies of Organic Molecules*; Lin-Vien, D., Colthup, N. B., Fateley, W. G., Grasselli, J. G. B. T.-T. H. of I. and R. C. F. of O. M., Eds.; Elsevier: San Diego, 1991; pp. 117–154 ISBN 978-0-12-451160-6.
111. Hoseinzadeh Hesas, R.; Arami-Niya, A.; Wan Daud, W. M. A.; Sahu, J. N. Preparation and Characterization of Activated Carbon from Apple Waste by Microwave-Assisted Phosphoric Acid Activation: Application in Methylene Blue Adsorption. *BioResources* **2013**, *8*, DOI:10.15376/biores.8.2.2950-2966.
112. Zhang, Y.; Wu, J.-Q.; Li, H.; Yuan, T.-Q.; Wang, Y.-Y.; Sun, R.-C. Heat Treatment of Industrial Alkaline Lignin and its Potential Application as an Adhesive for Green Wood–Lignin Composites. *ACS Sustain. Chem. Eng.* **2017**, *5*, 7269–7277, DOI:10.1021/acssuschemeng.7b01485.
113. Liu, W.-J.; Jiang, H.; Yu, H.-Q. Thermochemical conversion of lignin to functional materials: a review and future directions. *Green Chem.* **2015**, *17*, 4888–4907, DOI:10.1039/C5GC01054C.
114. Kawamoto, H. Lignin pyrolysis reactions. *J. Wood Sci.* **2017**, *63*, 117–132, DOI:10.1007/s10086-016-1606-z.

- 
115. Ház, A.; Jablonský, M.; Orságová, A. Determination of Temperature Regions. In *4th International Conference Renewable Energy Sources 2013*; 2013; pp. 1–6.
116. Archontoulis, S. V.; Miguez, F. E. Nonlinear Regression Models and Applications in Agricultural Research. *Agron. J.* **2015**, *107*, 786, DOI:10.2134/agronj2012.0506.
117. Liu, Y. Is the Free Energy Change of Adsorption Correctly Calculated? *J. Chem. Eng. Data* **2009**, *54*, 1981–1985, DOI:10.1021/je800661q.